NON-EQUILIBRIUM ELECTRON DYNAMICS IN SEMICONDUCTING TRANSITION METAL DICHALCOGENIDES

Tetiana Borzda

Doctoral Dissertation
Jožef Stefan International Postgraduate School
Ljubljana, Slovenia

Supervisor: Prof. Dr. Christoph Gadermaier, Jožef Stefan Institute, Jamova 39, Ljubljana, Slovenia
Co-Supervisor: Prof. Dr. Viktor Kabanov, Jožef Stefan Institute, Jamova 39, Ljubljana, Slovenia

Evaluation Board:
Prof. Dr. Maja Remškar, Chair, Jožef Stefan Institute, Jamova 39, Ljubljana, Slovenia
Asst. Prof. Dr. Tomaž Mertelj, Member, Jožef Stefan Institute, Jamova 39, Ljubljana, Slovenia
Dr. Nataša Vujičić, Member, Institute of Physics, Bijenička 46, Zagreb, Croatia

MEDNARODNA PODIPLOMSKA ŠOLA JOŽEFA STEFANA
JOŽEF STEFAN INTERNATIONAL POSTGRADUATE SCHOOL



Tetiana Borzda

NON-EQUILIBRIUM ELECTRON DYNAMICS IN SEMICONDUCTING TRANSITION METAL DICHALCOGENIDES

Doctoral Dissertation

NERAVNOVESNA DINAMIKA ELEKTRONOV V POLPREVODNIŠKIH DIHALKOGENIDIH PREHODNIH KOVIN

Doktorska disertacija

Supervisor: Prof. Dr. Christoph Gadermaier

Co-Supervisor: Prof. Dr. Viktor Kabanov

Ljubljana, Slovenia, May 2017

To my Family
There is no greater gift than education

Acknowledgments

First of all, I would like to acknowledge my supervisor Prof. Dr. Christoph Gadermaier for giving me the opportunity to work in the field of two-dimensional materials. I am grateful for his support, continual availability to answer questions and helpful feedback.

Special thanks go to Dr. Nataša Vujičić for introducing me to pump-probe spectroscopy. Nataša, thank you for our serious discussion and jokes that kept my motivation level constantly high.

I would also like to thank my colleagues – Daniele and Victor and all my co-workers from the Department of Complex Matter for making my job much easier.

Special thanks go to the members of committee: Prof. Dr. Maja Remškar, Asst. Prof. Dr. Tomaž Mertelj, Dr. Nataša Vujičić for carefully reading my thesis and for giving detailed comments and suggestions that have been helpful to improve the thesis.

I must also thank my family: mother Lybov, brother Oleksandr, father Volodymur, grandparents for their continued support.

Abstract

This thesis is dedicated to the study equilibrium and non-equilibrium optical properties of two-dimensional materials, in particular transition metal dichalcogenides (TMDs) such as MoS_2. Their potential for electronics has become evident by the realization of a field effect transistor based on a single flake of monolayer MoS_2.

After an introduction to TMD materials and their photophysics as well as the experimental methods used in this thesis, the first experimental chapter addresses the apparent conflict between strongly bound excitons on the one hand and efficient photovoltaics and sensitive photodetectors on the other. I use continuous wave photomodulation and femtosecond pump-probe spectroscopy to identify the spectral features of photogenerated charges and trace their dynamics, starting with their generation either by direct impulsive excitation into the charge continuum or via exciton dissociation. An ensemble of MoS_2 few-layer flakes obtained from liquid exfoliation dispersed in electronically inert PMMA matrix were used. The spectra and the relaxation times of the signal are very similar to those obtained on individual few-layer flakes. Hence the present study directly extends existing knowledge on the femtosecond behavior of few-layer MoS_2.

Soon after the publication of the first experimental chapter as a journal article, an alternative interpretation concerning the origin of the femtosecond transient absorption changes was proposed. Rather than a change in the transition probability due to a photoinduced change in the level occupation, the new work ascribed them to shifts and changes in lineshape due to the combined action of bandgap renormalization and screening of the electron-hole Coulomb interaction that provides the exciton binding energy. The data from the first experimental chapter was reassessed by synthesizing the transient absorption spectra from the measured changes and tracing the evolution of the individual — strongly overlapping — absorption peaks assigned to the various transitions. Rather than confirming one and refuting the other of two apparently opposing interpretations of the transient spectra, I find that both contributions are relevant, with the lineshape changes and shifts more important during the first picosecond, and the population effects dominating the signal at subsequent delays. By disentangling these two contributions, my analysis shows how to extract more and more relevant information from future and existing femtosecond optical data on two-dimensional semiconductors.

In the last part of the thesis I present the attempt to develop metrics for characterization of the doping level of two-dimensional materials. The investigation of the three main Raman peaks of WSe_2 in a field effect transistor with ionic liquid gating, which allows to control the doping level over a wide range was done. I track the positions and intensities of these peaks as a function of doping level and find several combinations — peak distances or intensity ratios that can be used as metrics for fast characterization.

Povzetek

Nedaven napredek na področjih eksfoliacije plastovitih materialov in izdelava nanonaprav sta obudila zanimanje za dvodimenzionalne snovi z lastnostmi komplementarnimi grafenu, zlasti za dihalkogenide prehodnih kovin (ang. transition metal dichalcogenides – TMD), kot je MoS_2. Njihov potencial za uporabo v elektroniki je postal očiten po izdelavi poljskega tranzistorja in logičnih vrat na osnovi posamezne luske monoplastnega MoS_2.

Po uvodu v materiale TMD in njihovo fotofiziko ter opisu eksperimentalnih metod uporabljenih v disertaciji, sem v prvem eksperimentalnem poglavju opisala navidezno nasprotje med močno vezanimi ekscitoni na eni ter učinkovito fotovoltaiko in občutljivimi fotodetektorji na drugi strani. V doktorskem delu sem uporabila fotomodulacijo zveznega svetlobnega vira (ang. continous wave-CW) in femtosekundno črpalno-testno spektroskopijo za prepoznanje spektralnih značilnosti fotogeneriranih nabojev in sledenje njihovi dinamiki, začenši z generacijo bodisi s sunkovnim vzbujanjem v nabojni kontinuum bodisi prek ekscitonske disociacije. Kot makroskopski vzorec, ki ga enostavno preučimo v različnih eksperimentalnih postavitvah brez večjih sprememb, sem uporabila nekajplastne luske MoS_2, ki sem jih dobila s tekočinsko eksfoliacijo in jih vmešala v PMMA, ki je predstavljala prozorno elektronsko inertno matriko. Spektri in relaksacijski časi signala bili zelo podobni tistim iz individualnih nekajplastnih lusk. Predstavljena študija direktno razširja obstoječe znanje o femtosekundnem obnašanju nekajplastnega MoS_2.

Kmalu po objavi pervega eksperimentalnega poglavja v obliki članka je bila predlagana alternativna interpretacija glede izvora femtosekundnih prehodnih absorpcijskih sprememb. Raje kot pripisati spremembo verjetnostni prehoda fotoinducirani spremembi nivoja zasedenosti, ga novo delo pripiše zamikom in spremembi oblike spektra zaradi kombiniranega prispevka renormalizacije pasovne reže in senčenje elektronsko-vrzelne Coulombske interakcije, ki določa vezavno energijo ekssitonov. Ponovno sem pregledala in ovrednotila podatke iz pervega eksperimentalnega poglavja s sintetiziranjem prehodnih absorpcijskih spektrov iz izmerjenih razlik in sledenjem evoluciji posameznih – močno prekrivajočih — absorpcijskih vrhov, ki so pripisani različnim prehodom. Raje kot potrditi eno ali ovreči drugo od dveh navidez nasprotujočih interpretacij tranzientnih spektrov, menim, da sta obe interpretaciji relevantni, spremembe in zamiki spektralnih črt so bolj pomembni v prvi pikosekundni, populacijski efekti pa dominirajo signal pri večjih zamikih. Z razpletom teh dveh prispevkov moja analiza kaže, kako izvleči čimveč pomembnih informacij iz obstoječih in prihodnjih femtosekundnih optičnih podatkov o dvodimenzionalnih polprevodnikih.

V zadnjem delu sem raziskovala tri glavne Ramanove vrhove WSe_2 v poljskem tranzistorju z ionskotekočinskimi vrati, kar omogoča nastavitev nivoja dopiranja v širokem razponu. Sledila sem pozicijam in intenzitetam teh vrhov kot funkciji nivoja dopiranja in našla več kombinacij — razdalje med vrhoma ali razmerja intenzitet — ki dopolnjujejo obstoječo metriko za natančnejšo in razumljivejšo karakterizacijo dvo-dimenzionalnih materialov.

Contents

List of Figures **xv**

Abbreviations **xix**

1 Introduction **1**
1.1 Excitons in Semiconductors . . . 1
1.1.1 Excitons in Bulk Semiconductors . . . 1
1.1.2 Excitons in Quasi-2D Semiconductors . . . 3
1.2 Structure and Physical properties of TMDs . . . 3
1.2.1 Structural properties . . . 3
1.2.2 Raman and Photoluminescence Spectroscopy . . . 7
1.2.3 Light Absorption, Excitons and Trions . . . 8
1.2.4 Ultrafast Carrier, Exciton and Many-body dynamics . . . 11

2 Experimental Techniques and Samples Preparation **15**
2.1 Generation of ultrashort laser pulses . . . 15
2.2 Optical nonlinear processes . . . 16
2.2.1 Supercontinuum generation . . . 17
2.3 Pump-probe spectroscopy . . . 18
2.3.1 Possible type of signals in Pump-probe measurements . . . 19
2.3.2 Pump-probe setup . . . 19
2.4 Photo-induced absorption spectroscopy . . . 21
2.5 Samples' preparation . . . 22
2.5.1 Characterization of the samples by Steady-State Absorption and Raman scattering . . . 23

3 Charge photogeneration in few-layer MoS_2 **25**
3.1 Continuous wave photomodulation spectroscopy data on MoS_2 . . . 25
3.2 Ultrafast data on MoS_2 . . . 26
3.3 Model of exciton dissociation to charge carriers in MoS_2 . . . 27
3.3.1 Branching ratio in direct generation of excitons and charges . . . 30
3.4 Discussion . . . 32
3.4.1 Conclusion . . . 34

4 Quasiparticles vs many-body interactions in photoexcited MoS_2 **35**
4.1 Results and Discussion . . . 36
4.2 Conclusion . . . 40

5 Doping signatures in the Raman spectrum of monolayer WSe_2 **41**
5.1 Results and Discussion . . . 43
5.2 Conclusions . . . 45

6 Conclusions **49**

References **51**

Bibliography **63**

Biography **65**

List of Figures

Figure 1.1: a. Schematic of optical excitation of a semiconductor and creation of excitonic bands. b. Semiconductor typical absorption spectrum. 2
Figure 1.2: Schematic drawing of an indirect-gap semiconductor band structure. . . 2
Figure 1.3: Schematic of 1T-, 2*H*-, 3*R*-MoS_2 polymorphs. 4
Figure 1.4: a. Band structure in the terms of metal atomic orbitals [5]. b. Relative contribution of individual atomic orbitals to the band structure of MoS_2. Image taken from [6]. c. Brilloin zone of MoS_2. 5
Figure 1.5: DFT calculation of the evolution of the MoS_2 band structure upon decreasing thickness. During decreasing thickness a transition from an indirect band-gap semiconductor to a direct one occurs. The horizontal dashed lines indicate the Fermi level. Image taken from [7] 6
Figure 1.6: Spin-orbit splitting in the conduction and valence band near the K and -K points. Spin-polarized bands are indicated by up (spin-up) and down (spin-down) arrows. The dashed circles are used for describing left and right photon polarization. 7
Figure 1.7: Possible Raman and IR modes in MoS_2. Image adopted from [14] . . . 8
Figure 1.8: a. Photoluminescence spectrum taken from 1- and 2-layer MoS_2 samples. Image taken from [4]. b. Raman spectra of in-plane(E^1_{2g}) and out of plane(A_{1g}) modes taken from MoS_2 samples with different number of layers. Shift of both modes with thickness and frequency difference $\omega(A_{1g}) - \omega(E^1_{2g})$ depending on layer number. Image taken from [15] . . 9
Figure 1.9: a. Excitons in both valleys using the exciton basis. Empty circle is a hole, black circle is an electron; up and down arrows indicate particles with spin-up and spin-down; red dashed circle reperesents bright excitons, blue dashed circle reperesents dark excitons. b. The ultrafast intravalley and intervalley relaxation of carriers. Image adopted from [19]. 10
Figure 1.10: a. Artistic drawing of exciton (X), trions (X^- – similar to hydrogen ion H^-, X^+ – similar to ionized hydrogen molecule $H_2{}^+$) and biexcitons (XX). b. Schematic of electron and hole configuration in neutral and charged excitons (trions) versus the doping of the crystal. c. Photoluminescence from monolayer MoS_2 upon doping a new trion (A^-) peak appears. Image taken from [28]. 11

Figure 2.1: The pulses train which were obtained due to many modes generation: pulse phases are locked (blue); pulse phases are random (red). Image taken from Ref. [40] 15
Figure 2.2: Possible modes in the laser resonator (blue) and pulses train when modes are locked. Image taken from Ref. [41] 16

Figure 2.3: Examples of the white-light spectrum in the sapphire and YAG crystals. In the range which is marked with arrows the number of photons is significantly higher than the one generated from the sapphire continuum. Image taken from Ref. [44]. 18
Figure 2.4: The sketch of pump-probe setup used in the thesis 20
Figure 2.5: A sketch of the photoinduced steady-state absorption setup used in the experiment. 20
Figure 2.6: The pulse train from CW laser modulated by chopper (upper row), the signal from the system under investigation when the population relaxation time is shorter than modulation period (middle row) and when the population relaxation time is longer than modulation period (lower row). 21
Figure 2.7: The components of ionic liquid: a. 1-ethyl-3-methylimidazolium (EMIM) cation; b. bis(trifluoromethylsulfonyl)imide (TFSI) anion. 22
Figure 2.8: Raman spectra of MoS_2 at two excitation wavelengths at 633 nm (red line) and 488 nm (blue line) 23
Figure 2.9: Absorption spectrum of the sample of MoS_2 in PMMA. Inset shows a photograph (the dark area has a diameter of approximately 7-8 mm) . . 24

Figure 3.1: (a) CW photoinduced absorption spectrum of MoS_2 in PMMA at room temperature for excitation at 3.1 eV. In-phase (blue) and quadrature (green) signal components are shown for a modulation frequency of 245 Hz. (b) Five Gaussian fits (red) whose sum (blue) fits the normalized in-phase spectrum (open squares). 26
Figure 3.2: (a) Normalized CW photomodulation spectrum of MoS_2 in PMMA (blue) compared to the fs transient spectrum at 300 ps pump-probe (black) delay for $2*10^{14}$ cm^{-2} excitation fluence, 3.1 eV pump photon energy. (b) Pump-probe spectra at 300 ps normalized to the B exciton peak for different pump fluences at 3.1 eV pump photon energy: $2*10^{14}$ (black), $3*10^{14}$(red), $6*10^{14}$ (green), $20*10^{14}$ (blue), $40*10^{14}$ (cyan) and $80*10^{14}$ cm^{-2} (magenta). 27
Figure 3.3: (a) Pump-probe spectra for $4*10^{15}$ cm^{-2} pump fluence at delays 300 fs (black), 1 ps (orange), 3 ps (red), 10 ps (purple), 30 ps (green), 100 ps (dark cyan), and 300 ps (blue). (b) Selected spectra from (a) normalized to the B^0 peak. (c) Normalized time traces for different probe energies: 2.48 (black), 2.25 (red), 2.07 (green), 1.94 (blue) and 1.80 eV (dark cyan). (d) Normalized spectra at 300 ps pump-probe delay for different pump photon energies: 3.10 (purple), 2.48 (blue), 2.34 (dark cyan) and 2.25 eV (green). 28
Figure 3.4: (a) Scheme of the photoexcitation dynamics of excitons and charges. (b) Time dependent exciton (blue) and charge (green) populations (c) Spectral contributions of excitons (blue) and charges (green). 29
Figure 3.5: (a) Contour plot of the measured $\Delta T/T$ (in %). (b) Contour plot of the fitted $\Delta T/T$ (in %). 29
Figure 3.6: (a-i) calculated exciton (black, purple, blue) and charge (red, orange, green) spectra for different branching ratios and dissociation yields (see insert). (j-l) calculated exciton and charge populations for the branching ratios of the same column and different dissociation yields (same color code). 31

Figure 4.1: (a) Extinction spectrum of few-layer MoS_2 in PMMA. (b) exciton and trion contributions to the extinction spectrum, showing the background corrected extinction (black), and the fit as the sum (blue) of five Gaussians (green, labeled). 37
Figure 4.2: (a) Transient differential transmission spectrum of MoS_2 in PMMA for selected pump-probe delays. (b) contour plot of $\Delta T/T$ in %. 37
Figure 4.3: (a) Transient absorption spectra (spectra in Fig. 4.2a subtracted from the spectrum in Fig. 4.1b). (b) Exciton and trion contributions to the transient absorption spectra. 38
Figure 4.4: (a) Transient absorption spectra (spectra in Fig. 4.2a subtracted from the spectrum in Fig. 4.1b). (b) Exciton and trion contributions to the transient absorption spectra. 39

Figure 5.1: (a) Scheme of the WSe_2 FET. (b) transistor characteristics with an estimate of the gate-dependent charge density in the channel. (c) Raman spectrum for parallel and cross polarization at 0 gate voltage. (d) dielectric function of WSe_2 [111]. (e) Raman spectrum of MoS_2 FET for parallel and cross polarization at 0 gate voltage. 42
Figure 5.2: Raman signals for parallel (a,b) and cross polarization (c-f) in the n (a,c,e) and p (b,d,f) regions. Due to the poor signal-to-noise levels, Figure (f) shows the fits to three Lorentzians in addition to the original data. 44
Figure 5.3: (a) Normalized (to the areas of E$^{'}$ and $A_1^{'}$ peaks at 0 V top gate voltages) area for E$^{'}$ and $A_1^{'}$ peaks at different gate voltages. (b) Area ratio for E$^{'}$ and $A_1^{'}$ peaks. (c-d) Full width at half maximum (FWHM) for peak E$^{'}$ and peak E$^{'}$+$A_1^{'}$. (e) Positions of E$^{'}$ and $A_1^{'}$ peaks at different voltages. (f) Relative positions of 2LA (M), E$^{'}$ and $A_1^{'}$ peaks as function of voltages. 46
Figure 5.4: (a-b) Metrics: full width at half maximum (FWHM) for peak E$^{'}$ and peak E$^{'}$+$A_1^{'}$ as a function of charge density (n, bottom axis) and applied gate voltages (V_{TG}) (top axis) represented as $|\ V_{TG}\text{-}V_{th}\ |$ (where V_{th}=2.4 V for n$\leq$0, V_{th}=1.05 V for n$\geq$0). (c) Metric: Positions of E$^{'}$ and $A_1^{'}$ peaks as a function of charge density (n, bottom axis) and applied gate voltages (V_{TG}) (top axis) represented as $|\ V_{TG}\text{-}V_{th}\ |$ (where V_{th}=2.4 V for n$\leq$0, V_{th}=1.05 V for n$\geq$0). (d) Metric: Relative positions of 2LA (M), E$^{'}$ and $A_1^{'}$ peaks as a function of charge density (n, bottom axis) and applied gate voltages (V_{TG}) (top axis) represented as $|\ V_{TG}\text{-}V_{th}\ |$ (where V_{th}=2.4 V for n$\leq$0, V_{th}=1.05 V for n$\geq$0). 47

Abbreviations

2D	...	two-dimensional
TMDs	...	transition metal dichalcogenides
NIR	...	near-infrared
CW PM	...	continuous wave photomodulation spectroscopy
Tr-ARPES	...	transient angle-resolved photoemission spectroscopy
PMMA	...	poly(methyl methacrylate)
CCD	...	charge-coupled device
PIA	...	photo-induced absorption spectroscopy
EDLT	...	electric double-layer field-effect transistors
PLLA	...	poly(L-lactic acid)
PDMS	...	Polydimethylsiloxane
rpm	...	Revolutions per minute
PS-PMMA-PS	...	polystyrene-PMMA-polystyrene
EMIM	...	1-ethyl-3-methylimidazolium
TFSI	...	bis(trifluoromethylsulfonyl)imide
CPG	...	charge photogeneration
VB	...	valance band
CB	...	conduction band
PB	...	photobleaching
PA	...	photoinduced absorption
BGR	...	band-gap renormalization

Chapter 1

Introduction

Layered materials exhibit remarkable properties owing to their quasi-2D nature. In particular this class of materials displays strong optical effects, making them promising candidates for application in future optoelectronic devices. This thesis focuses on the interaction of the layered materials with incident optical radiation, with the focus being on few-layer MoS_2 and monolayer of WSe_2 in the field-effect transistor geometry. Interest in TMD semiconductors such as MoS_2 and WSe_2 stems from their stability in ambient conditions, relative ease of fabrication and strongly bound excitonic states in visible or NIR wavelength range.

The main photoexcited species in the MoS_2 semiconductor are excitons with binding energy around 100 meV. Questions connected to the strong exciton binding energy, which are addressed in this thesis, are: - What is the mechanism of charge carrier photogeneration in the excitonic material? - Is there any mark of many-body interaction and how does it reveal in the optical response? I address these questions using time-resolved absorption spectroscopy.

Strong carrier doping can modify carrier-phonon interaction and drastically change phonon spectra in a material. We made an attempt to answer on the questions: - In which way strong carrier doping influence phonon spectra in WSe_2? - Can changes in the phonon spectra be used for characterization the doping level in WSe_2? Raman spectroscopy was used for answering on these questions.

1.1 Excitons in Semiconductors

1.1.1 Excitons in Bulk Semiconductors

An electron and a hole in a semiconductor can form a bound state due to their Coulomb attraction; this state is called an exciton. Excitons show up as strong absorption lines below the absorption in the continuum (inside the band-gap). Looking at the exciton as positronium or hydrogen atom its energy can be represented as [1]:

$$E_n^{3D} = E_g - \frac{E_b^{3D}}{n^2}, \tag{1.1}$$

where $E_b^{3D} = \frac{\mu e^4}{32\pi^2\hbar^2\varepsilon^2\varepsilon_0^2}$ or if we introduce the exciton radius as $a_b = \frac{8\pi\hbar^2\varepsilon\varepsilon_0}{\mu e^2}n^2$: $E_b^{3D} = \frac{e^2}{4\pi\varepsilon\varepsilon_0 a_b}$, where μ is the excitonic effective mass, ε is the crystal dielectric constant, E_g is the band-gap energy. For example, for excitons in bulk GaAs ($\mu = 0.0591$, $\varepsilon = 12.93$)

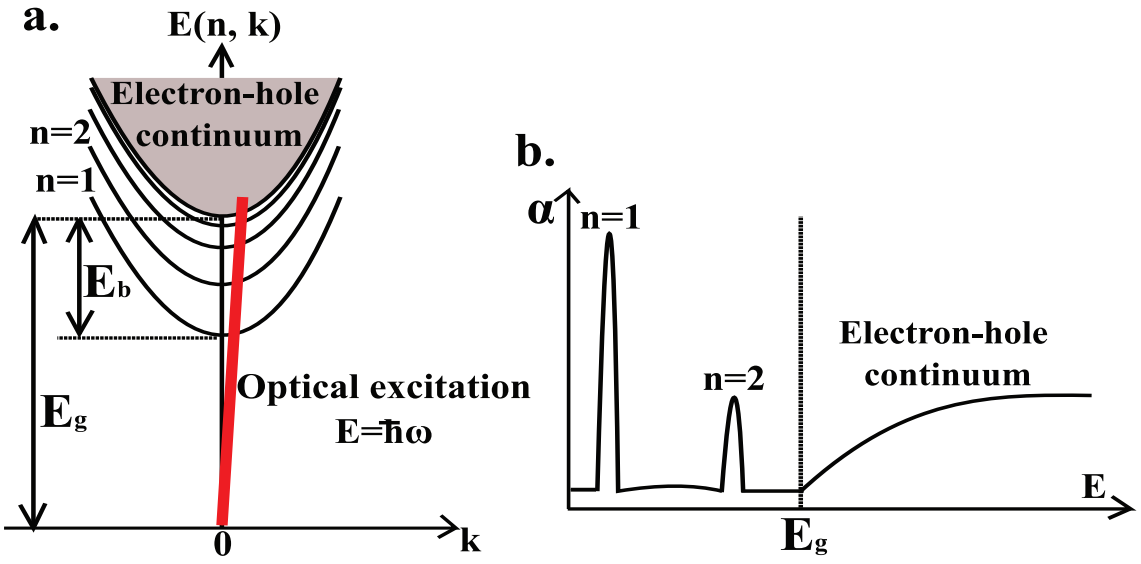


Figure 1.1: a. Schematic of optical excitation of a semiconductor and creation of excitonic bands. b. Semiconductor typical absorption spectrum.

a_b=14 nm, E_b=4.2 meV. Fig. 1.1 shows the dispersion relation for different exciton states. The point E(n,0) = 0 indicates the unexcited semiconductor, i. e. the valence band is filled and the conduction band is empty. The parabolas with indexes n = 1, n = 2, etc. are the different exciton states, which are red-shifted with respect to the continuum states by the exciton binding energy E_b/n^2. The photon with energy E_1 can excite an exciton in the state n=1. There are two types of excitons: Frenkel or molecular excitons, which are strongly localized (Bohr radius on the order of, or smaller than the lattice unit cell length; such excitons can be found in organic semiconductors) and have binding energy about hundreds meV; Wannier-Mott excitons with binding energy ∼ few meV and electron-hole distance of tens of lattice constants. The band structure of an indirect semiconductor is

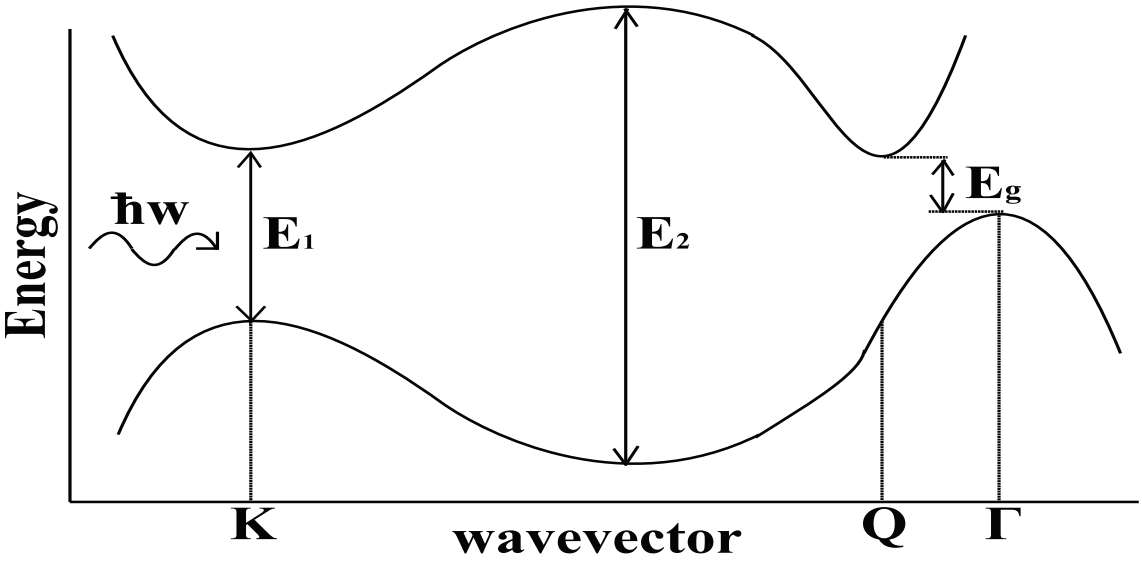


Figure 1.2: Schematic drawing of an indirect-gap semiconductor band structure.

shown in Fig. 1.2. The indirect band-gap is between the Γ and Q points of the Brillouin

zone and the direct band-gap is at the K point. The minimum of the conduction band lies at the Q point, the maximum of the valence band lies at the Γ point; so the semiconductor with band structure as in Fig. 1.2 is an indirect band-gap semiconductor. The difference in energy between the conduction band minimum and the valence band maximum is the band-gap energy. However, transitions that are not vertical in the band structure absorb very weakly. Hence excitations from the valence to the conduction band are strong for photon energies between E_1 (the lowest) and E_2 (the highest vertical energetic distance between the valence band and the conduction band), with the onset energy E_1 being larger than the indirect bandgap E_g. Again, excitons give rise to sharp absorption resonances below E_1.

1.1.2 Excitons in Quasi-2D Semiconductors

The quantum properties of a material emerge when the thickness of the material at least in one dimension is equal or less than a few de Broglie wavelengths of a carrier [2] $x \leqslant \sqrt{\frac{\hbar^2}{m^* kT}}$, where m^* is the effective mass of carrier, k is Boltzmann constant, T is temperature. At room temperature and for $m^* = 0.1m_0$, m_0 is the mass of a carrier: x$\leqslant$5 nm. The quantum properties of a layered material can be reached by making it thin using mechanical exfoliation or growing atomically thin flakes; or by creation of potential barriers by using materials with different band-gaps like in a heterostructure. In the quasi-2D semiconductors the electron and hole wavefunctions are localized in a layer (2D dimensions) and almost do not penetrate into the neighboring layers. So we can estimate that the electron is confined to the plane and its motion is quantized in the direction perpendicular to the plane, i. e. its properties and the material parameters depend on the direction. The energy of an exciton confined with infinitely large potential in one direction is [3]:

$$E_n^{2D} = E_g^{2D} - \frac{E_b^{2D}}{(n-1/2)^2}, \tag{1.2}$$

where E_g^{2D} is the band-gap energy, which is changed under confinement, E_b^{2D} is the Rydberg energy of exciton. For the infinite potential: $E_b^{2D} = 4E_b^{3D}, a_b^{2D} = \frac{1}{2}a_b^{3D}$. In reality, rather than a factor 4 between the 2D and 3D binding energies, factors in the range 2-3 are observed. In the 2D system exciton states with n>1 approach the electron-hole continuum faster than in the 3D system.

1.2 Structure and Physical properties of TMDs

1.2.1 Structural properties

Transition metal dichalcogenides (TMDs), such as the bulk MoS_2 are layered compounds where the layers are held together by van der Waals forces [3], [4]. As shown in Fig. 1. 3 each MoS_2 layer consists of an atomic plane of Mo, which is sandwiched between two atomic planes of S.

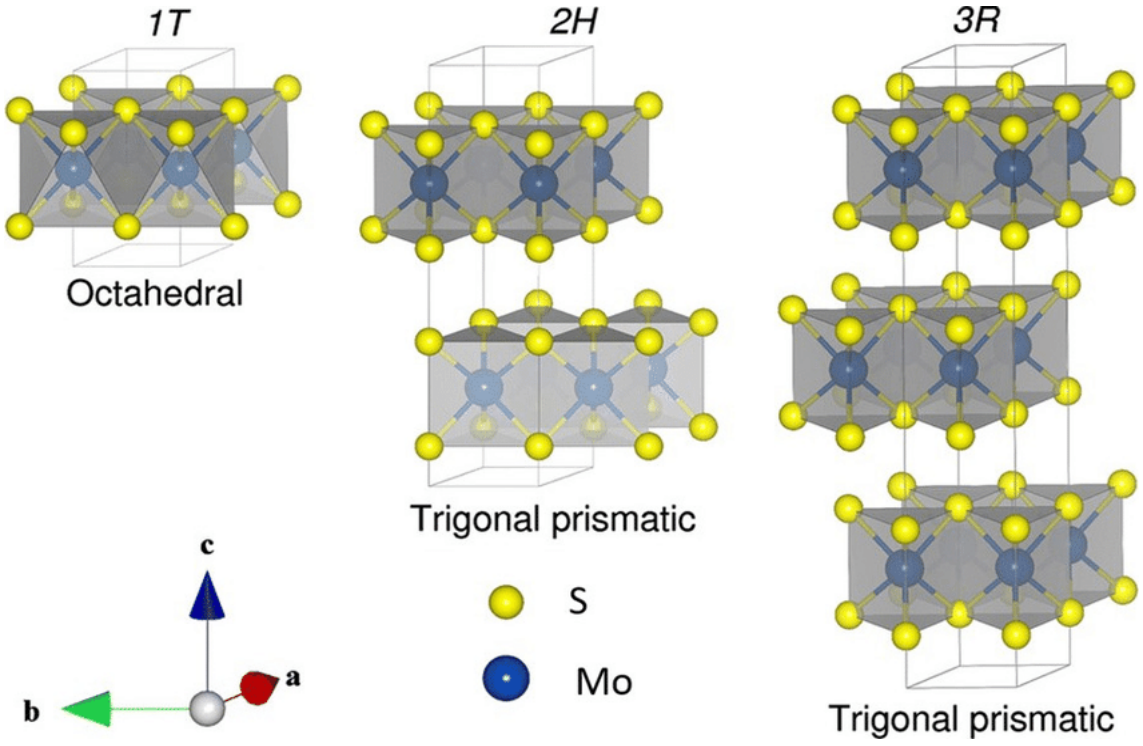


Figure 1.3: Schematic of 1T-, 2*H*-, 3*R*-MoS_2 polymorphs.

Within the layer each atom of Mo is surrounded by six atoms of S in a trigonal prismatic (*H*) or octahedral (*T*) coordination, forming a 2D hexagonal lattice. In the prismatic (*H*) configuration the chalcogen atoms in both planes are vertically aligned forming ABA stacking (A and B denotes the chalcogen and metal atoms planes respectively), in the octahedral (*T*) configuration one of the sulfur layers is shifted (i.e. is rotated by 30°) compared to the other resulting in ABC stacking (A, C are the chalcogen atom planes, B is the metal atom plane) (see Figure 1.3). Depending on the different ways of stacking between layers in a crystal, MoS_2 has several different polymorphs (see Figure 1.3). There are two stable polymorphs of bulk MoS_2: the 2*H* phase and the 3*R* phase. The unit cell of the 2*H* phase is composed of a double-layer and the 3*R* phase is formed by three layers. The bulk crystal 2*H*-MoS_2 belongs to the D_{6h} point symmetry group, the monolayer has the D_{3h} symmetry. The spatial inversion symmetry is absent in a monolayer and the 3*R* phase (and in all odd numbers of layers in the MoS_2 crystal) but is restored in bulk 2*H*-MoS_2. The conduction and valence bands are formed by hybridization of the d orbitals of Mo and p orbitals of S; the p orbitals of S are fully occupied with electrons, the d orbitals of Mo keep 2 electrons (Fig. 1.4a) [5].

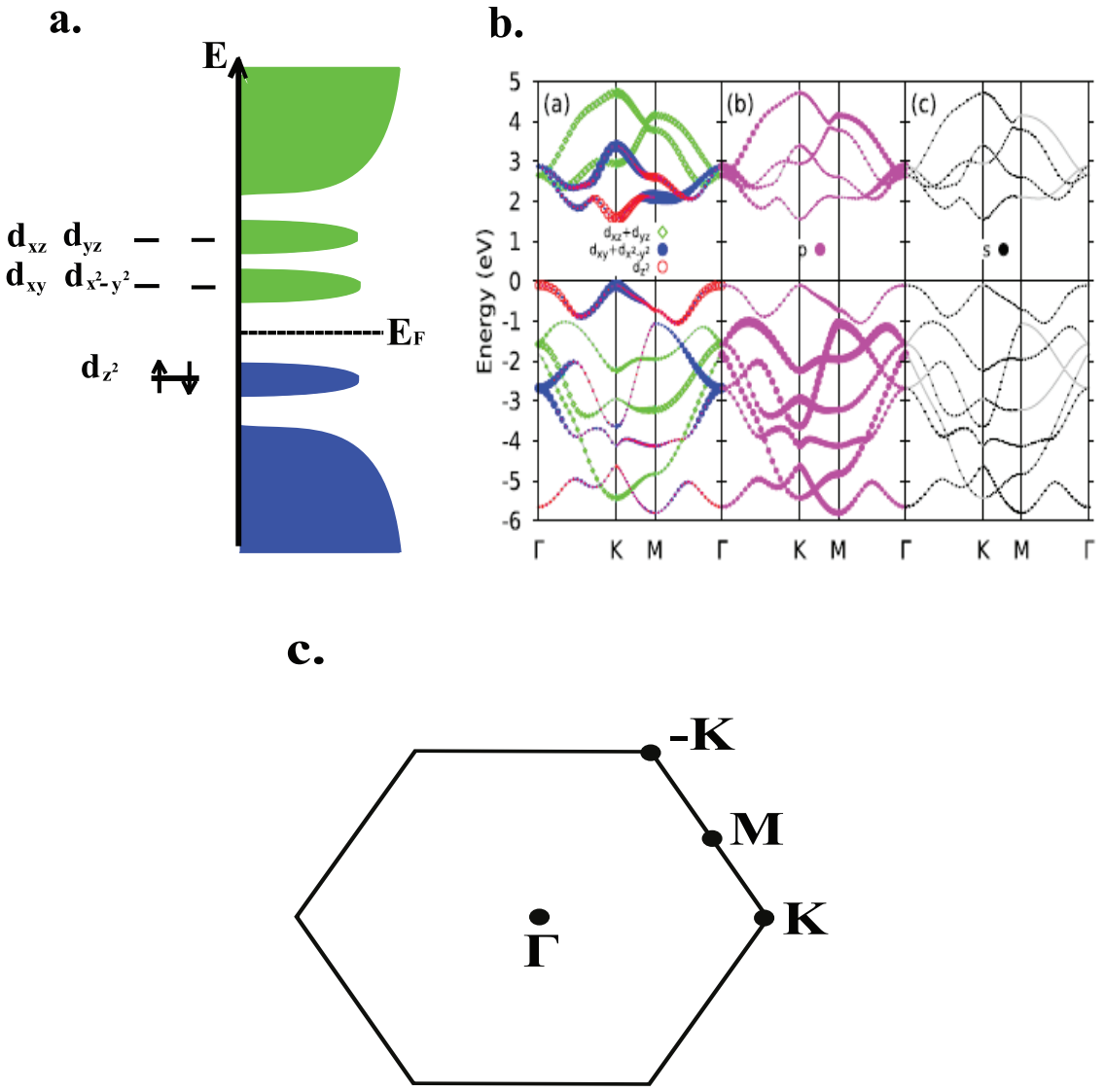


Figure 1.4: a. Band structure in the terms of metal atomic orbitals [5]. b. Relative contribution of individual atomic orbitals to the band structure of MoS_2. Image taken from [6]. c. Brilloin zone of MoS_2.

Due to the trigonal prismatic configuration of Mo, the d orbitals split into three bands which are formed by three groups of orbitals: d_{z^2}; d_{xy}, $d_{x^2-y^2}$; d_{xz}, d_{yz}. The electrons fully occupy the d_{z^2} orbitals, giving rise to the semiconducting nature of MoS_2. The monolayer MoS_2 is a direct band gap semiconductor (the band gap is ∼1.8 eV) (Fig. 1.5) with the minimum of the conduction and the maximum of the valence band at K and -K points of the Brillouin zone. In contrast to the monolayer MoS_2, the bulk MoS_2 is an indirect band-gap semiconductor (the band-gap is 1.3 eV) with the maximum of the valence band at the Γ point and the minimum of the conduction band at the Q point (which is half-way between the Γ and the K points; also known as L point, (Fig. 1.5)).

The rearrangement of the electronic band structure, i. e. changing nature of the electronic band-gap from an indirect to a direct one upon decreasing the MoS_2 thickness can be qualitatively described using a tight-binding model. The tight-binding model determines the atomic orbital composition of the electronic states at the different points of the

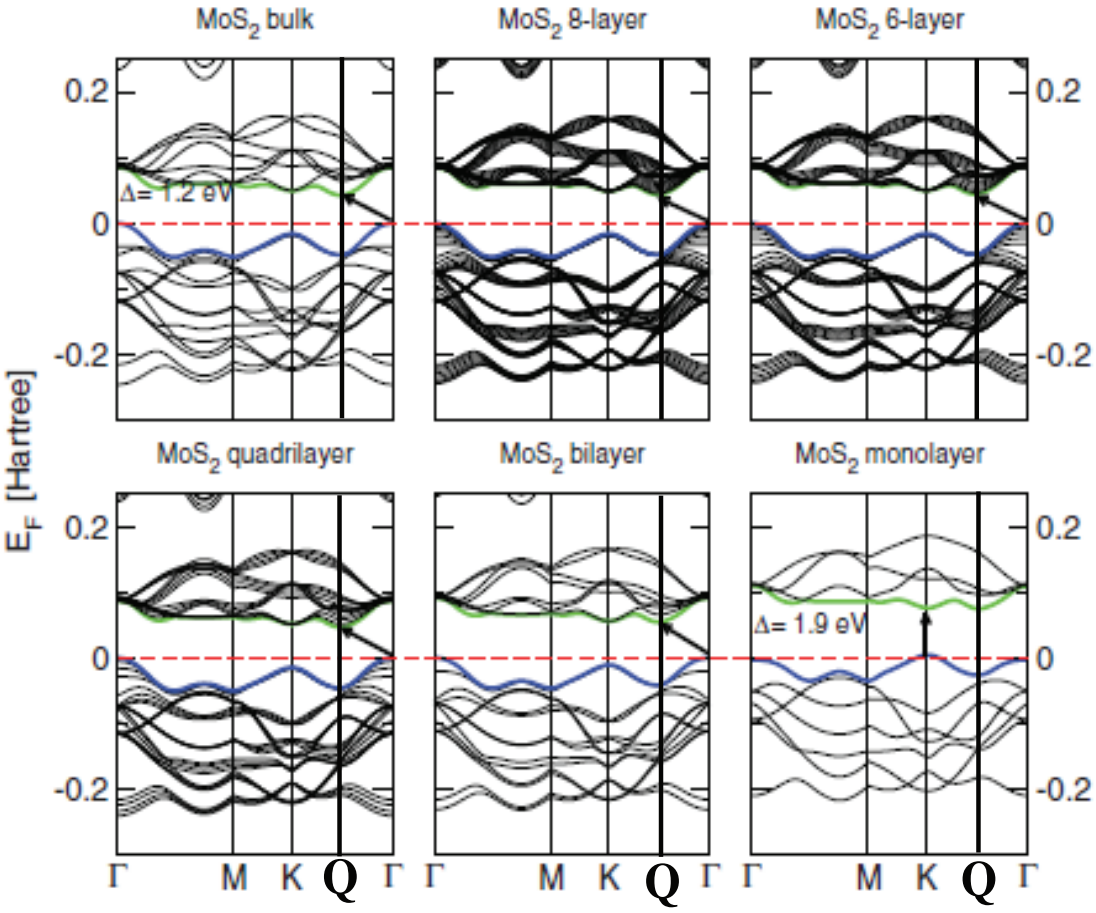


Figure 1.5: DFT calculation of the evolution of the MoS_2 band structure upon decreasing thickness. During decreasing thickness a transition from an indirect band-gap semiconductor to a direct one occurs. The horizontal dashed lines indicate the Fermi level. Image taken from [7]

Brillouin zone. For graphene the electronic structure was successfully described by the tight-binding model, taking into account just one tight binding parameter – the nearest-neighbor carbon-carbon hopping. Hamiltonians for multilayer graphene can be built using a monolayer tight-binding model adding additional hopping parameters between layers [8]. For the monolayer MoS_2 the electronic states at the valence band edge at the Γ point contain Mo d_{z^2} orbitals and S p_z orbitals (Fig. 1.4b), the valence band edge at the K point contain Mo $d_{x^2-y^2}$+d_{xy} orbitals and S p_x+p_y; the conduction band edge at the K point contains of Mo d_{z^2} and S p_x+p_y, the conduction band edge at the Q point contain of Mo d_{z^2} and S p_z, p_x+p_y [6], [9]. To build a tight-binding model for multilayer MoS_2 the tight-binding model for monolayer should taken together with interlayer hopping. The main role will be played by interlayer hopping between external S planes of each MoS_2 layer. The interlayer coupling in the multilayer system is driven by p_z-p_z hopping whereas $p_{x/y}$-$p_{x/y}$ and $p_{x/y}$-p_z hopping is negligible. This results in orbital-selective interlayer splitting of the energy levels, being larger for the states at the Γ and the Q points than for the states in the conduction and valence bands of the K point. In the optical measurements the optical band-gap is probed. For the excitonic materials with large exciton binding energy (like in monolayer MoS_2) the optical gap is strongly renormalized by large exciton binding energy [10].

The heavy Mo atoms in MoS_2 lead to strong spin-orbit interaction. The signature of the large (150 meV) spin-orbit splitting in the valence band at the K point of the Brillouin zone can be visible in the absorption spectrum as A and B excitons [3]. The spin-splitting in the conduction band is much weaker (few meV)[11]. The spin-splitting in the valence and conduction band for molybdenum-based compound have the same sign and opposite sign in the tungsten-based compounds (Fig. 1.6). The peculiar properties in TMDs appear

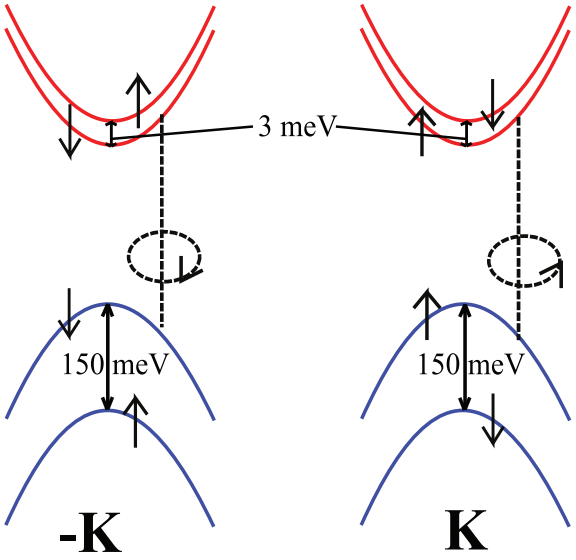


Figure 1.6: Spin-orbit splitting in the conduction and valence band near the K and -K points. Spin-polarized bands are indicated by up (spin-up) and down (spin-down) arrows. The dashed circles are used for describing left and right photon polarization.

at the boundary of the hexagonal (first) Brilloin zone (see Fig. 1.4c) at the two inequivalent points (K and -K). The absence of inversion symmetry ($E(k,\uparrow) \neq E(-k,\uparrow)$) and presence of time-reversal symmetry ($E(k,\uparrow) = E(-k,\downarrow)$) gives rise to the momentum dependent spin splitting for odd number of layers material [12]. The valleys at the K and -K points can be individually addressed by photoexcitation with circularly polarized light. Spin-resolved photoemission measurements [13] showed that the upper valence bands at the K point in the bulk material are also spin nondegenerate and the sign of the spins of the electronic bands are opposite in the adjacent layers in the unit cell. It was explained by a very strong valley-dependent spin splitting in each layer. That splitting suppresses hybridization of adjacent layers' states. Moreover, the signs of spins are reversed at the -K point, confirming the preservation of time-inversion symmetry in the bulk form.

1.2.2 Raman and Photoluminescence Spectroscopy

There are six atoms per elementary cell of bulk MoS_2. This yields 15 optical vibration modes in the following irreducible representations: $A_{1g} \oplus A_{2u} \oplus 2B_{2g} \oplus B_{1u} \oplus E_{1g} \oplus E_{1u} \oplus 2E_{2g} \oplus E_{2u}$ [14]. A_{1g}, E_{2g}, E_{1g} are Raman active modes and A_{2u}, E_{2u}, E_{1u} are infrared active modes. The schematic representation of the above mentioned modes is presented in Fig. 1.7. Raman active modes in MoS_2 have a strong dependence on the number of layers. The correspondence between the Raman frequencies and the number of layers was realized by comparing Raman with atomic force microscopy measurements [15]. The high frequency A_{1g}, E^1_{2g} and low frequency E^2_{2g} (shearing mode), B^2_{2g} (layer breathing mode) [16] phonon modes are used to characterize the thickness. The frequency

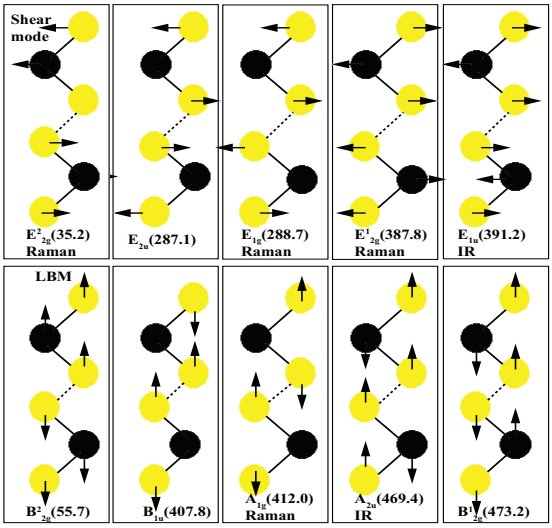


Figure 1.7: Possible Raman and IR modes in MoS_2. Image adopted from [14]

of the A_{1g} mode grows with increasing number of the layers due to interlayer interaction which increases the restoring force between layers; the frequency of the E^1_{2g} mode decreases with increasing number of layers [15]. The "anomalous" decreasing frequency of the E^1_{2g} mode in bulk crystals is connected to a weakening of the nearest neighbor Mo-S force constant. There are two reasons for such weakening: a slight redistribution of charge density when neighboring levels are present and Mo-S bonds are slightly longer in bulk. The A_{1g} and E^1_{2g} modes moving in opposite directions with increasing number of layers [15] make the distance between these modes in the Raman spectra a reliable measure of the layer number (Fig. 1.8b). As it was mentioned before, the frequencies of the shear and compression (layer breathing) modes are also thickness dependent. The single-layer MoS_2 doesn't have any signature of low-frequency modes but with increasing number of the layers the frequency of the layer breathing mode increases for the Nth phonon branch and decreases for the 2nd phonon branch and the frequency of the shear mode increases for the Nth phonon branch with dominant weight [16]. Decreasing the number of layers in MoS_2 leads to rearrangement of the band structure and a transition from indirect band-gap semiconductor (bulk) to direct band-gap semiconductor (monolayer).

It is well known that the change in the electronic structure of materials has a strong influence on its optical response. A bulk crystal does not have photoluminescence due to the low probability of the two-particle process, necessary for recombination across the indirect gap. In the monolayer form the photoluminescence quantum yield increases by a factor of 10^4 (Fig. 1.8a), but it is still very low due to quenching of light emission by intrinsic defects (S-vacancies). A photoluminescence quantum yield near unity was obtained [17] by passivating and repairing electronically active defects due to treatment of the monolayer with an organic superacid. The origin of photoluminescence in MoS_2 is recombination of excitons and trions (for the doped samples).

1.2.3 Light Absorption, Excitons and Trions

The optical band-gap in the bulk (1.3 eV) and monolayer (1.8 eV) MoS_2 lies in the near-infrared and visible optical range. MoS_2 is an excitonic material, so the value of the

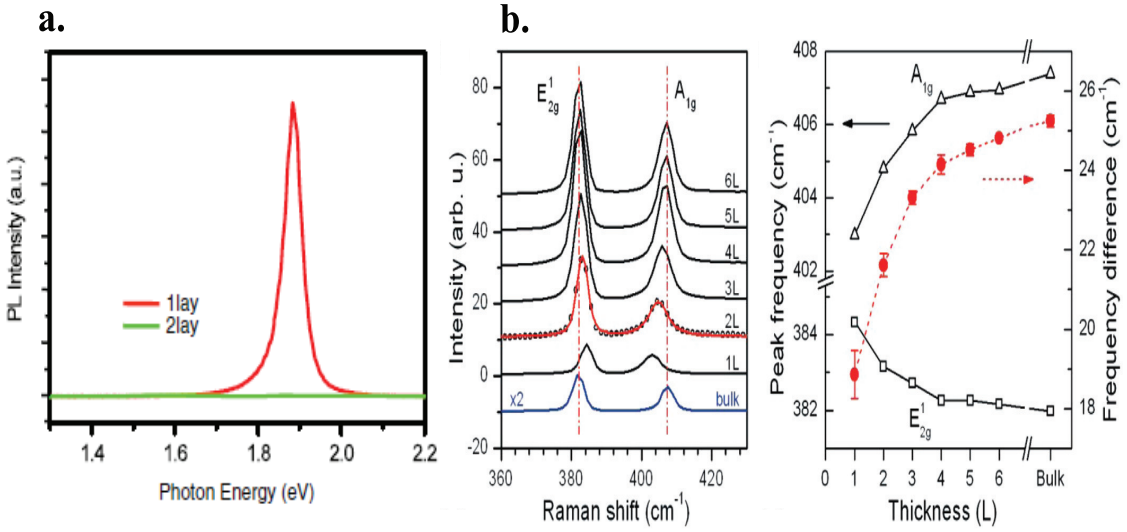


Figure 1.8: a. Photoluminescence spectrum taken from 1- and 2-layer MoS_2 samples. Image taken from [4]. b. Raman spectra of in-plane(E^1_{2g}) and out of plane(A_{1g}) modes taken from MoS_2 samples with different number of layers. Shift of both modes with thickness and frequency difference $\omega(A_{1g}) - \omega(E^1_{2g})$ depending on layer number. Image taken from [15]

quasiparticle band-gap is higher than the optical gap by the exciton binding energy. The value of the absorption coefficient in the visible photon energies range 1.6-3 eV in the bulk is 0.1-0.6$\times 10^6$ cm^{-1} [3]; the monolayer has an absorbance of 5-10% in a thickness of 6.5 Å and the absorption coefficient is 1-1.5$\times 10^6$ cm^{-1} [4]. The absorption coefficient for bulk is 2-3 times lower than for the monolayer, which reflects the non-linear dependence of the absorbance versus the number of layers. The dominant features in the absorption spectra are the exciton resonances. In MoS_2 excitons arise from the electronic transition at the K(-K) points. The binding energies of the A and B excitons depend on their reduced masses, which are different, so the binding energies are also different. Also additonal peaks of C and D excitons are visible in the absorption spectra. The C exciton emerges from electronic states in the zones where valence and conduction zones are nested in the Γ - Q direction of the Brillouin zone [18]. A definitive assignment of the D exciton is still missing.

Excitons in 2D materials can be classified as dark, which cannot be excited with light in the dipolar approximation, or bright, which are excited with light (Fig. 1.9). In MoS_2 the dark A(B) excitons are excitons formed by a hole from the highest (second highest) valence band and an electron from the lowest (second lowest) conduction band; the electron and hole spin projection must be the same (Fig. 1.9). Excitons in monolayer MoS_2 are visible even at room temperature due to the high exciton binding energy caused by the reduced dimensionality (i.e. confinement of the exciton wave function in the layer) and weak dielectric screening. Solving the hydrogen model for the idealized two-dimensional case, one obtains a binding energy which is four times that of the conventional, three dimensional case. The thickness of less than 1 nm of the monolayer makes it sensitive to its surrounding, i.e. electronic screening changes dramatically. The exciton binding energy in the bulk is described by the Wannier-Mott model; such approximation does not take into account screening nonlocality. In 2D the screening is nonlocal in real space and it depends on the distance between the electron and the hole and the polarizability of the material [20]. Basically, the Coulomb field lines extend outside the material, where no

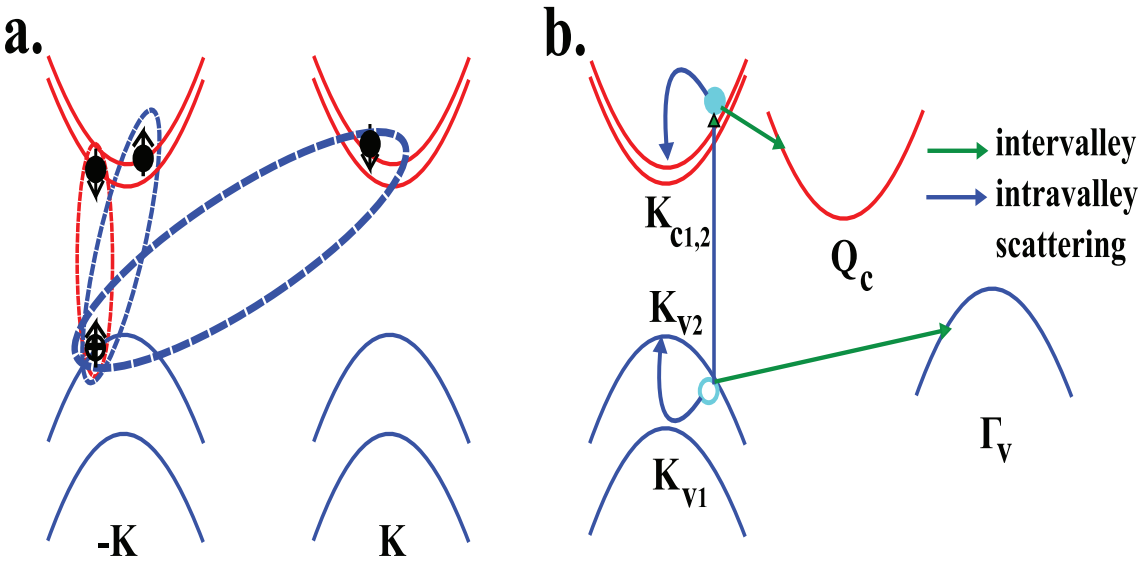


Figure 1.9: a. Excitons in both valleys using the exciton basis. Empty circle is a hole, black circle is an electron; up and down arrows indicate particles with spin-up and spin-down; red dashed circle reperesents bright excitons, blue dashed circle reperesents dark excitons. b. The ultrafast intravalley and intervalley relaxation of carriers. Image adopted from [19].

screening in the case of vacuum or less screening in the case of substrate is possible [21]. The quantum confinement and reduced screening increase the exciton binding energy to the value ~ 0.5 eV in monolayer [22] and ~ 0.1 eV in the bulk [23]. Due to the suppressed screening the exciton does not need to be localized to have such large binding energy and its Bohr radius is ~ 1 nm, so it is of Wannier-Mott type. It was shown [21] that the excitonic series deviates from the 2D hydrogen-like model. Taking into account that the different excitonic Rydberg states have different spatial distribution, the effective screening is different for each of the states. Surprisingly, even at room temperature, the absorption spectra of the bulk crystal also contain peaks of excitons, which are slightly red-shifted compared to the monolayer [24]. The reason for this is that the electronic states at the K(-K) points remain almost unchanged upon adding MoS_2 layers [6]. The binding energy of excitons in the bulk material decreases due to exciton delocalization in the direction perpendicular to the layer.

In a nearly neutral monolayer quasiparticles such as trions [25] and biexcitons ([26], [27]) were observed. The trion is a three-particle excitation, i.e. a positively or negatively charged exciton (Fig. 1.10b). The binding energy of trions (the difference between the trion and exciton energies) is ~ 30 meV [28] (Fig. 1.10c), which is larger than in semiconductor quantum wells as a result of the strong Coulomb interaction and weak dielectric screening. The trion can be imagined (Fig. 1.10a) like an exciton with spinning around it a third charged particle on the distance 2.5 nm from the equally-charged particle for decreasing Coulomb repulsion [29]. The presence of a third particle in the trion structure gives opportunity for the trion with finite momentum to couple to light, so under the radiative recombination excess momentum is transferred to the remaining electron/hole. In principle, both excitons A and B should have their own trion (A^-, B^-); to the best of my knowledge a B^- trion has not been yet experimentally observed. Trions can also be created in natural doped samples; the manipulation of the number of trions can be done by tuning the electron density in a MoS_2 transistor [28]. No trion signature has been reported in bulk-like samples.

The biexciton is a quasiparticle which consists of two excitons (Fig. 1.10a). The biex-

citons form in semiconductors with high density of excitons and usually are observed in photoluminescence (in photoluminescence the line intensity of the biexciton emission grows as the square of the light fluence) by tuning the excitation fluence; in ordinary semiconductors the biexciton binding energy is few meV. Unlike trions, biexcitons, like excitons, are composite bosons. In WSe_2 the binding energy of biexcitons is 52 meV [27], it is higher than for trions as a result of the more compact biexciton geometrical structure.

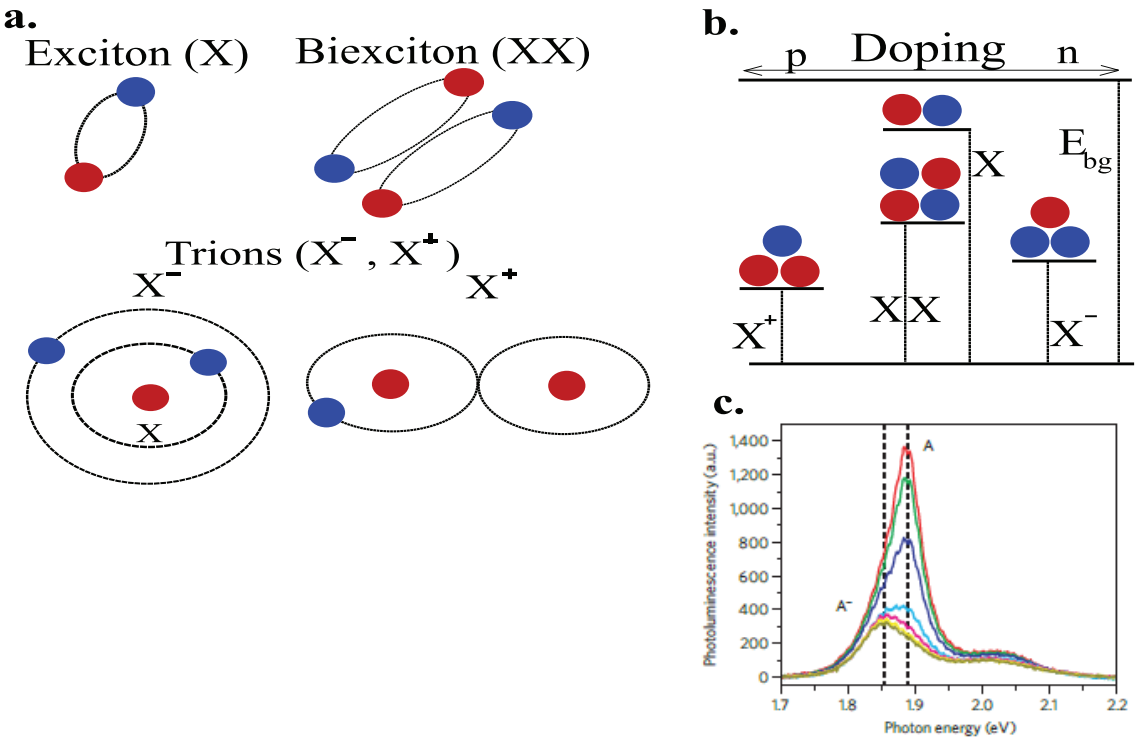


Figure 1.10: a. Artistic drawing of exciton (X), trions (X^- – similar to hydrogen ion H^-, X^+ – similar to ionized hydrogen molecule H_2^+) and biexcitons (XX). b. Schematic of electron and hole configuration in neutral and charged excitons (trions) versus the doping of the crystal. c. Photoluminescence from monolayer MoS_2 upon doping a new trion (A^-) peak appears. Image taken from [28].

1.2.4 Ultrafast Carrier, Exciton and Many-body dynamics

Ultrafast spectroscopy is a useful tool for studying the real-time dynamics of excitation inside a material. A broad range of techniques were used for the research, such as differential absorption spectroscopy [30], photoluminescence time-resolved spectroscopy [31], time- and angle-resolved photoemission spectroscopy [32]. The peculiar properties of the band structure of mono- and few-layer MoS_2 suggest that there are three different interesting regimes of the excitation energy: above the optical gap, resonantly to excitons; and below the gap. The excitations with different energies drive processes at different points in the Brillouin zone with the generation, relaxation and recombination of different type of quasiparticles such as free electrons and holes, weakly-bound electron-hole pairs and tightly-bound electron-hole pairs, so-called excitons.

In the following text I will discuss the processes after excitation of quasiparticles in more details. At negative time delays before the arrival of the pump pulse, the electron

distribution in the system is described by the Fermi-Dirac distribution. Upon arrival of the pump pulse a deviation from the Fermi-Dirac distribution is developed. Then, excited hot electrons relax through electron-electron scattering, electron-phonon scattering, electron-impurity/defect scattering and scattering with another elementary excitations and the Fermi-Dirac distribution recovers. Usually, electron-electron scattering is ultrafast ($\sim$ 100 fs), while the electron-phonon scattering time lies in the picoseconds range. The exact time interval for the different types of scattering depends on the systems under investigation and can be different for the electrons and holes. Note that, all optical time-resolved methods give, as a direct measurement result, just an amplitude of a photoinduced signal and a lifetime of a population (in special cases an information about spectra can be obtained). Investigation of electron (hole) dynamics in mono- and few-layer samples [33] has shown that upon pumping with the energy 2.74 eV and probing with the energy 1.37 eV the short-lifetime population dynamics does not have any meaningful dependence on the layer number and the relaxation time of the long-lifetime population is slowing down with increasing number of layers. The short-lifetime positive signal in the bulk-like samples is attributed to a decrease of absorption by midgap defect states due to the pump induced ionization of those states. The positive part of the signal is absent in the monolayer, which is consistent with no measurable photoluminescence or absorption at 1.37 eV and the absence of the optically active defect states.

The long-time dynamics in few-layer samples is described as defect-assisted recombination, which is more effective in the surface layers than in the inner layers. The presence of more defects at the surfaces can be explained by sulfur vacancies with low formation energies. The exciton and trion features are observed by ultrafast absorption [30] and photoluminescence spectroscopy [31] but the free carrier absorption is masked under strong excitonic and trionic bands. One way to investigate the free carrier dynamics is using time- and angle-resolved photoemission spectroscopy (Tr-ARPES); useful and complementary information to ultrafast absorption and photoluminescence spectroscopy about the band structure and its change upon the excitation can be obtained. The early data on the hot-electron relaxation through electron-electron scattering in bulk MoS_2 studied by time-resolved two-photon photoemission spectroscopy [34] shows that the relaxation time of hot electrons is $\leq$ 60 fs and their inverse lifetime (decay rate) depends linearly on the excess energy above the conduction-band minimum. Measurements on monolayer samples on a gold substrate with Tr-ARPES [32] determined an ultrafast (50 fs) extraction of excited free carriers via gold. Such ultrafast extraction was explained by the Auger-type electron-electron interactions. The excited electrons in the conduction band can easily find a hole in the gold states continuum while simultaneously exciting an electron-hole pair in the Fermi sea of the metal.

Before starting an overview of the available literature on the time-resolved pump-probe spectroscopy it should be mentioned that there are a multitude of ultrafast phenomena: the carrier-carrier and carrier-phonon scattering; the band gap renormalization; band filling; many body interaction, such as exciton-carrier and exciton-exciton scattering. The carrier-carrier and carrier-phonon interaction in a five-layer sample was investigated using pump-probe spectroscopy with 10 fs resolution [35]. It was claimed that just the free carriers' ultrafast dynamics was observed for the fluences which were used in experiment. The evolution of an initial excited nonthermal carrier distribution towards an equilibrium Fermi-Dirac distribution occurred during 15 fs through carrier-carrier scattering. The temperature dependence of the ultrafast relaxation time suggests that carrier-phonon scattering also contributes to the carrier thermalization. The slow decay components ($\sim$0.64 ps and 0.54 ps for the A and B excitons respectively) are presented in the population decay traces and suggested to be due to carrier cooling via phonon emission. It was suggested that

the A_{1g}, E^1_{2g} phonons take part in the electron cooling process. It is known, that electronic and optoelectronic characteristics are governed by carrier dynamics; for example carrier-carrier and carrier-phonon scattering limit the mobility in the devices. In Reference [35], electron and hole dynamics are indistinguishable, because the pump-probe spectroscopy is sensitive to the band filling processes, induced by both the electron and holes populations. In the work [19] separate dynamics for the electrons and holes were measured. It was shown that together with the ultrafast relaxation through the electron-electron scattering an intravalley and an intervalley relaxation channels exist (see Figure 1.9b). The intravalley relaxation of the electrons at the K point occurs dominantly by acoustic phonons. The intervalley scattering of the electrons from the K to the Q point occurs by E^1_{2g} LO phonons; scatttering of holes from K to Γ occurs by the acoustic phonons.

One peculiar physical phenomenon connected to enhanced many-body interaction in the monolayer MoS_2 and other members of the family TMDs is the band-gap renormalization and the Mott transition. In Reference [36] the band-gap renormalization effect, i.e. shrinking of the band-gap under low photoexcited charge density was discussed. The origin of the band-gap renormalization is the enhancement of the electronic screening which leads, besides band-gap shrinking, also to the lowering of the exciton binding energy. The measurements [37] on a bilayer WS_2 in the high carrier-density regime showed almost complete exciton peak disappearance and build up of a feature with negative differential absorption at photon energies below 1.8 eV. The exciton peak disappearance was explained as a sign of the Mott transition, i.e. a transition from an insulating excitonic regime to an electron-hole plasma. The presence of a hot electron-hole plasma gives rise to such phenomena as population inversion and band-gap renormalization of the order of 500 meV. The hot electron-hole plasma leads to a quasi-Fermi level shift inside the conduction and valence bands and carrier population inversion builds up near the band edges [37]. All these phenomena are pump-induced, transient with picosecond lifetimes and the recovery of the equilibrium optical properties occurs in hundreds of picoseconds. It should be mentioned here, that at high excitation fluence a fermionic nature of excitons should be taken into account. Besides the Mott transition, the high pump fluence can trigger generation of many-body particles, such as biexcitons. The biexciton was identified in [27] as a sharp peak in the photoluminescence spectra. The intervalley biexcitons [26] with binding energy ∼40 meV in monolayer MoS_2 were formed by A and B excitons. One more example of a many-body state in MoS_2 are trions. In transient spectroscopy measurements on WS_2 [38] the prediction was made that the excitons, generated by the pump pulse, dissociate on the defects of a crystal or a substrate, leaving electrons in the conduction band to bind with electron-hole pairs generated by the probe pulse to form negative trion states. The study of exciton dynamics in suspended and substrate-supported monolayer and few-layer MoS_2 at room temperature was conducted in Reference [30]. The mono-, few-layer and thick samples exhibit different dynamics. The dynamics in mono- and few-layer samples are faster than in thick samples, which means that all relaxation processes in the bulk occur on a much longer scale than in the thinner samples. An explanation for this is scattering on the surface defects, the number of which per atom is more in the thin than in thick samples. Also, the thin samples are direct band-gap semiconductors, so the interband relaxation is faster at the long time scale. The authors in [30] assigned the fast dynamics to carrier-carrier scattering (2 ps) and carrier-phonon scattering (20 ps) in the thick samples, defect assisted scattering ($\leq$ 500 fs) and interband carrier-phonon scattering (80 ps) out of the light cone in the thin samples; trapping (3 ps) and direct recombination (800 ps) in the thin samples, intervalley scattering (∼2.6 ns) and indirect recombination ($>$ 2.6 ns) in the thick samples. One of the time constants obtained by time-resolved photoluminescence measurements on monolayer MoS_2 [31] excited with 3 eV is $\sim$ 5 ps at 4K and is attributed

to the decay of the non-thermalized exciton. The calculation [39] showed that 3.7 ps, which is close to the experimental 5 ps lifetime, is the intrinsic (at the temperature – 0 K, Q=0 (Q – momentum) of the exciton) radiative decay time of the A exciton. As the temperature is increased, in addition to the 5 ps decay constant a longer photoluminescence decay time(1 ns) component appears.

Chapter 2

Experimental Techniques and Samples Preparation

2.1 Generation of ultrashort laser pulses

According to Fourier transform, the shortest attainable pulse duration (τ) is inversely proportional to the spectral width ($\Delta\nu_s$), $\Delta\nu_s \sim \tau^{-1}$. Therefore, for generation of ultrashort laser pulses a gain medium with a broad gain bandwidth (to amplify light over wide range of frequencies) is needed. The cavity of length L has resonant modes at wavelengths λ for which $n\frac{\lambda}{2} = L$, with n being the mode order. Using $\nu = \frac{c}{\lambda}$, the mode frequencies can be written as $\nu = \frac{nc}{2L}$ and the frequency separation ($\Delta\nu$) between adjacent modes is $\Delta\nu = \frac{c}{2L}$. Hence for a gain bandwidth of $\Delta\nu_s$, $N = \frac{\Delta\nu_s 2L}{c}$ modes are amplified in the cavity. If the modes are not in phase then the intensity shows chaotic fluctuations without forming intense pulses (Fig. 2.1). If, on the other hand, the phases of all N modes are suitably locked with each other, then the light energy inside the cavity concentrates into one pulse of duration $\tau \geq \Delta\nu^{-1}$ (see Fig. 2.2). Therefore the requirement for the generation of ultrashort pulses is to have a lot of modes which form a broad spectrum and are all synchronized with each other.

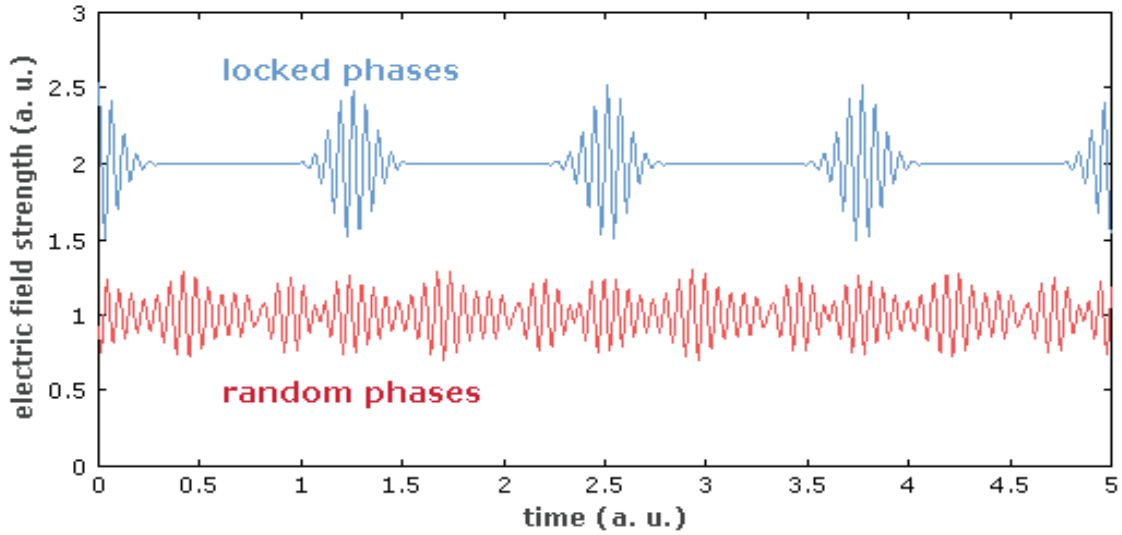


Figure 2.1: The pulses train which were obtained due to many modes generation: pulse phases are locked (blue); pulse phases are random (red). Image taken from Ref. [40]

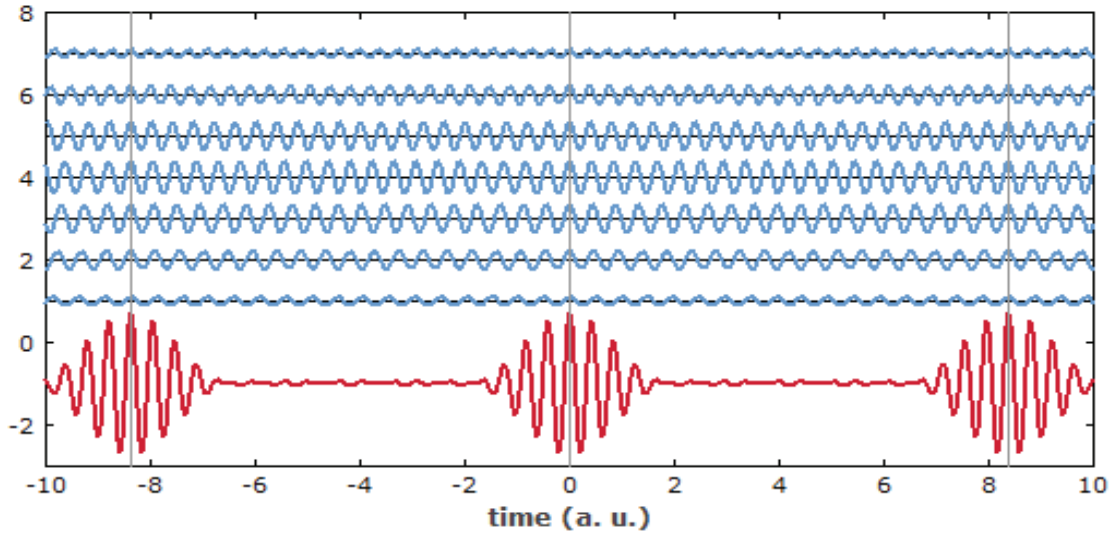


Figure 2.2: Possible modes in the laser resonator (blue) and pulses train when modes are locked. Image taken from Ref. [41]

2.2 Optical nonlinear processes

The interaction of light with a medium is described as an electrical polarization of the medium induced by the electric field of the light. For moderate light intensity (when the amplitude of the electric field $|\vec{E}(\omega,t)|$ is much less than interatomic electric fields, $10^9\ \frac{V}{m}$) the induced polarization depends linearly on the electric field: $\vec{P}(\omega,t) = \varepsilon_0\chi^{(1)}(\omega)\vec{E}(t)$, where $\vec{P}(\omega,t)$ is the polarization of the medium, $\vec{E}(t)$ is the electric field, and $\chi^{(1)}(\omega)$ is the 2nd-rank tensor of the electric susceptibility of the medium at the frequency of the electric field. The electric susceptibility is related to the medium's refractive index: $n = \sqrt{1+\chi^{(1)}(\omega)}$. If $|\vec{E}(t)|$ is comparable to the interatomic Coulomb field, as can be reached by focussing a short laser pulse, the induced polarization is no longer linear in the applied electric field and higher order terms need to be included [42]:

$$\vec{P}(\omega,t) = \vec{P}^{(1)}(\omega,t) + \vec{P}^{(2)}(\omega,t) + \vec{P}^{(3)}(\omega,t) + ..., \tag{2.1}$$

or

$$\vec{P}(\omega,t) = \varepsilon_0[\chi^{(1)}(\omega)\vec{E}(t) + \chi^{(2)}(\omega)\vec{E}(t)\vec{E}(t) + \chi^{(3)}(\omega)\vec{E}(t)\vec{E}(t)\vec{E}(t) + ...], \tag{2.2}$$

Second harmonics generation (SHG) appears due to the second order susceptibility term. However, for centrosymmetric crystals (with inversion symmetry in their crystal structure) such as sapphire, the even order susceptibility terms in Eq. (2.2) vanish. Therefore, typically $Ba_2B_2O_4$(BBO) crystals are used for SHG. The second-order nonlinear polarization has the form: $\vec{P}^{(2)}(\omega,t) = \varepsilon_0\chi^{(2)}(\omega)\vec{E}(t)\vec{E}(t)$. Assuming the light field as a plane wave $\vec{E}(t) = E_0e^{-i\omega t} + c.c.$, we obtain:

$$\vec{P}^{(2)}(\omega,t) = 2\varepsilon_0\chi^{(2)}(\omega)E_0{E_0}^* + \varepsilon_0\chi^{(2)}({E_0}^2e^{-i2\omega t} + c.c), \tag{2.3}$$

where first term describes a static shift, known as optical rectification and second term describes the creation of frequency-doubled wave - second harmonic. If we take into account

that the incident laser field is not a simple monochromatic plane wave, we can expect further second-order three wave-mixing nonlinear processes. If we consider frequencies ω_{p} and ω_{s} from the spectrum of the non-monochromatic pulsed laser, such processes are: sum frequency and different frequency generation, optical-parametric generation and optical-parametric amplification. Not all processes occur at the same time, due to different phase-matching conditions for each effect. I will focus on optical parametric processes. Here, an intense high-frequency wave (pump) imparts its energy to weaker, lower-frequency waves (signal and idler). Two cases can be distinguished: optical-parametric generation (OPG) and optical-parametric amplification (OPA). In the case of OPG an intense pump pulse ω_p amplifies a signal ω_s and idler ω_i wave, which arise from vacuum fluctuation: $\omega_p = \omega_s + \omega_i$. The broad tunability of $\omega_{s,i}$ is achieved via phase-matching. In the case of OPA a weak signal wave ω_s already exists and it is then amplified by an intense pump beam ω_p, the idler wave ω_i is generated in the same process: $\omega_i = \omega_p - \omega_s$ $(\omega_s < \omega_p)$

2.2.1 Supercontinuum generation

In a centrosymmetric crystal the third-order susceptibility $\chi^{(3)}$ is the lowest order non-linearity that needs to be taken into account: $\vec{P}^{(3)}(\omega,t) = \varepsilon_0\chi^{(3)}E^3(t)$. For the monochromatic plane wave $\vec{E}(t) = E_0\cos(\omega t)$: $\vec{P}^{(3)}(\omega,t) = \varepsilon_0\chi^{(3)}(\omega){E_0}^3\cos^3(\omega t)$ or:

$$\vec{P}^{(3)}(\omega,t) = \frac{1}{4}\varepsilon_0\chi^{(3)}(\omega){E_0}^3\cos(3\omega t) + \frac{3}{4}\varepsilon_0\chi^{(3)}(\omega){E_0}^3\cos(\omega t), \tag{2.4}$$

The first term of Eq. (2.4) describes the third-harmonic generation (with frequency 3ω). The second term describes a nonlinear contribution with the fundamental frequency ω. Taking into account also first-order polarization term, the polarization thus becomes: $\vec{P}(\omega,t) = \varepsilon_0[\chi^{(1)} + \frac{3}{4}\chi^{(3)}|\vec{E}(t)|^2]\vec{E}(t)$. The third order nonlinear polarization leads to an intensity dependent susceptibility and refractive index, which is called the optical Kerr effect. We can consider the effective susceptibility as $\chi_{\mathrm{eff}} = \chi^{(1)} + \frac{3}{4}\chi^{(3)}|\vec{E}(t)|^2$ and the effective refractive index as: $n = \sqrt{1+\chi_{\mathrm{eff}}}$. This can be approximated as $n = n_0 + n_2 I(t)$, where $\mathrm{n_0}$ is the refractive index for zero light intensity, $\mathrm{n_2}$=$\dfrac{4\pi^2}{n_0^2}\chi^{(3)}(\omega;\omega,\omega,-\omega)$ is the non-linear refractive index at the frequency ω, $\chi^{(3)}(\omega;\omega,\omega,-\omega)$ is the third-order non-linear susceptibility, $I(t)$ is the (laser) light intensity. For typical Kerr media like sapphire, diamond or CaF_2: $\mathrm{n_0}$∼1, $\mathrm{n_2}$∼10^{-16}-10^{-14} $\frac{cm^2}{W}$. The additional refractive index proportional to the time-dependent light intensity leads to a phenomenon called self phase modulation (SPM). The non-linear phase change for a path L in the Kerr medium is $\Delta\Phi(t) = \frac{\omega}{c}n_2 I(t)L$. The time dependence of the phase change for an intensity that varies in time, such as that of a laser pulse, leads to the appearance of a frequency deviation $\Delta\omega(t) = \frac{\omega}{c}n_2 L\dfrac{\partial I}{\partial t}$. This introduction of additional frequencies above and below the center frequency ω leads to a spectral broadening of a laser pulse by $\Delta\omega \approx \frac{\omega}{c}n_2 L\dfrac{I_0}{\tau}$, with I_0 being the peak intensity and τ the pulse duration. In the above description of the SPM mechanism we take into account only first order dispersion. Under such assumption, only symmetric spectral broadening occurs. However, there are additional mechanisms that lead to asymmetric broadening, such as self-steepening, spatial self-interaction of the pulse, and non-instantaneous medium response [42]. The spatial self-interaction is induced by the Kerr nonlinearity of the medium. The radial non-homogeneity of the laser intensity creates a radial variation of the refractive index via $n = n_0 + n_2 I(r)$, which can be seen as a lens. This so-called Kerr lens leads to beam self-focusing for $\mathrm{n_2}$>0 or self-defocusing for $\mathrm{n_2}$<0. As a result of self-focusing the laser fluence and hence the strength of optical non-linear processes increases. Self-focussing

leads to complex changes in phase and intensity of the pulse. As a result, several filaments form, each of them are form a source of broadband radiation. Self-steepening changes the temporal shape of the beam due to the intensity dependence of the group velocity. In a medium with $n_2>0$, the peak of a pulse propagates slower than its wings, which makes the trailing edge of the pulse steeper and the leading edge less steep. In summary, spectral broadening of a laser pulse occurs when a high-intensity beam propagates through a Kerr medium. In the first stage the beam is self-focused and its diameter decreases, increasing the fluence. The increased fluence creates an electron plasma in the medium, which in turn defocuses the beam. When the plasma defocusing compensates the self-focussing, spectral broadening occurs [42], [43]. A typical example of the white light spectrum generated by SPM in sapphire is depicted in Fig. 2.3.

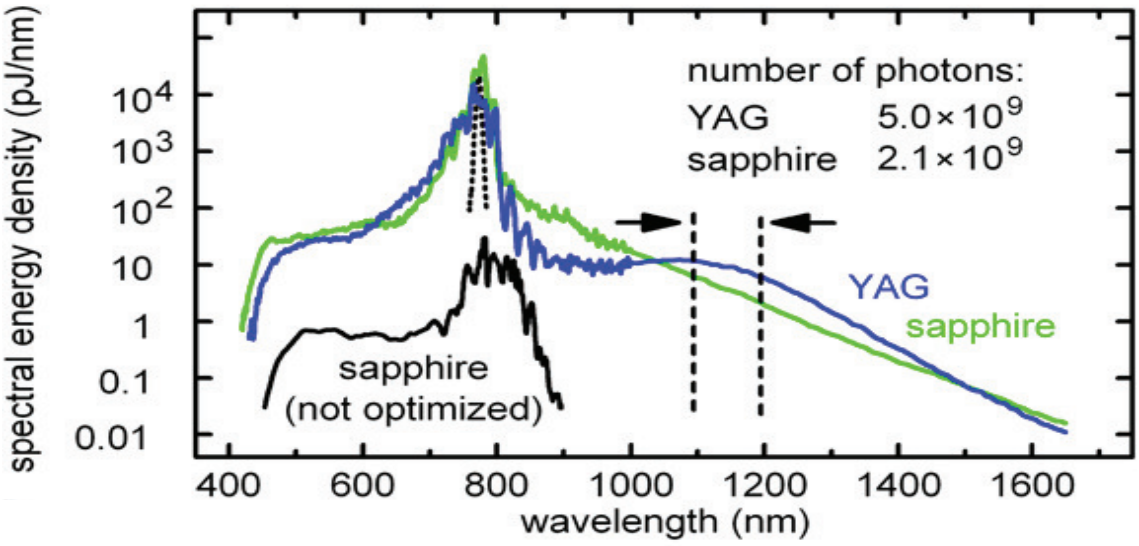


Figure 2.3: Examples of the white-light spectrum in the sapphire and YAG crystals. In the range which is marked with arrows the number of photons is significantly higher than the one generated from the sapphire continuum. Image taken from Ref. [44].

2.3 Pump-probe spectroscopy

The basic idea of time-resolved (pump-probe) spectroscopy is to trace the evolution of a system from equilibrium to a non-equilibrium situation and back with femtosecond ($\sim 10^{-15}s$) resolution. Such time resolution enables to investigate important relaxation processes that determine the functional properties of solids. In pump-probe spectroscopy two beams of ultrashort laser pulses are used. The first pulse excites the system out of equilibrium, the second, weaker pulse takes a snapshot of the system at a defined point in time after the excitation. Scanning the delay between the pump and probe pulses – typically with a mechanical delay stage that controls the optical path of one of the beams – traces the relaxation of the system back to equilibrium. The pump and probe pulses can have different nature: they can be both in or near the visible part of the spectrum, but the probe can also be in the THz range or even be an electron pulse to study structural dynamics via time-resolved electron diffraction. Detection of the probe light is in transmission or reflection geometry depending on the transmittance of the sample. The

pump-probe experiments in this thesis used pump and probe pulses in the visible range in transmission geometry.

2.3.1 Possible type of signals in Pump-probe measurements

The transient absorption with the pump beam turned on is $\mathrm{A}(\lambda)+\Delta\mathrm{A}(\lambda,t)$, with $\mathrm{A}(\lambda)$ being the absorption with the pump off and $\Delta\mathrm{A}(\lambda,t)$ the change in absorption due to photoexcitation. $\Delta\mathrm{A}(\lambda,t)$ can be positive or negative in different wavelength regions; a negative $\Delta\mathrm{A}(\lambda,t)$ corresponds to photobleaching or stimulated emission, a positive $\Delta\mathrm{A}(\lambda,t)$ corresponds to new absorption bands (photoinduced absorption). The pump-probe experiments in this thesis are performed in transmission. Assuming that the changes in transmission originate predominantly from changes in absorption (i.e. neglecting changes in the reflection and scattering contributions), we can relate $\Delta\mathrm{A}(\lambda,t)$ to the relative change in transmission $\frac{\Delta\mathrm{T}}{\mathrm{T}} = \frac{\mathrm{T}_{\text{pump on}}-\mathrm{T}_{\text{pump off}}}{\mathrm{T}_{\text{pump off}}}$: $\Delta\mathrm{A}(\lambda,t) = -\frac{1}{\ln 10}\frac{\Delta\mathrm{T}}{\mathrm{T}}(\lambda,t)$. Using Bouguer-Lambert-Beer law the change in the absorption can be re-writed as: $\mathrm{T} = \mathrm{I}_0\exp(-kd)$, where I_0 is incident light, T is transmitted light. The pump-probe signal can be represent as: $\frac{\Delta\mathrm{T}}{\mathrm{T}} = \frac{\exp(-k_{\text{on}}d)-\exp(-k_{\text{off}}d)}{\exp(-k_{\text{off}}d)} = \frac{\exp(-k_{\text{on}}d)}{\exp(-k_{\text{off}}d)} - 1$, where $k_{\text{on}}, k_{\text{off}}$ is absorption coefficient with and without pump beam respectively; d is sample thickness. Then $\frac{\Delta\mathrm{T}}{\mathrm{T}} = \exp(-(k_{\text{on}}-k_{\text{off}})d)-1$, since change in the absorption coefficient with pump and without is small, we can expand $\frac{\Delta\mathrm{T}}{\mathrm{T}}$ in the Taylor series: $\frac{\Delta\mathrm{T}}{\mathrm{T}} \approx 1-(k_{\text{on}}-k_{\text{off}})d-1 = -(k_{\text{on}}-k_{\text{off}})d = -\Delta kd$. The absorption coefficient k is proportional to the density of the different kind species which absorb the light times their absorption cross-section: $k = \sum_i N_{\mathrm{i}}\sigma_{\mathrm{i}}$, where N_{i} – populations of photoexcited species in $[\frac{1}{cm^3}]$, σ_{i} – absorption cross section of each populations, $[cm^2]$. In general the population of photoexcited species depends on time $N_{\mathrm{i}}(t)$ and the absorption cross-section depends on frequency $\sigma_{\mathrm{i}}(\omega)$. Than $\frac{\Delta\mathrm{T}}{\mathrm{T}} = -d\sum_i N_{\mathrm{i}}(t)\sigma_{\mathrm{i}}(\omega)$, so the evolution of $\frac{\Delta\mathrm{T}}{\mathrm{T}}$ is the evolution of the photoexcited populations.

2.3.2 Pump-probe setup

Here I will describe the pump-probe setup that was used for the measurements reported in this thesis. We excited the samples under investigation at different pump energies and used a broad-band probe to detect the relaxation dynamics at different energies. The laser source is a regeneratively amplified mode-locked Ti:Sapphire laser (Coherent Libra) operating at 1 kHz repetition rate with 1.55 eV energy, giving pulse with 100 fs duration and 4 mJ energy. A fraction of the pulse energy is focused in a 3 mm thick sapphire plate to generate a single-filament white light continuum spanning the range $\sim$ 1.65-3.1 eV, used as a probe. Another fraction of the pulse energy is used to generate the pump pulse, either by second harmonic generation in a BBO crystal, or in a second-harmonic pumped optical parametric amplifier (OPA), generating $\sim$ 70 fs pulses tunable from 1.65 to 2.5 eV. The signal beam for the OPA is generated in sapphire and is selectively amplified by the pump pulse at 3.1 eV generated in a BBO crystal. The non-collinear geometry allows phase-matching of the pump and seed pulses over a broad spectral range. The spectral portion of the white light that is amplified is selected through a delay line that allows to adjust the temporal overlap of the pump and seed pulses.

The pump and probe beams are focused and spatially overlapped on the sample. The energy of the probe is kept weak to prevent re-excitation of the sample. The spot size

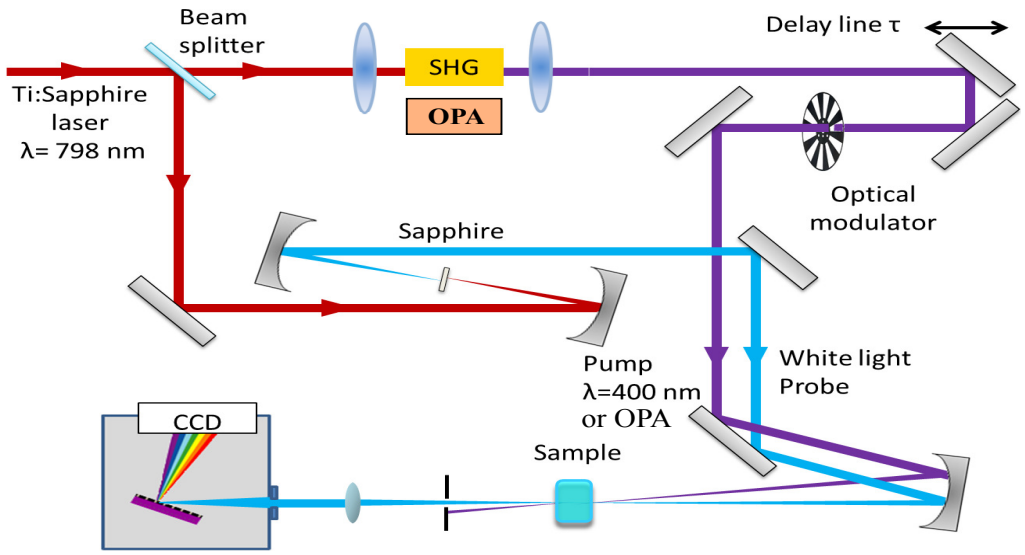


Figure 2.4: The sketch of pump-probe setup used in the thesis

of the pump beam is larger than that of the probe in order to probe only the photoexcited part of the sample. The delay between the two pulses is controlled by a delay line mounted on a computer-controlled translation stage, which allows to vary the optical path length of the pump beam. In order to acquire the transmitted probe spectrum with and without photoexcitation, a chopper modulates the pump pulses at half the pulse repetition frequency (500 Hz in our case), blocking the first of two consecutive pulses. A customized software calculates $\frac{\Delta T}{T} = \frac{T_{\text{pump on}} - T_{\text{pump off}}}{T_{\text{pump off}}}$ for two consecutive probe pulses and averages over hundreds of pulses for each selected pump-probe delay. The spectrometer consists of a grating and a CCD array and allows a signal-to-noise ratio of 10^{-5}. A sketch of the pump-probe set-up is depicted in Fig. 2.4.

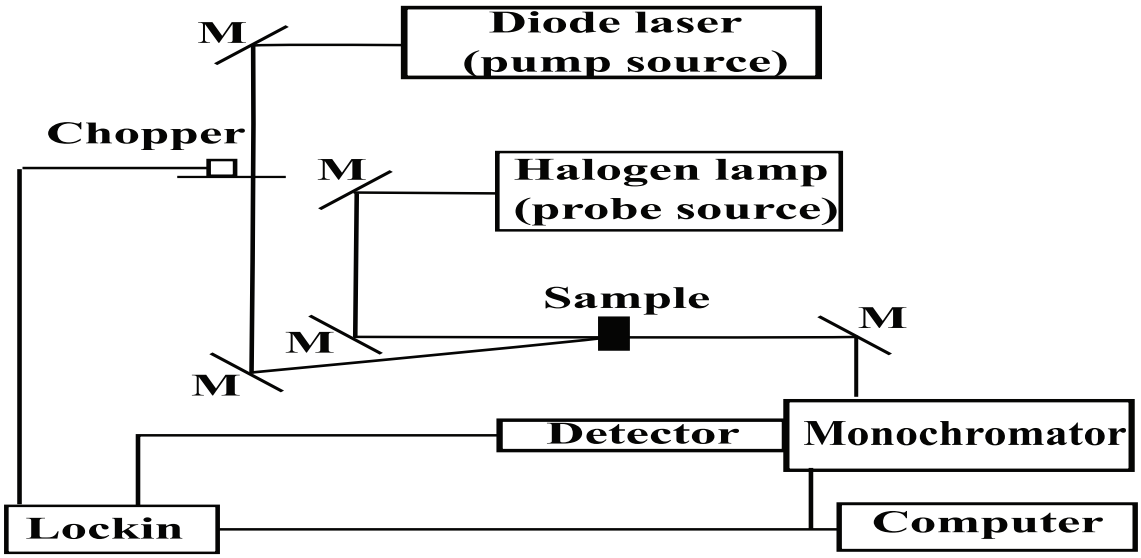


Figure 2.5: A sketch of the photoinduced steady-state absorption setup used in the experiment.

2.4 Photo-induced absorption spectroscopy

The basic principles of photo-induced absorption spectroscopy (PIA) are identical to those of pump-probe spectroscopy, just that PIA lacks the direct time resolution. The PIA set-up is sketched in Fig. 2.5. Usually a continuous wave (cw) laser is used for the pump and a halogen lamp for the broad-band probe beam. The detected wavelength is scanned by a computer-controlled monochromator. Since the excitation densities achievable by CW excitation are usually much lower than with pulsed lasers, $\frac{\Delta \mathrm{T}}{\mathrm{T}}$ is usually low, of the order of $10^{-5} - 10^{-4}$. Hence we use a lock-in detection scheme where the pump is modulated by a chopper, which also provides the reference signal for the lock-in amplifier. The lock-in amplifier multiplies the ΔI and the reference signal and removes the oscillatory components of the result via a low-pass filter. Let us consider only the fundamental frequency of the signal $S(t)$ and reference $R(t)$:

$$R(t) = R_0 \cos \omega t, \tag{2.5a}$$

$$S(t) = S_0 \cos(\omega t + \varphi), \tag{2.5b}$$

$$R(t)S(t) = \frac{1}{2} R_0 S_0 [\cos \varphi + \cos(2\omega t + \varphi)], \tag{2.5c}$$

The low-pass filter will remove the 2ω component and the resulting signal will be DC and proportional to $S_0 \cos \varphi$. Most lock-in amplifiers have a second output channel that yields a signal proportional to $S_0 \sin \varphi$. The *cos* term is called the in-phase and the *sin* term is called the quadrature component of the signal. S_0 and φ depend on the chopper period $T = \frac{2\pi}{\omega}$ and the lifetime τ of the photoexcited species that gives the signal. For slow modulation $\tau < T_m$ the transient photoexcited population and hence $S(t)$ follow the almost square wave modulation of the pump by the chopper (Fig. 2.6, first curve). $S(t)$ is in phase with $R(t)$

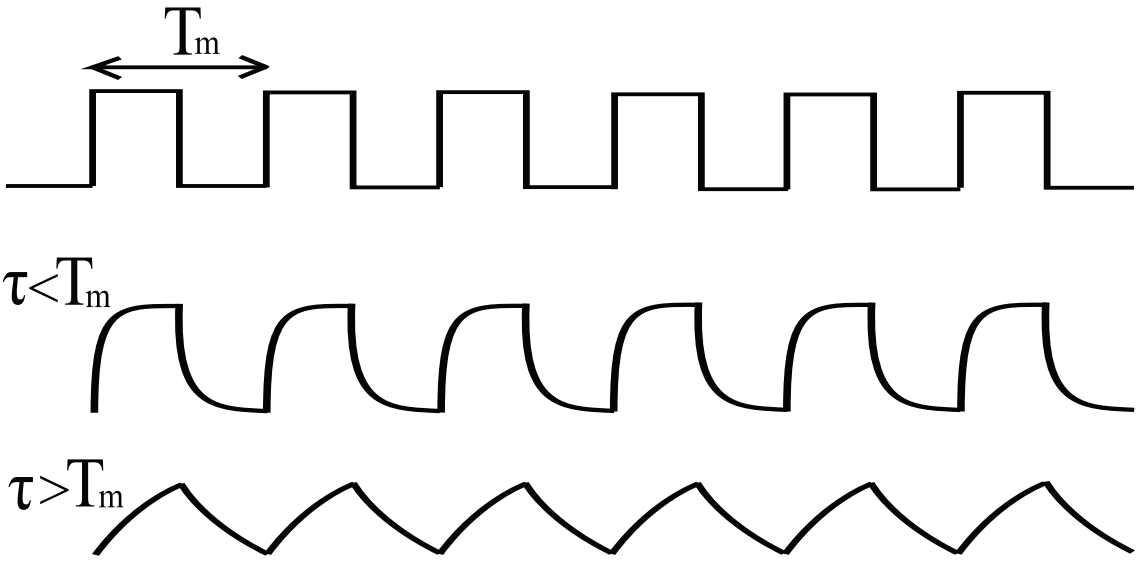


Figure 2.6: The pulse train from CW laser modulated by chopper (upper row), the signal from the system under investigation when the population relaxation time is shorter than modulation period (middle row) and when the population relaxation time is longer than modulation period (lower row).

and the photoexcited population oscillates between zero and the equilibrium population when the generation rate equal the decay rate (Fig. 2.6, second curve). For fast modulation

$\tau > T_m$ the transient population reaches neither zero nor the upper equilibrium, but follows an almost triangular wave, with $\varphi \sim 90°$ and a lower amplitude which decreases with increasing ω (Fig. 2.6, third curve). Hence, a frequency dependent measurement of the in-phase and quadrature components can be used to estimate the lifetime of the photoexcited species.

2.5 Samples' preparation

The samples studied in this thesis (Chapter 3 and Chapter 4) are MoS_2 flakes obtained from liquid exfoliation dispersed in transparent, inert PMMA matrix, as shown in the inset of Fig. 2.9. 1 mg of MoS_2 in water/ethanol mixture (Graphene Supermarket) was extracted by flocculation with the addition of KCl (potassium chloride $\geq$ 99.0%, Sigma) into a solution. The obtained flocculates were repeatedly washed with a fresh water/ethanol (1:1) mixture to remove any salt residues. The solvent mixture was then replaced by absolute ethanol only. Sedimented MoS_2 was extracted from the bottom with a minimum amount of solvent and redispersed in 2 mL of chlorobenzene in an ultrasonic bath. 40 mg of PMMA (poly(methyl)methacrylate, Sigma Aldrich) was added to a dispersion of MoS_2 and sonicated at 50 °C for 30 min. 30 μL of the obtained stable solution was drop-cast onto a quartz substrate and left to dry in air.

The samples studied in Chapter 5 are electric double-layer field-effect transistors (EDLT) with ionic liquid. The channels in the transistors are monolayer WSe_2. The substrate is made of Si/SiO_2 where, sequentially, 100 nm of Al (acting as a reflective surface) and 30 nm of HfO_2 (in contact with the flakes) have been deposited. The gate, source and drain electrodes are made of Pd/Au (5/50 nm thickness).

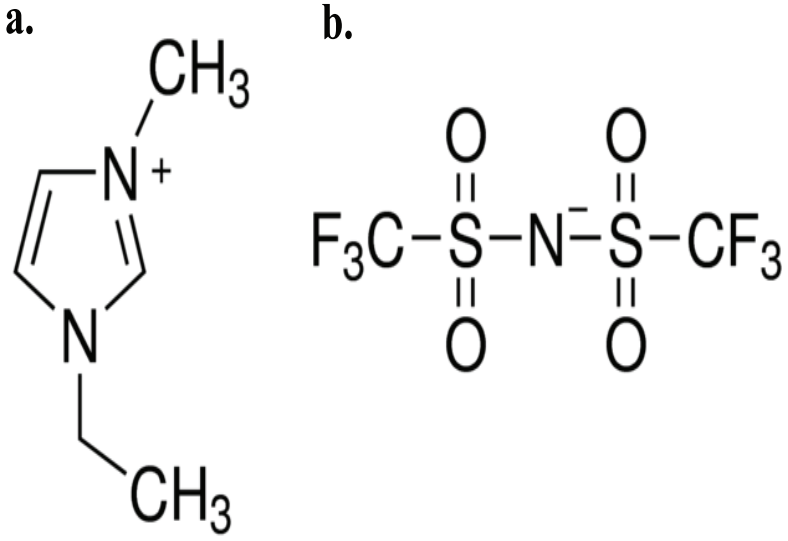


Figure 2.7: The components of ionic liquid: a. 1-ethyl-3-methylimidazolium (EMIM) cation; b. bis(trifluoromethylsulfonyl)imide (TFSI) anion.

Monolayers of WSe_2 were mechanically exfoliated onto a degenerately doped n^{++} Si chip covered by 270 nm SiO_2 and identified by optical contrast [45]. Since the SiO_2 substrate has high density of charge impurities and leads to an increased doping at the dielectric — 2D material interface [46], as-exfoliated WSe_2 was transferred from the Si/SiO_2 to the target substrate ($Si\text{-}SiO_2/Al/HfO_2$) using a wet transfer method based on a glass

slide covered with Polydimethylsiloxane (PDMS) as a stamp, a poly(L-lactic acid) polymer film (PLLA) as the holder for the flakes and deionized water promoting the detachment of the polymer [47]. The process was completed by electron beam lithography and deposition of the metal electrodes. A polymer electrolyte based on a mixture of PS-PMMA-PS (polystyrene-PMMA-polystyrene) and [EMIM]-[TFSI] (see Fig. 2.7) ion [48] was spin-coated onto the device by using 6000 rpm for 2 minutes as spin-parameters.

2.5.1 Characterization of the samples by Steady-State Absorption and Raman scattering

Raman spectra of layered materials are sensitive to the number of layers in a sample. MoS_2 shows two Raman modes A_{1g} and E^1_{2g} close to 400 cm^{-1}. Interlayer interaction increases the frequency of the out-of-plane A_{1g} mode, while the in-plane E^1_{2g} mode shows an anomalous softening with increasing layer number [15]. Due to this shift in opposite directions, the distance between the two modes gives a measure of the layer number. Raman characterization was performed with an NT-MDT NTEGRA SPECTRA confocal Raman microscope in backscattering geometry with spectral resolution of $\backsim$0.6 cm^{-1}. We used excitation lines at 488 nm (Argon ion laser) and 632.8 nm (He–Ne laser) and a 100× objective (NA 0.9) to focus onto a spot size of 3 μm. The Raman signal was detected with a cooled CCD array. We used a laser power below 3 mW to avoid damaging the sample.

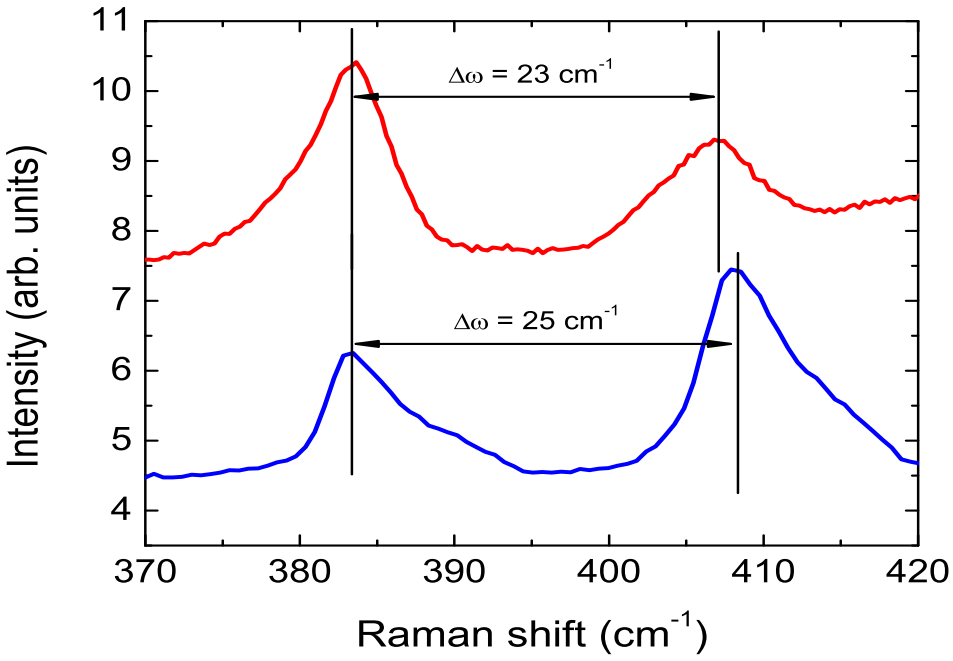


Figure 2.8: Raman spectra of MoS_2 at two excitation wavelengths at 633 nm (red line) and 488 nm (blue line)

From the Raman spectra of our sample shown in Fig. 2.8 for varying excitation wavelength a different distance between two modes was found. It can be explained that different laser wavelength excites areas on the sample with different thicknesses. For the excitation at 633 nm we got $\triangle\ w$=23 cm^{-1} and $\triangle\ w$=25 cm^{-1} at 488 nm. The Raman spectra indicate

a flake thickness distribution that is dominated by three- to six-layer flakes.

The steady-state absorption spectrum has the characteristic step-like shape with four peaks (Fig. 2.9) labeled A to D at 1.9, 2.1, 2.7 and 2.9 eV. Our sample is doped due to dislocations induced by exfoliation and due to impurities. Absorption peaks A(B) have contribution of A(B) exciton and $A^-(B^-)$ trion, the trion peak is $\backsim$30 meV red-shifted compare to the exciton. Experimentally, no trions were observed for B exciton. For the A peak, an even lower energy contribution has been identified,[49] which has alternatively been ascribed to a surface-trapped exciton,[50] an edge state,[51] or a plasmon resonance,[52] so that peak A actually arises from the overlap of three peaks. Similar to the notation in refs. [28], [49], [53], we will use the labels L, A^-, and A^0 for the low energy peak, charge peak, and exciton peak of the A resonance, and B^- and B^0 for the charged and neutral contributions to the B resonance.

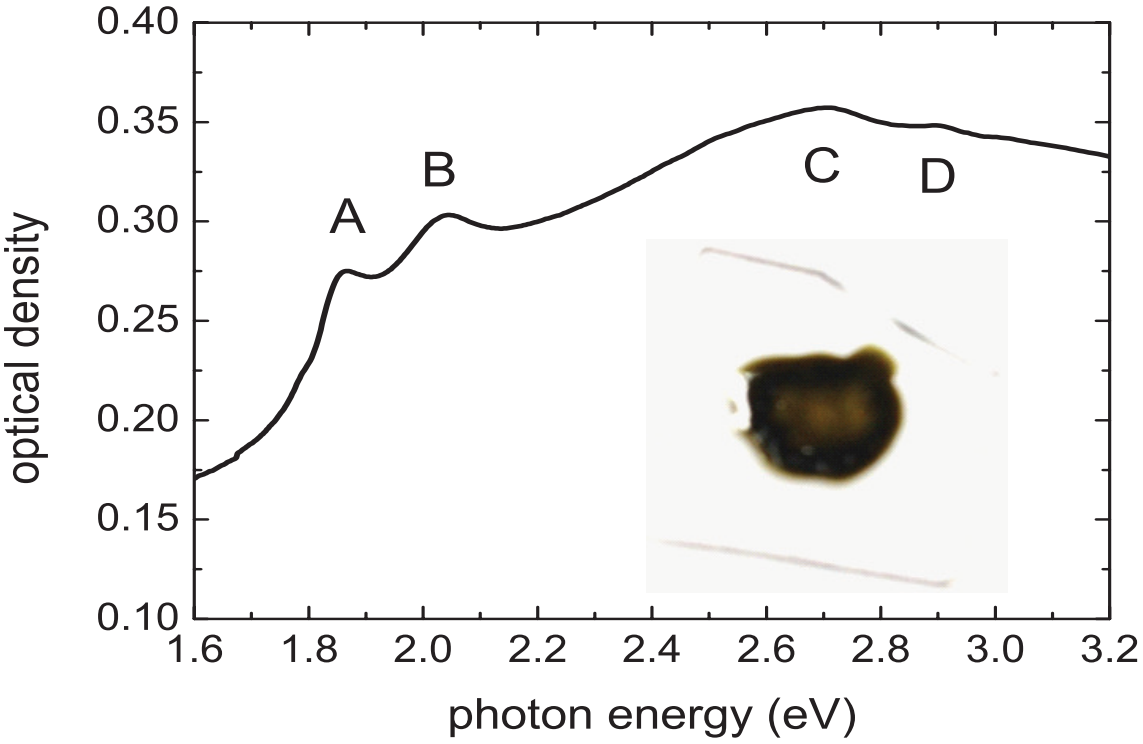


Figure 2.9: Absorption spectrum of the sample of MoS_2 in PMMA. Inset shows a photograph (the dark area has a diameter of approximately 7-8 mm)

Raman measurements for the Chapter 5 were done on the same Raman set-up as for the Chapter 3 and Chapter 4, just electrical and optical measurements were performed in high vacuum (10^{-6} mbar) and after an in situ thermal annealing at 343 K for 16 hours.

Chapter 3

Charge photogeneration in few-layer MoS_2

The two-dimensional semiconductor MoS_2 in its mono- and few-layer form is expected to have a significant exciton binding energy of several 100 meV, suggesting excitons as the primary photoexcited species. Nevertheless, even single layers show a strong photovoltaic effect and work as the active material in high sensitivity photodetectors, thus indicating efficient charge carrier photogeneration (CPG). Here we use modulation spectroscopy in the sub-ps and ms time scales to study the photoexcitation dynamics in few-layer MoS_2. Our results suggest that the primary photoexcitations are excitons which efficiently dissociate into charges with a characteristic time of 700 fs. Based on these findings, we make simple suggestions for the design of efficient MoS_2 photovoltaic and photodetector devices.

3.1 Continuous wave photomodulation spectroscopy data on MoS_2

To identify long lived photoexcitations we performed CW PM spectroscopy. Those photoexcitations whose population changes significantly over the modulation cycle (i.e. their lifetime is long enough to build up sufficient population while the laser is on and short enough to sufficiently reduce their population while it is off) are identified in the CW PM spectrum via their photoinduced absorption (negative $\triangle T/T$) transitions to higher excited states. Concomitantly with the increase of photoexcited populations, the ground state population and its associated absorption is reduced (photobleaching, positive $\triangle T/T$). The CW PM spectrum at room temperature upon excitation at 3.1 eV, above the C and D exciton resonances, is shown in (Fig. 3.1a). The signal is largely in phase with the modulation of the photoexcitation, with a negligible quadrature contribution. This means that the populations at the origin of the signal can easily follow the modulation at 245 Hz, implying that the lifetimes of the respective photogenerated species are much shorter than the modulation period of $\sim$4 ms. The main features of the spectrum are three positive (photobleaching) and two negative (photoinduced absorption) peaks. We fit the spectrum using five overlapping Gaussians (see Fig. 3.1b), which represent the thermal and disorder-induced (in particular by polydispersity of flake thickness) broadening of the electronic resonances. The strong overlap between neighboring peaks makes them appear narrower than their actual lineshape and connected by an almost straight line, masking the inflection points characteristic of isolated Gaussian peaks. The spectral positions of the five peaks correspond very well with the three neutral and two charge peaks discussed in [28], [49], [53]. Assuming the same origin for the peaks in the PM spectrum, we obtain a straightfor-

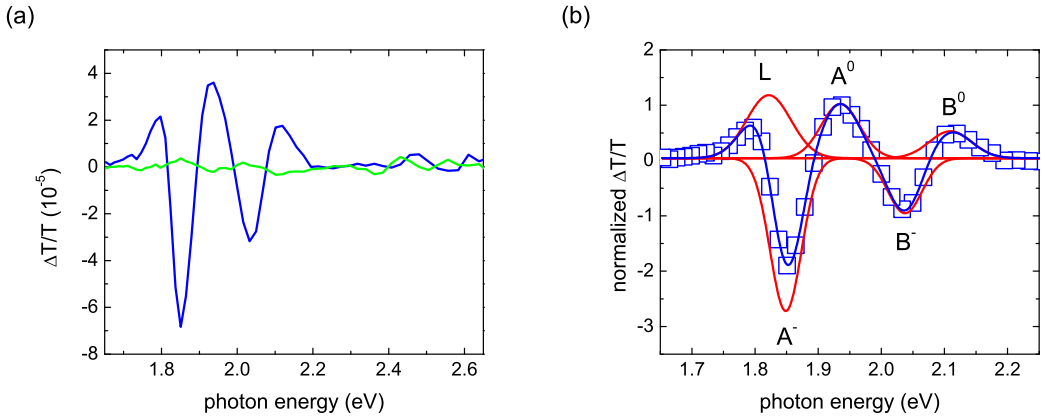


Figure 3.1: (a) CW photoinduced absorption spectrum of MoS_2 in PMMA at room temperature for excitation at 3.1 eV. In-phase (blue) and quadrature (green) signal components are shown for a modulation frequency of 245 Hz. (b) Five Gaussian fits (red) whose sum (blue) fits the normalized in-phase spectrum (open squares).

ward interpretation. Upon photoexcitation, the number of electrons in the neutral ground state is reduced, and the number of charge carriers is increased. Hence the absorption features L, A^0, and B^0 from transitions between neutral states are reduced, resulting in a positive $\triangle T/T$ (photobleaching), while the absorption features A^- and B^- from charges are increased, yielding a negative $\triangle T/T$ (photoinduced absorption).

Alternatively, one could interpret the PM spectrum based on its resemblance of a derivative lineshape. A photoinduced blue shift of the absorption spectrum would result in a $\triangle T/T$ contribution that follows the first derivative of the absorption spectrum (or a negative first derivative for a red shift); a photoinduced broadening of the absorption peaks would contribute a negative second derivative. If we interpreted our spectrum in terms of derivative lineshapes, it would be dominated by a positive second derivative, which indicates a photoinduced line narrowing. We are not aware of any such mechanism. However, the A peak is composed of the three overlapping narrower peaks L, A^-, and A^0 (no equivalent to the L peak has yet been identified for the B peak, but we may extrapolate our reasoning also to B). In our proposed scenario photoexcitation generates charges and the middle peak A^- increases at the expense of the other two, which decreases the overall width of the A peak. Hence, CPG leads to an apparent photoinduced line narrowing, which explains the positive second derivative lineshape.

3.2 Ultrafast data on MoS_2

To investigate CPG in real time, we employed femtosecond optical pump-probe spectroscopy. We start by comparing the $\triangle T/T$ signal for excitation at 3.1 eV at long pump-probe delay (300 ps) with the CW PM (see Fig. 3.2a). The two normalized spectra are very similar, with three important differences: in the transient spectrum the L peak is absent, there is an additional broad photoinduced absorption feature peaking around 2.45 eV, and the whole spectrum is red shifted. This red shift is more pronounced at higher pump intensities (see Fig. 3.2b) and shorter pump-probe delays (see Fig. 3.3b and Fig. 3.3a). Both these correlations suggest that the red shift is stronger for higher concentration of a certain

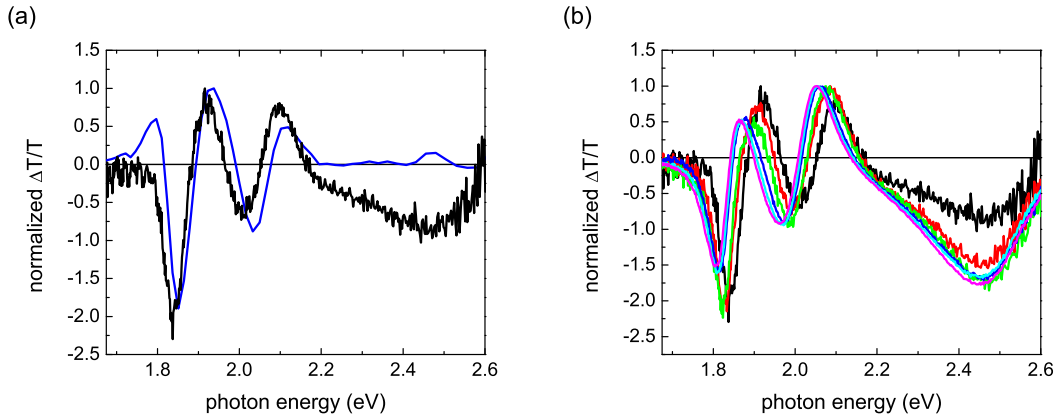


Figure 3.2: (a) Normalized CW photomodulation spectrum of MoS_2 in PMMA (blue) compared to the fs transient spectrum at 300 ps pump-probe (black) delay for $2*10^{14}$ cm^{-2} excitation fluence, 3.1 eV pump photon energy. (b) Pump-probe spectra at 300 ps normalized to the B exciton peak for different pump fluences at 3.1 eV pump photon energy: $2*10^{14}$ (black), $3*10^{14}$(red), $6*10^{14}$ (green), $20*10^{14}$ (blue), $40*10^{14}$ (cyan) and $80*10^{14}$ cm^{-2} (magenta).

species of excited states. The most intuitive interpretations are Stark effect due to the local field of photogenerated charges, as has been observed in semiconductor nanocrystals [54], organic semiconductors [55], and carbon nanotubes [56], [57], inter-excitonic interaction [58] or band gap renormalization, as has been found in semiconducting quantum wells upon photoexcitation [59] and inferred in recent works on semiconducting TMDs [60], [61]. After approximately 3 ps, the spectrum decays without any significant shifts or changes of shape, through a dominant process with a time constant of approximately 500 ps (see Fig. 3.3c), as previously obtained on few-layer MoS_2 supported on a dielectric substrate [30]. In addition to the previously identified A^-, A^0, B^-, and B^0 peaks, we note an additional broad absorption peak and a further positive peak at higher probe energies. Due to its position, we straightforwardly assign the positive peak to bleaching of the C exciton and label it C^0. The absorption peak (near C^0 exciton) shows a formation similar to A^- and B^-, and is similarly long lived; hence, it should belong to a charge population. Like the C exciton bleaching, it is absent in CW PM and strongly reduced for excitation energies below the C exciton resonance (see Fig. 3.3d); hence, we ascribe it to a charge associated with the C exciton, labeled C^-. The C exciton is ascribed either to excitation from a band below the valence band, or between the valence and conduction bands in a region of the bands nesting slightly off the Γ point [18]. In both scenarios, it is plausible that the C^0 and C^- features do not appear in the CW experiment, which probes populations that have relaxed toward the edges of the band gap.

3.3 Model of exciton dissociation to charge carriers in MoS_2

During the first 3 ps the $\Delta T/T$ spectrum undergoes a characteristic change of shape; the positive signal components are formed during the instrumental resolution and decay monotonically, while the main photoinduced absorption features, associated with charges A^-, B^-, and C^-, show an initial instrument-limited rise followed by a delayed rise component after the pump pulse and by a slower decay (see Fig. 3.3c, inset). The simplest scenario of

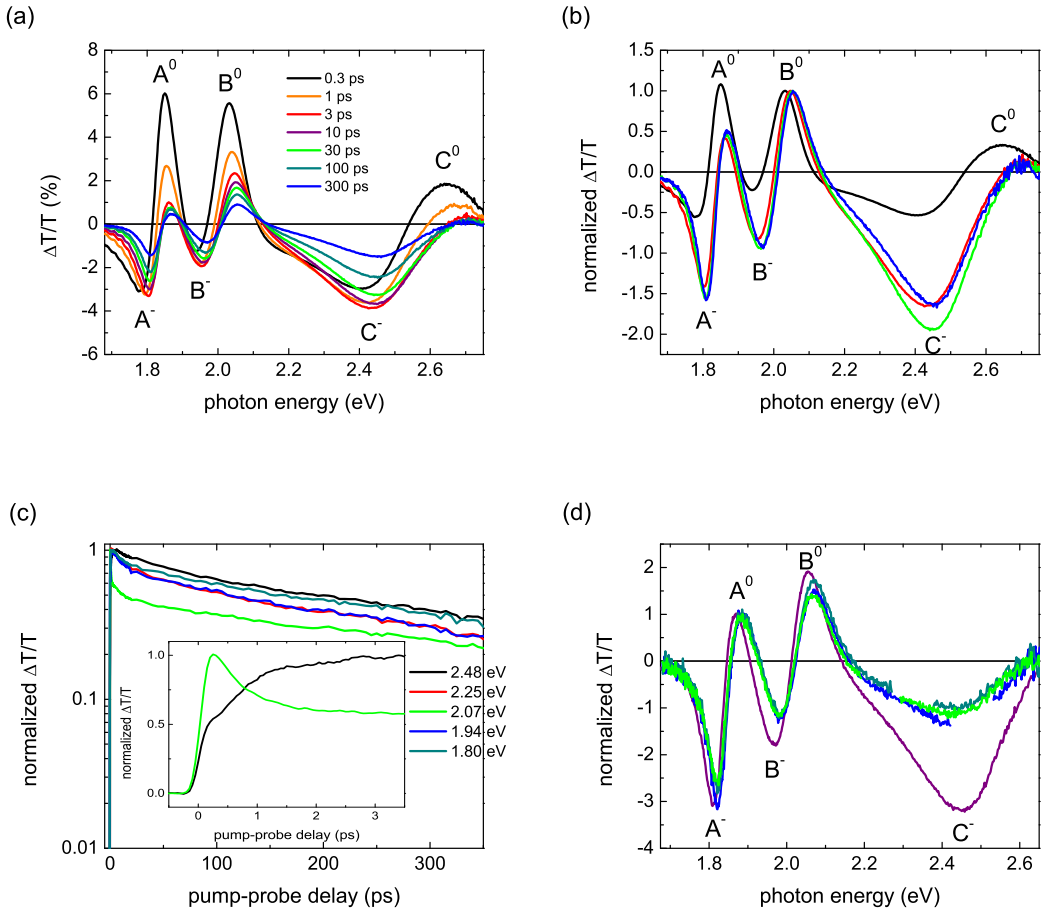


Figure 3.3: (a) Pump-probe spectra for $4{*}10^{15}$ cm^{-2} pump fluence at delays 300 fs (black), 1 ps (orange), 3 ps (red), 10 ps (purple), 30 ps (green), 100 ps (dark cyan), and 300 ps (blue). (b) Selected spectra from (a) normalized to the B^0 peak. (c) Normalized time traces for different probe energies: 2.48 (black), 2.25 (red), 2.07 (green), 1.94 (blue) and 1.80 eV (dark cyan). (d) Normalized spectra at 300 ps pump-probe delay for different pump photon energies: 3.10 (purple), 2.48 (blue), 2.34 (dark cyan) and 2.25 eV (green).

the underlying photoexcitation dynamics that is consistent with these results is sketched in Fig. 3.4a. The pump pulse generates excitons as the primary photoexcited species, and these excitons dissociate into pairs of charges with a characteristic time τ_1,

$$\frac{dE(t)}{dt} = G(t) - k_1 E(t), \tag{3.1a}$$

$$\frac{dC(t)}{dt} = k_1 E(t) - k_2 C(t), \tag{3.1b}$$

with $E(t)$ and $C(t)$ being the time-dependent overall exciton (A^0, B^0, and C^0) and charge (A^-, B^-, and C^-) populations and G(t) the exciton generation term (pump–probe cross-correlation, approximated as a Gaussian). $k_1 = 1/\tau_1$ is the rate constant of exciton dissociation and $k_2 = 1/\tau_2$ is the rate constant of charge recombination. The evolution of the photoexcited states' population according to Eq. (3.1a) and Eq. (3.1b) is best fitted with a characteristic times $\tau_1 = 700$ fs, $\tau_2 = 500$ ps. The assumption of only one common time

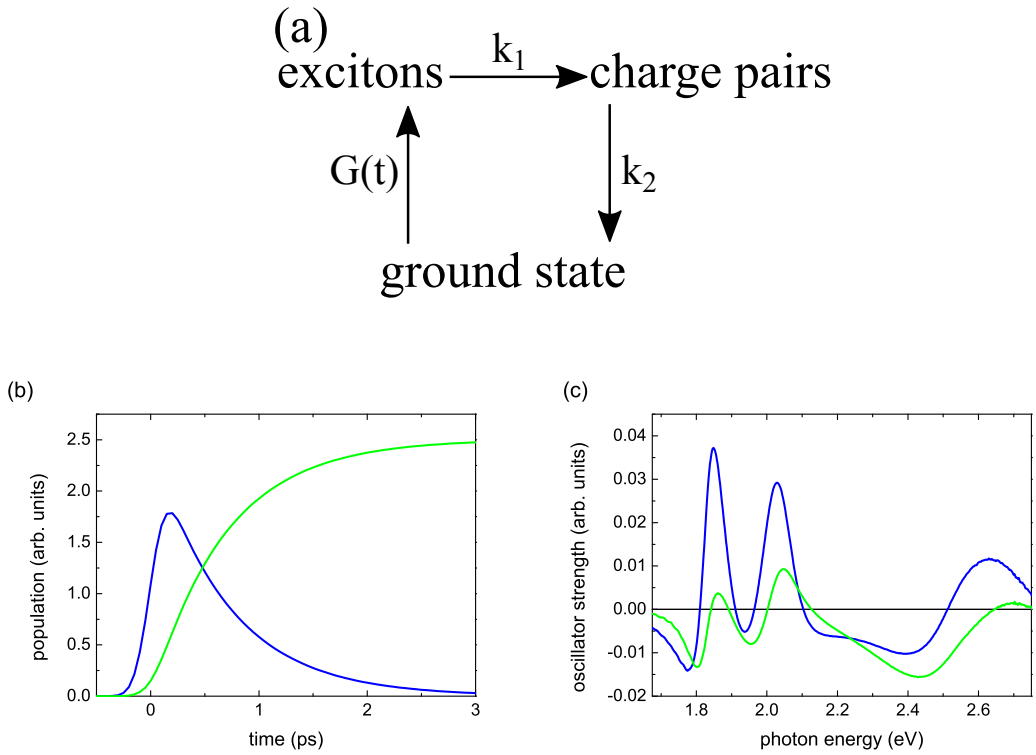


Figure 3.4: (a) Scheme of the photoexcitation dynamics of excitons and charges. (b) Time dependent exciton (blue) and charge (green) populations (c) Spectral contributions of excitons (blue) and charges (green).

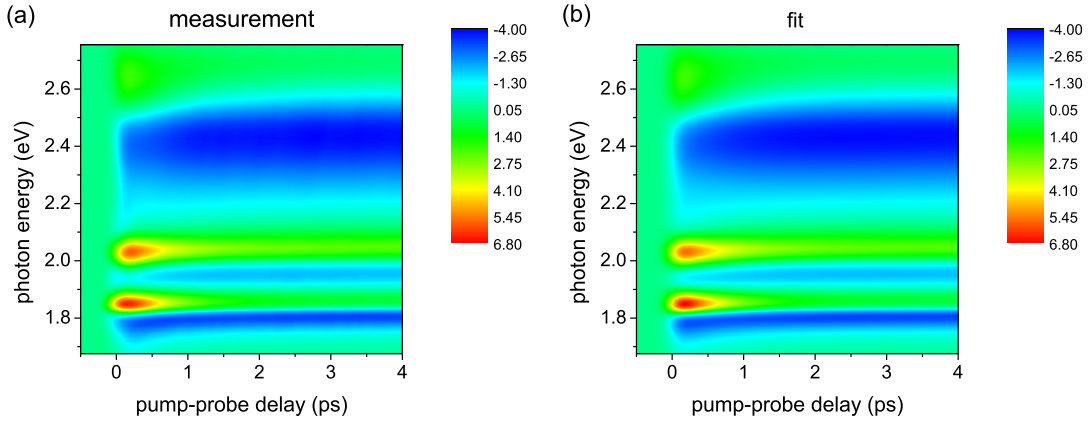


Figure 3.5: (a) Contour plot of the measured $\Delta T/T$ (in %). (b) Contour plot of the fitted $\Delta T/T$ (in %).

constant τ_1 for the dissociation of A, B, and C excitons may be a strong simplification, but it describes the data remarkably well (Fig. 3.5a, Fig. 3.5b).

The time-dependent exciton and charge populations and their contributions to the $\Delta T/T$ signal are shown in Fig. 3.4b, Fig. 3.4c, respectively. Please note that exciton

dissociation already occurs during the pump pulse; therefore, at all times the exciton population is lower than the number of absorbed photons and lower than the number of charge pairs that are eventually created. The spectral contributions, given as oscillator strength in arbitrary units, include both the photoinduced absorption features of excitons and charges (shown as negative oscillator strength in Fig. 3.4c) and their contribution to the bleaching (as positive oscillator strength). The bleaching contribution of charges is significantly smaller than that of excitons, suggesting that charges are more localized than excitons [62].

The exciton spectrum in Fig. 3.4c contains, in addition to the three well-known bleaching peaks, also several photoinduced absorption features. It is common in excitonic materials to observe such absorptions due to transitions from the lowest exciton level toward an exciton that involves an electron in a band higher than the conduction band (CB) or a hole below the valence band (VB) [63], [64]. The band structure of MoS_2 has many such bands [10], [65], and in particular at the K point, where the direct exciton is located, there are several band maxima and minima within the relevant range of 1–3 eV above the CB and below the VB, which can get involved in higher excitons A^* or B^*. While a precise identification of which bands are involved would require a detailed quantum chemical calculation of the transition matrix elements, which is beyond the scope of this thesis, we can generally assign the photoinduced absorption peaks of the exciton population to transitions A^0–A^* or B^0–B^*.

While for excitation at 3.1 eV our results suggest that all photoexcited excitons eventually dissociate with a characteristic time of 700 fs, Fig. 3.3d shows that the ratio between the absorption peaks due to charges and the respective bleaching peaks is slightly lower for lower excitation energy. This finding suggests that for lower pump photon energies, the charge yield can be somewhat lower than 100%. An analogous result has been published for an MoS_2 monolayer, where the lower photoluminescence quantum yield for higher excitation energy has also been ascribed to stronger exciton dissociation [18].

3.3.1 Branching ratio in direct generation of excitons and charges

Compared with our simplest scenario for the photoexcitation dynamics, two additional effects deserve consideration: direct excitation of charges and incomplete dissociation of the exciton population. Direct excitation of charge pairs (electron and hole) can be modeled by introducing a generation term in the equation for charges. Incomplete exciton dissociation should be accounted for by a time-dependent dissociation rate constant $k_1(t)$. However, a simpler way consists in arbitrarily dividing the excitons into two populations, one ($E_1(t)$) that dissociates according to Eq. (3.1a), and another ($E_2(t)$) that decays slowly with the same time constant τ_2 as the charges ($C(t)$) (to account for the fact that at long delays the spectrum does not change shape, which means that the ratio between excitons and charges should remain constant). Hence the system of rate dynamic equations becomes:

$$\frac{dE_1(t)}{dt} = \alpha(1-\beta)G(t) - k_1 E_1(t), \tag{3.2a}$$

$$\frac{dE_2(t)}{dt} = (1-\alpha)(1-\beta)G(t) - k_2 E_2(t), \tag{3.2b}$$

$$\frac{dC(t)}{dt} = \beta G(t) + k_1 E_1(t) - k_2 C(t), \tag{3.2c}$$

with α being the fraction of excitons that dissociate and β the fraction of directly photoexcited charges (relative to the total photoexcited population).

Unfortunately, neither the fraction of excitons that dissociate, nor the initial branching ratio between excitons and charges can be extracted from our data. Any assumption about

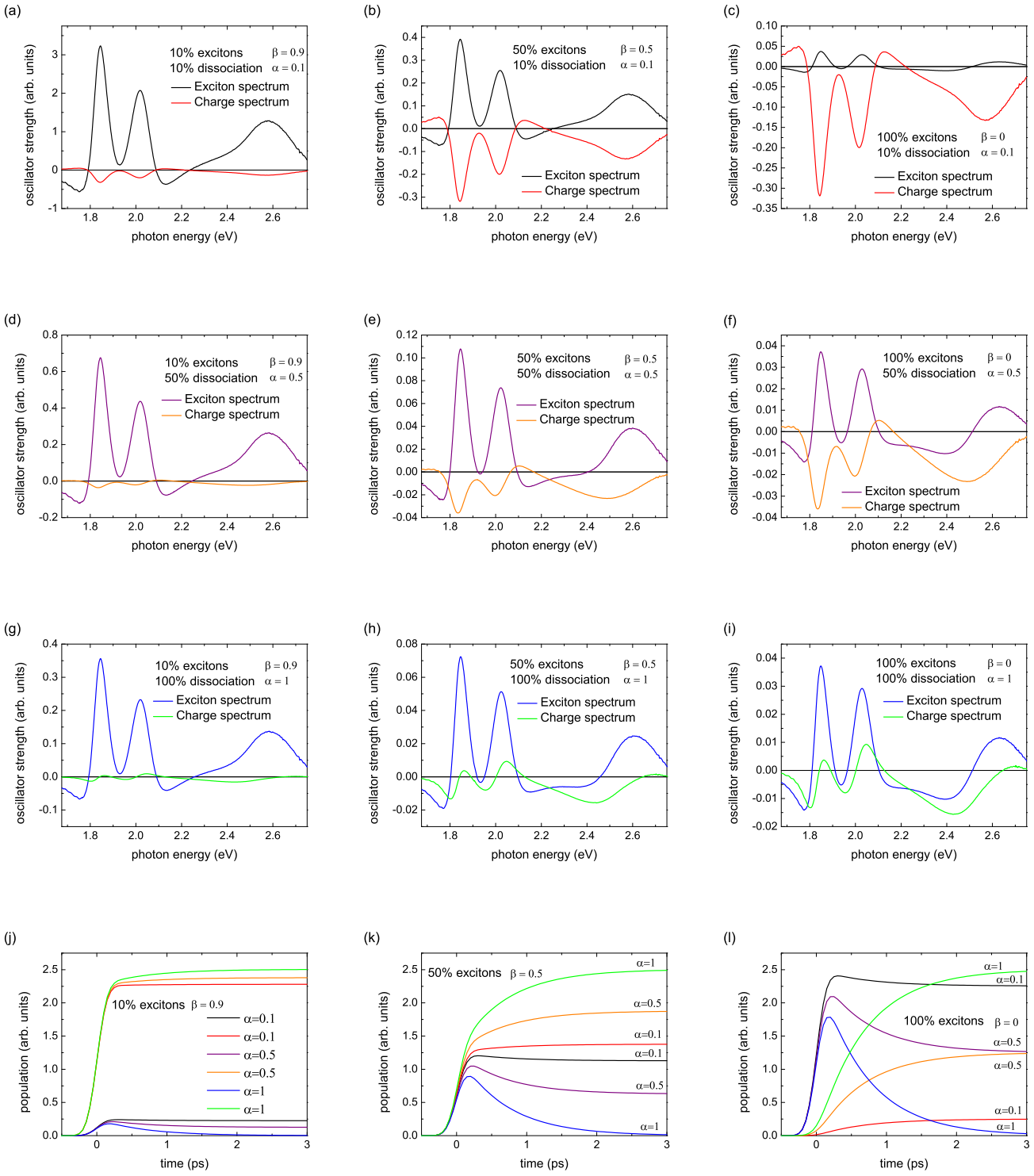


Figure 3.6: (a-i) calculated exciton (black, purple, blue) and charge (red, orange, green) spectra for different branching ratios and dissociation yields (see insert). (j-l) calculated exciton and charge populations for the branching ratios of the same column and different dissociation yields (same color code).

these two parameters gives different spectra for excitons and charges, all of which fit the experimental data equally well. However, the exciton and charge spectra obtained from the fit using Eq. (3.2) depend on both these parameters. In Fig.3.6a-i we show several examples, which illustrate three important trends. First, upon changing α, there is an important change in the resulting charge spectrum. For lower α the spectrum below 2.0 eV is more dominated by absorption; even at the bleaching peaks the overall signal is negative. Second, the higher β, the weaker the charge spectrum (the lower their oscillator strength). Finally, for increasing β, the kink in the exciton spectrum at 2.4 eV develops into an additional photoinduced absorption peak.

Based on these three observations, we can now evaluate which α and β values yield the most plausible spectra. It makes sense to assume that the charge spectrum should look similar to the CW PM spectrum (to a certain extent, since the charge density in the femtosecond measurement is much higher, which causes the above discussed red shift), which is also dominated by charges. The highest bleaching peaks and hence the strongest resemblance of the charge spectrum to the CW PM signal is obtained for α=1. (see Fig.3.6g, h, i). The assumption of complete exciton dissociation also leads to the simplest explanation why the relaxation behavior becomes wavelength independent after 3 ps: spectrum on the Fig. 3.6i (green) is due only to charges. Concerning the initial branching between photoexcitation of excitons and charges, even when we assume $\beta = 0$, the bleaching contribution of charges is significantly smaller than that of excitons (Fig.3.6c, f, i). This suggests that charges are more localized than excitons [64]. Since the exciton spectrum with a peak rather than a kink at 2.4 eV is more plausible, and materials with significant exciton binding energies usually have mostly excitons as their primary photoexcited species, we favor a scenario where the initial branching is largely biased towards excitons ($\beta = 0$ or very small).

The most plausible scenario – excitons as the primary photoexcitations which dissociate completely with a time constant of 700 fs yields the spectra shown in Fig.3.6i and the population dynamics depicted in Fig.3.6l (blue for the excitons and green for the charges).

3.4 Discussion

Let us now put our findings into context by comparing them to high-exciton binding energy materials on the one hand, and conventional semiconductors on the other hand. Detailed studies of the CPG dynamics exist for carbon nanotubes and conjugated polymers, whose exciton binding energies are similar to bilayer MoS_2, which is somewhat higher than in our samples. In carbon nanotubes, there is an initial branching between mostly excitons and 1%–2% directly excited charges [57], with a higher charge yield for higher excitation energy. In conjugated polymers, there is a similar initial branching, followed by additional CPG via dissociation of "hot" excitons during the first few picoseconds [66]. Elaborate models describe how the surplus energy of hot excitons increases their dissociation probability [67], [68]. The relaxation of the electron and hole to the lowest exciton state are typically faster than our observed 700 fs [69]–[71]; however, electron–phonon coupling creates a phonon heat bath that can live on for a few picoseconds [72]. In addition, exciton migration, which is facilitated by the excess energy and comes to a halt when the exciton reaches a local energy minimum, increases the probability that the exciton reaches a site where its dissociation is facilitated. In MoS_2 flakes, such sites could be surface defects, flake edges, metallic inclusions, crystal faults, or small islands of an extra MoS_2 layer. In the few-layer flakes of our study, for excitation at 3.1 eV, the exciton dissociation yield is close to 100% and only slightly lower for lower pump energies above the B exciton resonance. Hence, if hot exciton dissociation (phonon- or defect-mediated) mechanisms play a role, they are

masked by the already high dissociation yield observed just above the B exciton resonance.

In conventional bulk semiconductors, the exciton binding energy is typically so low that at room temperature free carriers are photoexcited directly, prevalently across the direct gap. In the case of indirect gap semiconductors, the photoexcited electrons and holes relax toward the CB minimum and VB maximum of the indirect gap on a time scale of 100–200 fs [69], [73]. This fast relaxation is the reason for the low fluorescence quantum yield of indirect semiconductors. In our case, the exciton binding energy is sufficient to have excitons as the primary photoexcited species, but is insufficient to prevent their subsequent dissociation. The relaxation toward the indirect gap is possible only if it is preceded or accompanied by exciton dissociation, which is the rate-limiting step in this case. An exciton lifetime of 700 fs is still much shorter than the 60 ps observed at room temperature for the monolayer [31] and can hence explain the much lower quantum yield of the excitonic fluorescence in the few-layer case [4]. For a bilayer of WSe_2 at 4 K the direct gap fluorescence bears a lifetime of 3 ps, while the indirect gap fluorescence has an onset that is delayed by a few picoseconds [74]. We can hence assume an analogous mechanism as we observe in the few-layer MoS_2 flakes, where exciton dissociation enables the carriers to scatter toward the indirect gap. Due to the higher exciton binding energy in the bilayer, the exciton dissociation and hence the scattering toward the indirect gap is slower than in our case.

Before we discuss the implications of efficient exciton dissociation, we review how our findings compare to previous femtosecond work on TMDs. Intervalley scattering [75], [76] requires circular polarization and is not probed in our experiment, because all our laser polarizations are linear. On a time scale of 1–500 ps, Shi et al. [30] obtained results very similar to ours in few-layer flakes deposited on a dielectric substrate, but they do not discuss the temporal change of shape of the spectrum, which is crucial to understanding exciton dissociation and charge generation. They estimate that for excitation fluences similar to ours, the sample temperature should change by only 0.1 K, thus dismissing sample heating as a possible source of the signal. In our samples, due to the low heat conductivity of PMMA [77], heating could be a bit stronger. However, a signal due to heating would not change its shape with time and, most crucially, at least for comparable absorbed fluences, its shape would not depend on the excitation photon energy. In Fig. 3.3d, there is a small C^- signal even for excitation below the C exciton resonance. This contribution, which at any delay is 20% or less compared with the spectrum for excitation above the C resonance, may originate from heating or any other mechanism that changes the overall lineshapes and/or peak positions, such as Stark effect or band gap renormalization. Hence, for the combination of all such processes including heating, we estimate an upper boundary of 20% contribution to the transient signal. Any such mechanism is less important in the CW PM experiment, where no appreciable C^- signal is found. Therefore, both the femtosecond and the CW signals are dominated by changes in excited and ground-state populations, not pure lineshape/shift mechanisms.

Considering further lineshape/shift mechanisms, inter-exciton interaction is expected to result in a red-shift [58] and line broadening. However, we observe an apparent line narrowing (see the discussion of the CW PM spectrum) due to the increase of the central A^- peak at the expense of its neighbors on either side. The Burstein–Moss effect, which has been observed in substitutionally doped MoS_2 fullerenes [78], should lead to a blue shift with increasing excited-state population. Our contrasting observation implies that any Burstein–Moss contribution is overwhelmed by one or more red-shifting mechanisms.

3.4.1 Conclusion

We have developed a scenario of the exciton and charge dynamics in few-layer MoS_2 where femtosecond pump-probe results are best described assuming that the primary photoexcitations are excitons which dissociate efficiently with a characteristic time of 700 fs. Thus few-layer MoS_2 displays a behavior which is intermediate between conventional semiconductors on the one hand, and high exciton binding energy materials, such as organic semiconductors, carbon nanotubes, and presumably single-layer MoS_2 on the other. Our results suggest that few-layer MoS_2 flakes can be employed in high efficiency photodetectors and photovoltaic elements. Such devices have been shown based on monolayer field-effect transistors [79], [80]. However, due to the higher exciton binding energy, in the monolayer the CPG yield is expected to be significantly lower. This assumption is corroborated by the observation that measures which facilitate exciton dissociation have strongly improved the efficiency of such devices. Such measures include a strong built-in field using appropriate electrode materials, by engineering a p-n junction [81], [82], or by combining MoS_2 with a second material [83]–[85], so that one of them acts as electron donor and the other as acceptor in a heterojunction. According to our findings, in few-layers, which have the added benefit of absorbing a larger fraction of the incident light, such measures should not be necessary and simpler, more scalable device structures could be used.

Chapter 4

Quasiparticles vs many-body interactions in photoexcited MoS_2

Strong electron-electron interaction in two-dimensional semiconductors like MoS_2 lead to strongly bound excitons, accompanied by sizable bandgap renormalization effects, both upon doping and photoexcitation. The transient spectra and their evolution in femtosecond optical experiments have been assigned either to the population dynamics of excitons and free charges, or, alternatively, to linewidth changes and shifts due to bandgap renormalization and screening of the exciton binding potential. Here we use femtosecond optical pump-probe spectroscopy on an ensemble of MoS_2 flakes from liquid exfoliation to distinguish between these effects. Rather than confirming one and refuting the other of two apparently opposing interpretations of the transient spectra, we find that both contributions are relevant, with the lineshape changes and shifts more important during the first picosecond, i.e. during the electron-phonon relaxation, and the population effects dominating the signal at subsequent delays. By disentangling these two contributions, our analysis shows how to extract more and more relevant information from future and existing femtosecond optical data on two-dimensional semiconductors.

Strong spatial confinement and strongly reduced screening in low-dimensional materials leads to important interactions between photoexcited electrons and holes [3]. Consequently, the single-particle picture is insufficient to describe their photophysics and many-body electron interactions have to be taken into account. Usually photoexcitation creates bound states of two (excitons), three (trions) or four (biexcitons) electrons/holes which interact much stronger with each other than with all other electrons and holes. Hence these few-particle states are described as quasiparticles, with all other interactions treated as a renormalizing background.

Transition metal dichalcogenides such as MoS_2 and WS_2 are two-dimensional semiconductors that have garnered a lot of attention recently [86], [87] since they enable high-mobility, low-off current nanotransistors [88] and are amenable to low-cost, high-throughput processing techniques in liquid [89]–[91]. Their unprecedentedly strong light-matter interaction [92], [93] (a monolayer of 0.7 nm thickness absorbs about 10% of the incident light) qualifies them for photonic and optoelectronic applications such as high-sensitivity photodetectors [80], photovoltaic cells [83], or electroabsorption modulators [47]. Excitonic resonances, conventionally labeled A, B, C, etc. (see also Fig. 4.1a) dominate their absorption spectra. In the presence of charges from electrical injection [28] or chemical doping [53], three-particle charged photoexcited states (trions) have been observed for the lowest energy A resonance. The absorption and fluorescence features involving trions are usually red-shifted by 30-70 meV ([28]) from the exciton transitions. Due to the typical linewidth of around 100 meV FWHM at room temperature, the exciton and trion peaks

merge into one. Additionally, two opposing excitation density dependent renormalizations have been observed [37]: a reduction of the electronic gap (band gap renormalization BGR), which shifts the electronic transitions towards lower energies, and a lowering of the exciton binding energy due to stronger screening, which partially compensates the red shift due to BGR.

The non-equilibrium optical properties and the relaxation dynamics of semiconductors are customarily studied using femtosecond pump-probe spectroscopy, where a pump pulse excites the sample and a weaker, broadband probe pulse measures the differential transmission (ΔT/T) as a function of probe frequency ω and pump-probe delay τ. In the small-signal limit, this quantity is directly related to the photoinduced change in absorbance ΔA:

$$\Delta A(\omega,\tau) = A(\omega,\tau) - A_0(\omega) \simeq -\frac{\Delta T}{T}(\omega,\tau), \tag{4.1}$$

where $A_0(\omega)$ and $A(\omega,\tau)$ are the stationary and time-dependent absorbance, respectively. Writing the stationary absorbance as $A_0(\omega) = d\sum_i(n_i\sigma_i(\omega))$, with n_i being the density of absorbers, $\sigma_i(\omega)$ their frequency-dependent absorption cross section, and d the sample thickness, we obtain:

$$\Delta A(\omega,\tau) = d\sum_i(\Delta n_i(\tau)\sigma_i(\omega) + n_i(t)\Delta\sigma_i(\omega,\tau)), \tag{4.2}$$

with the index i denoting the ground state and the various excited state populations. The first term reflects the photoinduced changes in the populations, which change the intensity of a spectral feature (such as the area under an absorption peak). The second term represents shifts in the absorption spectra as a consequence of photoexcitation-induced many-body interactions, such as BGR or screening of the exciton binding energy. Femtosecond studies on semiconducting TMDCs have been interpreted as either the relaxation behavior of photoexcited excitons, or charge carriers, or both [94]–[98], implicitly assuming that the signal is dominated by the first term in Eq. (4.1). Recently, however, it was shown that the ΔT/T spectrum of monolayer MoS_2 at short delays [36] can also be explained by assuming a signal that is dominated by the second term in Eq. (4.2). The ΔT/T spectrum has a derivative-like shape, consistent with peak shifts due to the band gap renormalization, which is not completely compensated by the screening of the exciton binding energy.

Here we show how to disentangle the quasiparticle and many-body contributions to the pump-probe signal of few-layer MoS_2 flakes obtained from liquid exfoliation dispersed in the transparent polymer PMMA, as used in a previous study [94]. We present a non-standard analysis that demonstrates that photoexcitation close to the C exciton resonance immediately leads to a derivative-like signal due to renormalization of the band gap and the exciton binding energy. Subsequently, the photoinduced absorption by charge carriers and the bleaching of the exciton resonance form on a time scale of 1 ps. The discussion represents our current understanding of these processes, which still leaves some open questions.

4.1 Results and Discussion

The extinction spectrum of the MoS_2 flakes in Fig. 4.1a shows the characteristic A, B, and C excitonic resonances. A and B belong to excitons at the conduction and valence band (CB and VB) minima/maxima at the K point, where the energy difference between A and B is given mostly by the spin-orbit splitting of the VB. The C exciton has been ascribed to a transition between the valence and conduction bands in a band nesting region slightly off the Γ point [18], [36], [99]. Due to n doping of the starting material, the A and B

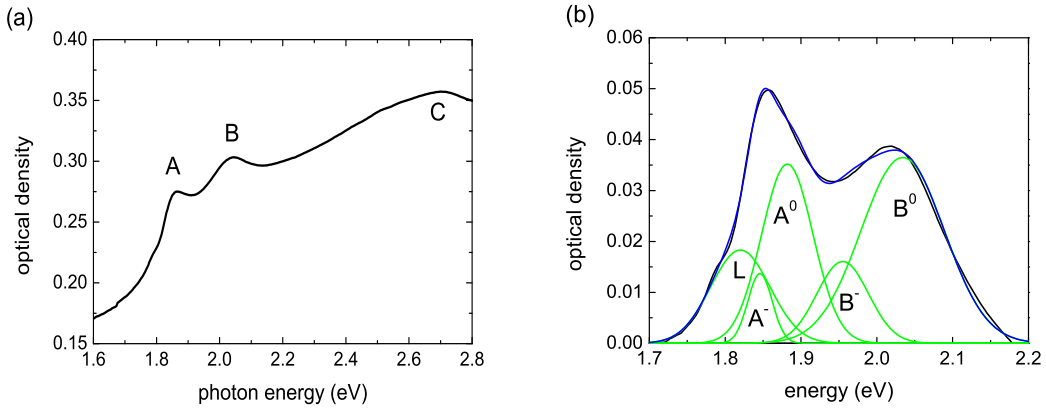


Figure 4.1: (a) Extinction spectrum of few-layer MoS_2 in PMMA. (b) exciton and trion contributions to the extinction spectrum, showing the background corrected extinction (black), and the fit as the sum (blue) of five Gaussians (green, labeled).

features are composed of two peaks, the transitions A^0 and B^0 from a neutral ground state to an exciton and the transitions A^- and B^- from a (negative) charged state to a trion [28]. Additionally, at the low energy side of the A peak, a low energy feature from a transition between neutral states is observed [49] and is customarily denoted as L (for low energy) and ascribed to surface trapped excitons [100]. Fig. 4.1b shows the extinction spectrum in the spectral region of the A and B features with a generic background subtracted (to minimize the scattering contributions and overlap with higher energy absorption features) and fitted to five Gaussian peaks representing the L, A^-, A^0, B^-, and B^0 transitions.

The pump-probe spectrum at selected pump-probe delays is shown in Fig. 4.2a for excitation at a fluence of 10^{15} cm^{-2} at a photon energy of 3.1 eV. It shows an increased

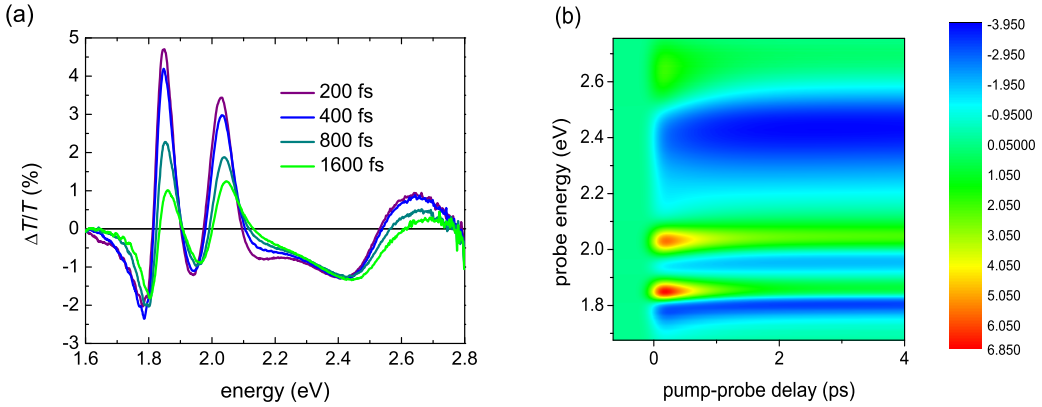


Figure 4.2: (a) Transient differential transmission spectrum of MoS_2 in PMMA for selected pump-probe delays. (b) contour plot of $\Delta T/T$ in %.

transmission (photobleaching, PB) for both peaks A and B, and a reduced transmission (photoinduced absorption, PA) on both sides of the A and B peak. The bleaching and the

PA around 2.1 eV rise during the instrument resolution of ∼100 fs and decay monotonically for increased pump-probe delay, while the two other PA (photoinduced absorption) features rise monotonically over several hundred fs. Such variegated behavior suggests that the signal does not simply follow the generation and decay of one photoexcited population, but at least two distinct ones. Additionally, all spectral features shift monotonically to higher energies. This suggests that the transition energies that compose the spectrum may depend on the density of excited states, pointing towards a BGR contribution (whose temporal dynamics is again related to the population dynamics).

To disentangle the contributions from different populations and their action on the strength and energy of the individual spectral features, rather than the customary analysis of $\Delta T/T$, we look directly at the transient absorption spectra. According to Eq. (4.1), the transient absorption spectrum of the excited sample is simply the difference between the static absorption and $\Delta T/T$, which we report in Fig. 4.3. All five relevant peaks shift

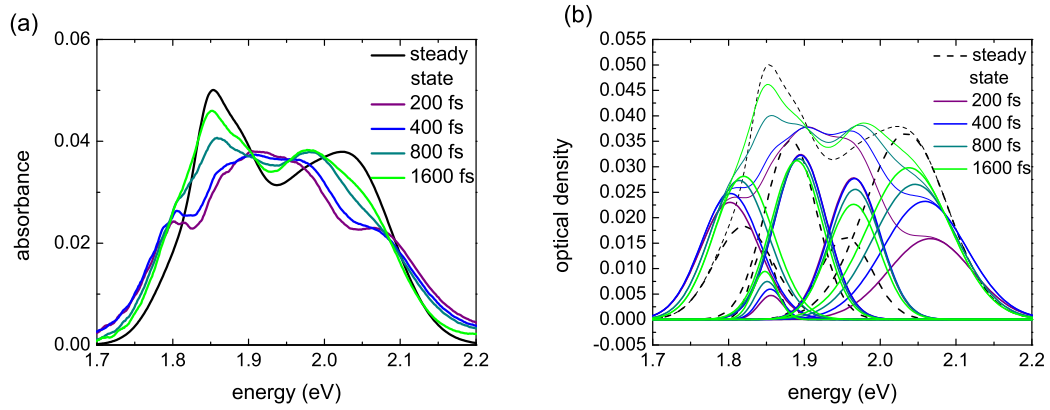


Figure 4.3: (a) Transient absorption spectra (spectra in Fig. 4.2a subtracted from the spectrum in Fig. 4.1b). (b) Exciton and trion contributions to the transient absorption spectra.

during the instrumental resolution, the low energy feature to the red by approximately 20 meV, and the others to the blue by amounts ranging from 10 (for A^0) to 30 meV (for B^0). Most of the peaks, which together form a steady-state absorption spectrum that shows only two main peaks due to their overlap, are now further apart, leading to a more faceted transient spectrum. All peaks relax back to their equilibrium position with a time constant of roughly 1ps, the time scale of electron-phonon relaxation [94]–[98]. In addition to the transient change in the peak positions, they also change their area, which is representative of the joint density of states available for a given transition, from a threefold decrease of A^- to an almost twofold increase of B^- during the instrument resolution. For L and A^0 this change in area continues to grow for a few ps, while for the other three features it relaxes back on the same time scale. Hence the transient absorption spectrum of MoS_2 is determined by two contributions (corresponding to the two terms in Eq. (4.1)): shifts due to the joint action of BGR and exciton screening, and the non-equilibrium population of the relevant energy levels. During the first few ps the two contributions are of similar strength, while later the population effect dominates.

The time-dependent positions and areas of all peaks are shown in Fig. 4.4. The immediate shifts upon photoexcitation suggest that renormalization happens as an immediate consequence of photoexcitation into the C exciton. Additionally, the photoinduced change

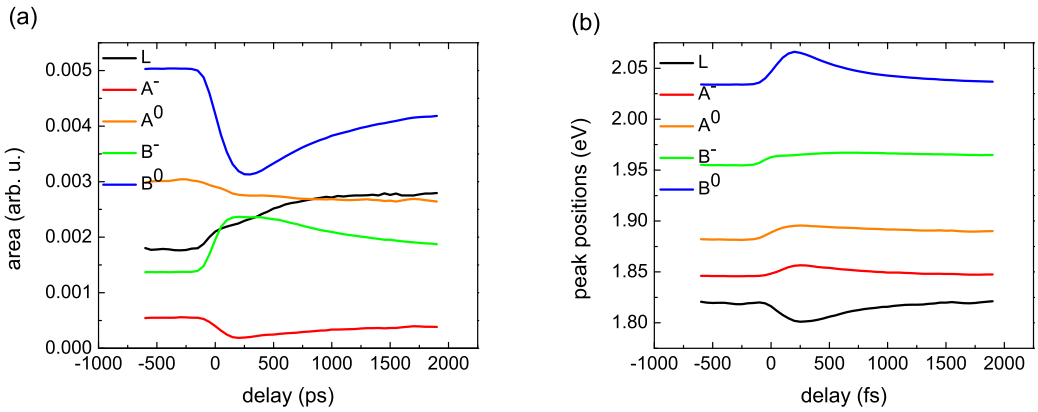


Figure 4.4: (a) Transient absorption spectra (spectra in Fig. 4.2a subtracted from the spectrum in Fig. 4.1b). (b) Exciton and trion contributions to the transient absorption spectra.

in population enhances the L and in particular the B^- feature, while it bleaches B^0 and A^-, and, to a lesser extent, also A^0. The enhancement of L and the bleaching of A^0 continue to grow after photoexcitation, while the areas of the other features relax. The interpretation for B^- and B^0 is straightforward: positions in the band structure which can participate in the formation of B trions are populated, hence the transition that forms them is enhanced, while that which forms B excitons is proportionally reduced. Subsequent relaxation depopulates these states again, leading to the relaxation of the peak areas towards their equilibrium value. The situation for the L, A^-, and A^0 peaks is more intricate. Photoexcitation initially decreases A^0 only slightly, but strongly reduces A^-, while it increases the L peak. The reduction of A^- is subsequently reverted, while the trend for the other two peaks continues. Apparently, photoexcitation depopulates those charged states that enable A^- trion formation and additionally enables additional surface trapped excitons, at the expense of A^0 excitons. Subsequent relaxation replenishes the charges that enable A^- trions, but continues to enable further surface trapped excitons. Hence the assignment of the L peak must be reviewed. Either many surface traps are inactive and are activated by photoexcitation (e.g. through a change in the level alignment due to photoinduced BGR), or the origin of the L peak is different altogether.

In light of these findings, we can reassess the existing literature to obtain a more comprehensive picture of the photoexcitation dynamics in few-layer TMDCs. Photoexcitation into the C exciton or other higher electronic levels not involved in the A and B transitions instantly renormalize the band gap and the exciton binding energy. Hence the early (the first few picoseconds) signal in many studies has a strong renormalization contribution leading to a lineshape that strongly resembles a first derivative of the absorption spectrum if all involved transition energies shift uniformly in one direction, or a second derivative if the peaks fan out as in our case. For each transition, the energy shift is the result of two opposite contributions, BGR and lowering of the exciton binding energy due to screening. Which of the two dominates may be different for each case, e.g. in monolayer MoS_2 all four peaks (of a CVD sample that shows no L peak) initially shift to the red [36], for WS_2 nanoinks [101] A^- and A^0 shift in opposite directions. During the initial electron relaxation, the renormalization effect is reduced and population effects increasingly dominate the $\Delta T/T$ spectrum and its temporal evolution.

4.2 Conclusion

We have disentangled the quasiparticle and the many-body contributions to the femtosecond pump-probe signal. In samples with overlapping peaks conventional analysis methods usually do not allow this distinction. The analysis presented here enabled us to develop a more comprehensive picture of the photoexcitation dynamics in few-layer TMDCs and may do so also in other situations, for example monolayers, or high excitation densities.

Chapter 5

Doping signatures in the Raman spectrum of monolayer WSe_2

Layered two-dimensional materials such as the transition metal dichalcogenides show a broad range of interesting optical and electronic properties that depend strongly on the number of layers [4], [102]. Given the importance of this number, several metrics have been proposed to obtain it rapidly from spectroscopic measures such as the distance between Raman peaks [15] or details of the absorption spectrum [24]. However, none of these metrics allows an unambiguous identification of the layer number. In the case of the Raman spectrum, the distance between the dominant peaks is not only a function of the layer number, but also of the level of doping introduced during the synthesis [103]. Similarly, the A and B resonances in absorption originate from the overlap of exciton and trion peaks; hence the exact position of the composite peaks depends not only on the number of layers, but also on the relative strength of the exciton and trion contributions, which again depends on doping [28]. Hence, the currently used metrics need to be complemented by an additional measure of the doping level.

Here we study the Raman spectrum of monolayer WSe_2 in a field effect transistor (FET) configuration with a polymer electrolyte gate, which allows to vary the charge density in the monolayer over a wide range. We monitor the three most prominent Raman peaks and correlate different aspects, such as the distance or intensity ratio between combinations of two peaks with this charge density in the FET channel. From this we propose several additional metrics to complement existing ones for more accurate material characterization.

The Raman spectrum of semiconducting monolayer $2H$-WSe_2 in the region 200-300 cm^{-1} consists of three modes: the out of plane $A_1^{'}$, the in plane $E^{'}$ and the second order 2LA mode, caused by frequency doubling of the LA (M) phonon at 130 cm^{-1}. The $A_1^{'}$, and $E^{'}$ modes are degenerate in the monolayer, located around 250 cm^{-1} [104]. Due to the symmetry the $A_1^{'}$ mode is observed only for the scattered light with the same polarization, as the excitation and vanishes in the cross-polarized Raman geometry $Z(XY)\bar{Z}$. The metallic monolayer 1T-WSe_2 phase shows additional Raman peaks between 50 and 150 cm^{-1} [105].

In our experiment we measured polarization-resolved Raman scattering on a monolayer WSe_2 field-effect transistor (FET) (See Figure 4.1(a)). The WSe_2 transistor shows ambipolar characteristics with the on states in the n-region above 1 V and in the p-region below -2.2 V (Figure 4.1(b)). The transistor was fabricated with the liquid gate on top to enable the injection of significant charge densities already at gate voltages of few volts. The area normalized capacitance of polymer electrolytes varies between 1 and 10 μFcm^{-2} [106]–[110].

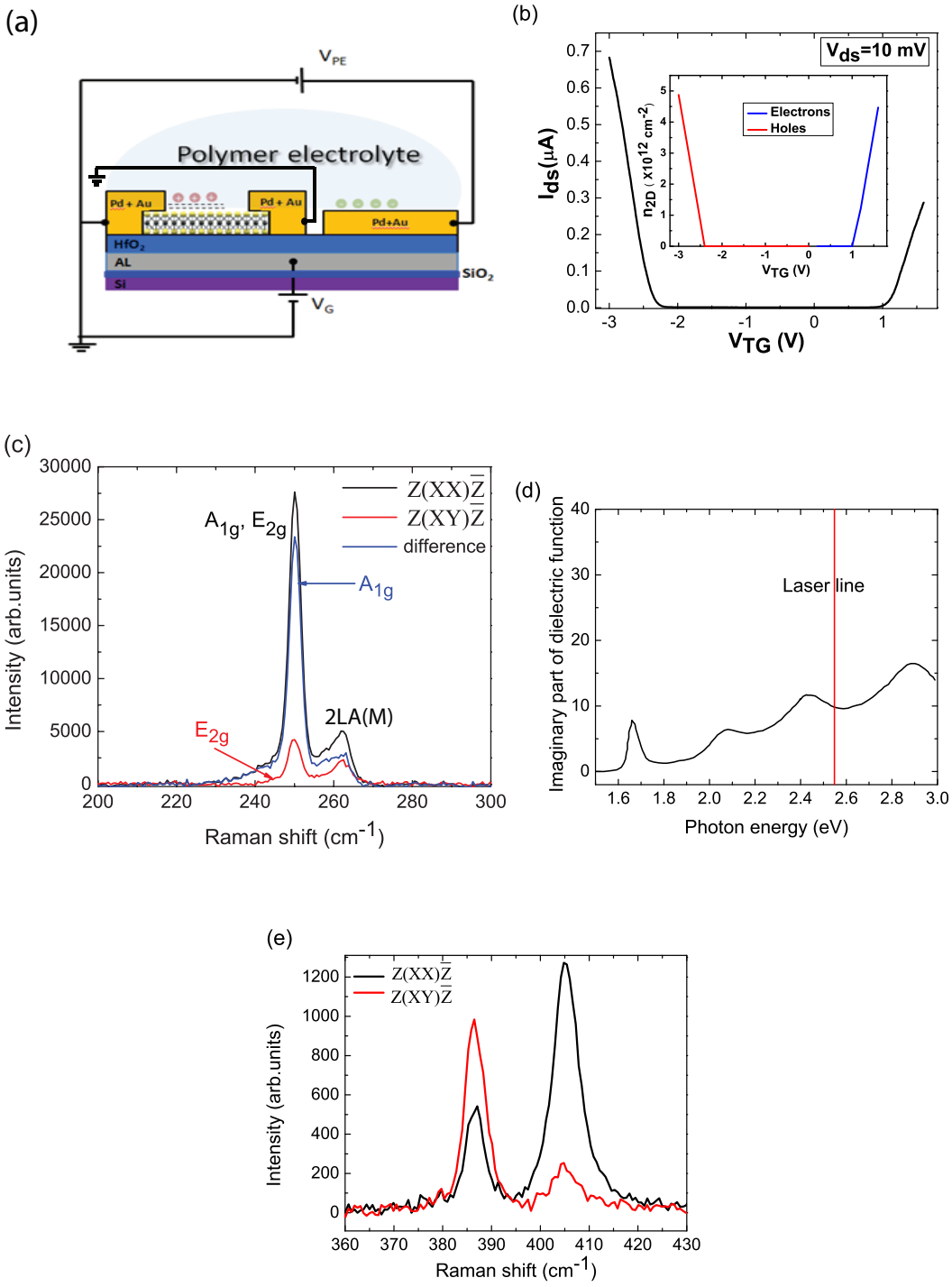


Figure 5.1: (a) Scheme of the WSe_2 FET. (b) transistor characteristics with an estimate of the gate-dependent charge density in the channel. (c) Raman spectrum for parallel and cross polarization at 0 gate voltage. (d) dielectric function of WSe_2 [111]. (e) Raman spectrum of MoS_2 FET for parallel and cross polarization at 0 gate voltage.

Taking a conservative estimate of 1.3 μFcm^{-2} [48], the number of injected carriers per unit area is 0.12-0.48$*10^{13}$ cm^{-2} (See Figure 4.1(b)) ($n_{2D} = \frac{C_{IL}}{e}|V_{TG} - V_{th}|$, where n_{2D} – density of charges in the channel, C_{IL} – capacitance of polymer electrolyte, V_{TG} – top-gate voltage, V_{th} – threshold voltage value at which transistor is in the "on"-state, e – elementary charge). Using the top liquid gate we injected carriers to the channel and observed how the Raman signal under different polarizations changed. We observed changes in intensity, width and positions for the $A_1^{'}$, $E^{'}$ and 2LA(M) modes and assess how they can be used to develop a metric for the determination of the charge density in monolayer WSe_2 from Raman measurements.

5.1 Results and Discussion

As the first step, we verify that our data have a reliable polarization and are only from the $2H$ polytype of WSe_2. We performed polarization dependent Raman spectroscopy on MoS_2 control sample (Figure 4.1(e)). From this we can safely rule out any influence on the excitation light polarization from the polymer. On the WSe_2 FET we observe the characteristic $A_1^{'}$, $E^{'}$, and 2LA(M) modes (See Figure 4.1(c)). Additional modes in the range of 100 – 150 cm^{-1}, characteristic of the 1T phase of WSe_2, are absent over the whole range of gate voltages. We therefore conclude that the injected charge carriers do not induce a polytype transition and our Raman signal originates from the pure $2H$ polytype over the whole range of charge densities.

The Raman spectrum in the region of the three relevant peaks is shown in Figure 4.2 for different relative polarizations of excitation and detection (parallel and cross-polarization) for different gate voltages. We can distinguish four gate voltage regimes: the p-on region for voltages below -2.2 V, the p-off region between -2.2 and -1.0 V, the n-off region from -1 to +1 V and the n-on region above 1 V. In principle, the size of the off region should be given by the band gap of WSe_2 [108]. However, it is frequently found that a region where the transistor is strictly “off” is only seen in a logarithmic representation, provided the noise level is low enough. Here, we view the source-drain current as an indicator of the induced charge density. Hence, even if the transistor is not strictly “off”, but the charge density is small, we do not expect an appreciable change in the Raman signal. Therefore, for us the whole region where the current is low and not steeply changing with the source-drain voltage can be considered as “off”. This region is broader by about 1V than the band gap of WSe_2 suggests. Moreover, from the behavior of the Raman signal, as we shall discuss in detail below, it can be divided into two sub-regions, which we call p-off and n-off. This is due to the fact that the Raman signal depends not only on the charge density in the channel, but also on the dielectric environment. This, in turn, depends on the different polarizability of the polymer electrolyte induced by different ions type under switching gate voltages. Hence, we assign the crossover point between the n-off and p-off region as the point where the polarization of the polymer electrolyte is inverted. The peak at 250 cm^{-1} originates from the $E^{'}$ mode for cross-polarization and from the sum of the $E^{'}$ and the about six times stronger $A_1^{'}$ mode for parallel polarization. Both modes are strongest in the n-off region and decrease strongly in the p-off and slightly in the p-on region. In the n region the $A_1^{'}$ mode decreases while the $E^{'}$ mode decreases slightly in height, but also substantially broadens. Hence its apparent area increases, which is partially an artefact due to the increased overlap with the 2LA(M) peak. The 2LA(M) peak is strongest in the n-off- and p-off regions; in the p region it decreases with increased charge injection, in the n region it decreases and shifts towards the red until at 1.6 V it becomes indistinguishable from the $A_1^{'}$ and $E^{'}$ modes. In both on regions, the 2LA(M) has a rather poor signal-to-noise ratio, which puts a large error on its area. Hence, in developing the metric, we will

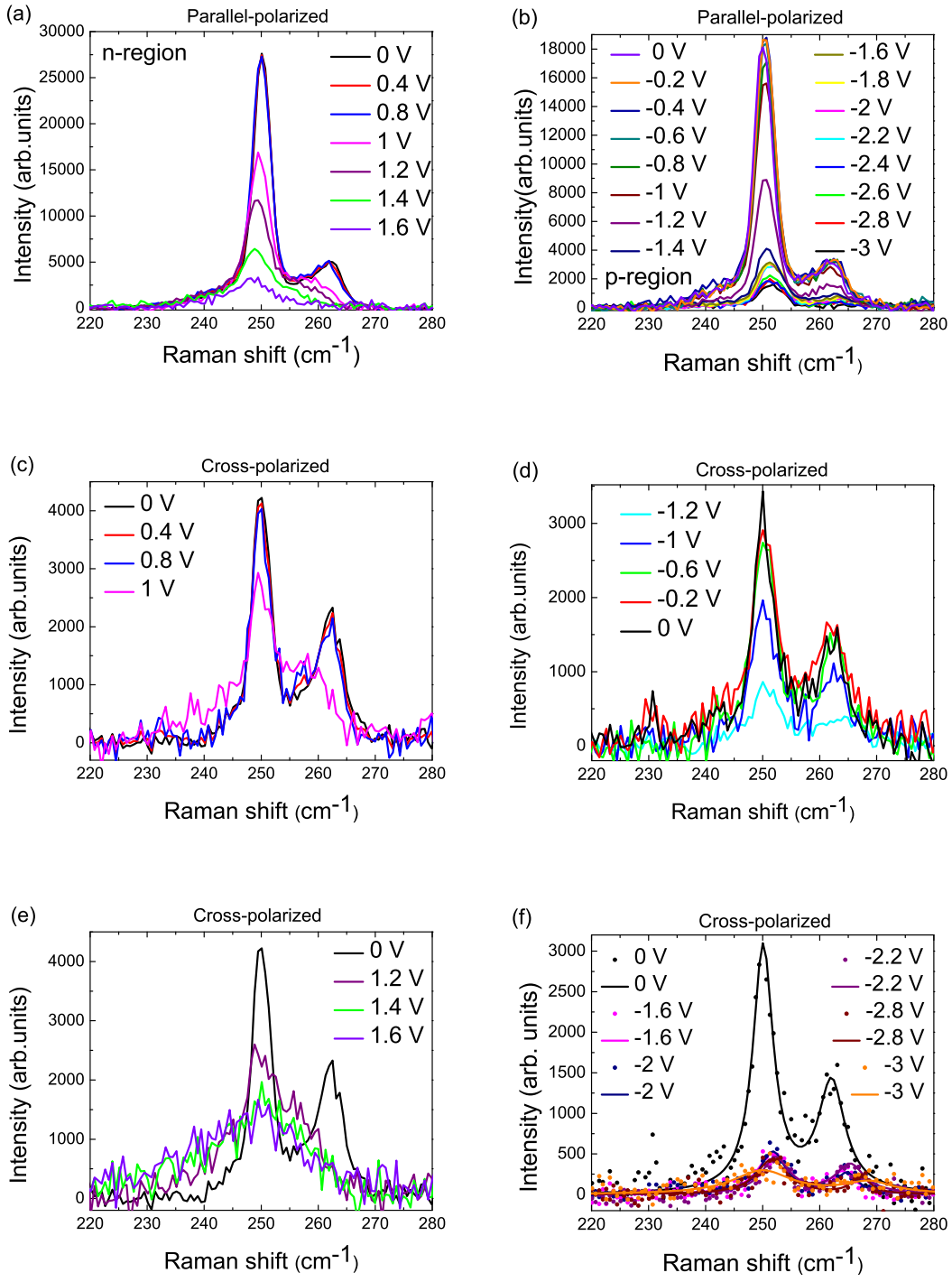


Figure 5.2: Raman signals for parallel (a,b) and cross polarization (c-f) in the n (a,c,e) and p (b,d,f) regions. Due to the poor signal-to-noise levels, Figure (f) shows the fits to three Lorentzians in addition to the original data.

use only its position, not its area.

We fit the obtained spectra with three Lorentzians (or two in the cases where two peaks become indistinguishable) and plot their positions, widths, and areas to explore which of them is most suited as a metrics for the charge density. Figure 4.3 shows the intensities (i. e. areas under the peaks), ratios between different peak areas, widths, positions, and distances as a function of the gate voltage. Absolute intensities of all peaks, depicted in Figures 4.3 (a, b) show a plateau for the n-off region and decrease sharply upon entering the p-off region, staying relatively constant over the p-off and p-on regions. For the n region there is a similar sharp decrease in intensity, except for the $E^{'}$ peak, which increases strongly. Absolute intensities have limited applicability as a metric to compare different samples; they can only be used to compare different doping levels of the same sample measured in the same geometry, such as for in-situ monitoring of doping levels.

The intensity ratio between $A_1^{'}$ and $E^{'}$ shows a plateau-like shape (except for the outlier at -1.2 V), with an almost constant value of 4 for the whole n-off and p-off regions (Figure 4.3(b)). For both on states, the ratio changes sharply with similar slope. Hence, in principle, these ratios could constitute a reasonable metric for the absolute charge density, when the sign is not important.

The peak widths generally remain constant over the n-off and p-off regions and increase for charge injection of either polarity (Figures 4.3(c) and (d)). However, for the p-on region, there seems to be a bit of a lag compared to the transistor characteristics, which makes the widths less reliable as a metric. However, if one suspects that a sample is significantly doped and is looking for confirmation, then one can find it in the $A_1^{'}$+$E^{'}$ ($E^{'}$) peak being broader than 5 (7) cm^{-1}.

Finally, we take a look at the peak positions. While $A_1^{'}$ and $E^{'}$ shift monotonously with the gate voltage over all four regions (Figure 4.3(e)), the distances of both peaks from 2LA(M) closely follow the charge density – with 12 cm^{-1} for the whole off region, higher values for p and lower values for n doping (Figure 4.3(f)). Also, compared to other possible metrics, they change less abruptly with relatively constant slope.

Having identified the ratios between peak $A_1^{'}$ and $E^{'}$ as a reasonable metric for the absolute value of the charge density and the distance between 2LA(M) and either of the other two as the most promising metric for the charge density including sign, we now plot these values as a function of the estimated charge density (Figure 4.4). Please note that we use a conservative estimate for the capacity of the ionic gate, hence the actual charge density in the channel may be higher and hence the depicted slope of the metrics vs charge density is an upper limit.

5.2 Conclusions

We have recorded the three salient Raman peaks of monolayer WSe_2 as a function of the charge density, which we controlled via the gate voltage in an FET using a polymer electrolyte. By analyzing their positions, widths and intensities we derived several metrics to determine the charge density. The fact that we have found several metrics for the charge density suggests a strategy for developing a more comprehensive metric that can simultaneously yield the charge density and the number of layers, which will allow rapid throughput screening of mono- and few-layer material obtained by different methods ranging from chemical vapor deposition to liquid exfoliation.

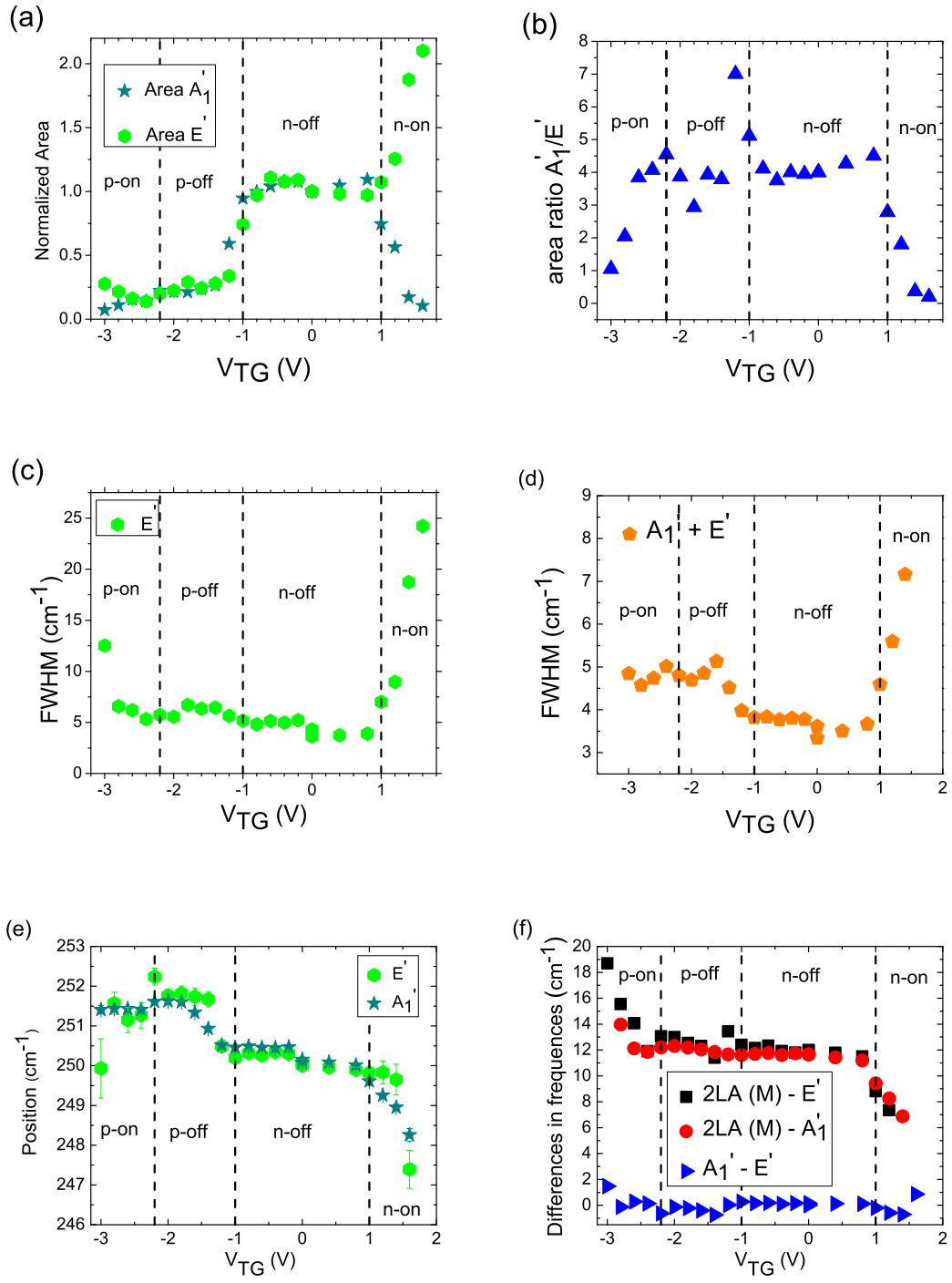


Figure 5.3: (a) Normalized (to the areas of E' and $A_1^{'}$ peaks at 0 V top gate voltages) area for E' and $A_1^{'}$ peaks at different gate voltages. (b) Area ratio for E' and $A_1^{'}$ peaks. (c-d) Full width at half maximum (FWHM) for peak E' and peak E'+$A_1^{'}$. (e) Positions of E' and $A_1^{'}$ peaks at different voltages. (f) Relative positions of 2LA (M), E' and $A_1^{'}$ peaks as function of voltages.

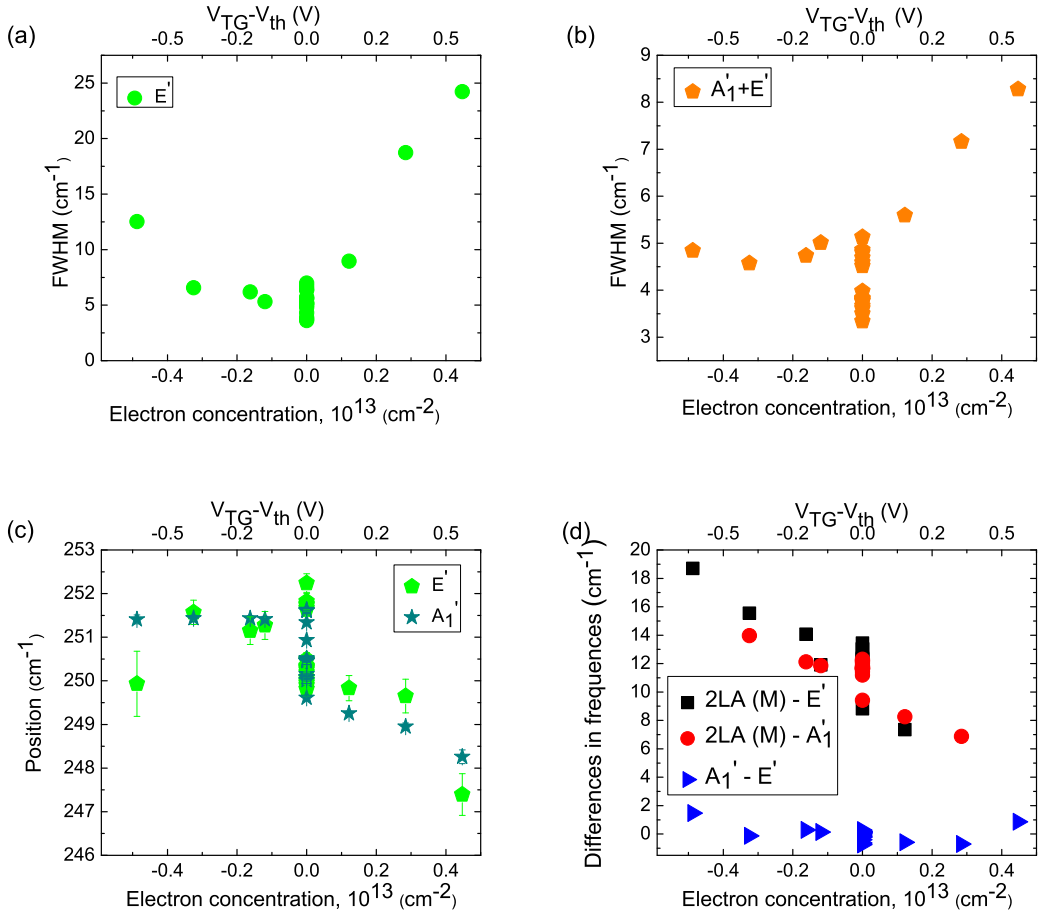


Figure 5.4: (a-b) Metrics: full width at half maximum (FWHM) for peak E' and peak E'+A_1' as a function of charge density (n, bottom axis) and applied gate voltages (V_{TG}) (top axis) represented as | V_{TG}-V_{th} | (where V_{th}=2.4 V for n≤0, V_{th}=1.05 V for n≥0). (c) Metric: Positions of E' and A_1' peaks as a function of charge density (n, bottom axis) and applied gate voltages (V_{TG}) (top axis) represented as | V_{TG}-V_{th} | (where V_{th}=2.4 V for n≤0, V_{th}=1.05 V for n≥0). (d) Metric: Relative positions of 2LA (M), E' and A_1' peaks as a function of charge density (n, bottom axis) and applied gate voltages (V_{TG}) (top axis) represented as | V_{TG}-V_{th} | (where V_{th}=2.4 V for n≤0, V_{th}=1.05 V for n≥0).

Chapter 6

Conclusions

In the present thesis I investigated the equilibrium and non-equilibrium optical properties of two-dimensional materials, such as MoS_2 and WSe_2. The spectroscopic techniques used for the investigation were femtosecond optical pump-probe, continuous wave photomodulation, and Raman spectroscopy. By studying the ultrafast response of few-layer MoS_2 I found that there are two ensemble populations of photoexcited species involved in the relaxation dynamics. The second population grows as the first one decays. We developed a scenario where the first population is dominated by excitons, which are either directly photoexcited or formed during the experimental time resolution (<100 fs). Subsequently, these excitons dissociate into charge carriers with a time constant of 700 fs for excitation at 3.1 eV. These carriers also cause a time-dependent shift (via Stark effect or band gap renormalization) of the pump-probe spectral features, whose magnitude depends on the excitation density. The exciton dissociation yield depends strongly on the excitation wavelength: excess energy relative to the exciton resonance increases the yield. This points towards a mechanism where the surplus energy helps the dissociation (e.g. through electron-phonon scattering during the relaxation of "hot" excitons). Additionally, also scattering on defects may contribute to the exciton dissociation.

I reassessed the origin of the pump-probe signal of few-layer MoS_2 during the first few picoseconds. There is a disagreement in the literature whether it is dominated by population dynamics – the interpretation used in Chapter 3 of this thesis — or by peak shifts due to band gap renormalization. To this end, the more in-depth analysis traces the positions and areas of the A and B exciton and trion peaks individually. From this analysis the following picture emerges: photoexcitation into the C exciton or other higher electronic levels not involved in the A and B transitions instantly renormalizes the band gap and the exciton binding energy. Hence the early signal has a strong renormalization contribution leading to a derivative lineshape. For each transition, the energy shift is the result of two opposite contributions, band gap renormalization and exciton screening. During the initial electron relaxation, the renormalization effect is reduced and population effects increasingly dominate the $\frac{\Delta T}{T}$ spectrum and its temporal evolution.

Spectroscopic metrics may enable rapid throughput characterization of 2D materials. Here I assessed the use of the Raman spectrum of WSe_2 in an ionic-liquid gated ambipolar field-effect transistor as a metric of the doping level. I observed that charge injection suppresses characteristic Raman modes, which reduces the possibility to find a reliable metric. However, I identified two promising candidates: the intensity ratio between the $A_1^{'}$ and $E^{'}$ modes and the distance between the 2LA(M) and the $A_1^{'}$ ($E^{'}$) modes. The intensity ratio between the $A_1^{'}$ and $E^{'}$ modes follows the transistor characteristic: it is constant in the off-region and decreases sharply in both on regions. The distance of both peaks from the 2LA(M) peak follows the transistor characteristic and also is sensitive to

the sign of the injected charge: it is constant in the off-region, decreases in the n-on region and increases in the p-on region. As an alternative candidate for the metrics I tried the widths of the $E^{'}$ as well as the composite peak formed by $E^{'}$ and $A_1^{'}$, but they follow the transistor characteristics only in the n on-region.

References

[1] R. S. Knox, "Introduction to exciton physics," in *Collective Excitations in Solids*, B. D. Bartolo, Ed. Springer, 1983.

[2] M. Fox, *Optical properties of solids*. Oxford University Press, 2001.

[3] A. Yoffe, "Low-dimensional systems: Quantum size effects and electronic properties of semiconductor microcrystallites (zero-dimensional systems) and some quasi-two-dimensional systems," *Advances in Physics*, vol. 42, no. 2, pp. 173–262, Apr. 1993. DOI: 10.1080/00018739300101484. [Online]. Available: http://dx.doi.org/10.1080/00018739300101484.

[4] K. F. Mak, C. Lee, J. Hone, J. Shan, and T. F. Heinz, "Atomically thin MoS_2 : A new direct-gap semiconductor," *Physical Review Letters*, vol. 105, no. 13, Sep. 2010. DOI: 10.1103/physrevlett.105.136805. [Online]. Available: http://dx.doi.org/10.1103/PhysRevLett.105.136805.

[5] A. Enyashin and G. Seifert, "Electronic properties of MoS_2 monolayer and related structures," *Nanosystems: Physics, Chemistry, Mathematics*, vol. 5, no. 4, pp. 517–539, 2014.

[6] G.-B. Liu, W.-Y. Shan, Y. Yao, W. Yao, and D. Xiao, "Three-band tight-binding model for monolayers of group-VIB transition metal dichalcogenides," *Physical Review B*, vol. 88, no. 8, Aug. 2013. DOI: 10.1103/physrevb.88.085433. [Online]. Available: http://dx.doi.org/10.1103/PhysRevB.88.085433.

[7] A. Kuc, N. Zibouche, and T. Heine, "Influence of quantum confinement on the electronic structure of the transition metal sulfide TS_2," *Phys. Rev. B*, vol. 83, no. 24, Jun. 2011. DOI: 10.1103/physrevb.83.245213. [Online]. Available: http://dx.doi.org/10.1103/PhysRevB.83.245213.

[8] M. I. Katsnelson, *Graphene: Carbon in Two Dimensions*. Cambridge University Press, 2012.

[9] E. Cappelluti, R. Roldán, J. A. Silva-Guillén, P. Ordejón, and F. Guinea, "Tight-binding model and direct-gap/indirect-gap transition in single-layer and multilayer MoS_2," *Physical Review B*, vol. 88, no. 7, Aug. 2013. DOI: 10.1103/physrevb.88.075409. [Online]. Available: http://dx.doi.org/10.1103/PhysRevB.88.075409.

[10] T. Cheiwchanchamnangij and W. R. L. Lambrecht, "Quasiparticle band structure calculation of monolayer, bilayer, and bulk MoS_2," *Phys. Rev. B*, vol. 85, no. 20, May 2012. DOI: 10.1103/physrevb.85.205302. [Online]. Available: http://dx.doi.org/10.1103/PhysRevB.85.205302.

[11] A. Kormányos, G. Burkard, M. Gmitra, J. Fabian, V. Zólyomi, N. D. Drummond, and V. Fal'ko, "K·p theory for two-dimensional transition metal dichalcogenide semiconductors," *2D Materials*, vol. 2, no. 2, p. 022 001, 2015.

[12] X. Xu, W. Yao, D. Xiao, and T. F. Heinz, "Spin and pseudospins in layered transition metal dichalcogenides," *Nat Phys*, vol. 10, no. 5, pp. 343–350, Apr. 2014. DOI: 10.1038/nphys2942. [Online]. Available: http://dx.doi.org/10.1038/NPHYS2942.

[13] J. M. Riley, F. Mazzola, M. Dendzik, M. Michiardi, T. Takayama, L. Bawden, C. Granerød, M. Leandersson, T. Balasubramanian, M. Hoesch, T. K. Kim, H. Takagi, W. Meevasana, P. Hofmann, M. S. Bahramy, J. W. Wells, and P. D. C. King, "Direct observation of spin-polarized bulk bands in an inversion-symmetric semiconductor," *Nature Physics*, vol. 10, no. 11, pp. 835–839, Oct. 2014. DOI: 10.1038/nphys3105. [Online]. Available: http://dx.doi.org/10.1038/NPHYS3105.

[14] A. Molina-Sánchez, K. Hummer, and L. Wirtz, "Vibrational and optical properties of MoS_2: From monolayer to bulk," *Surface Science Reports*, vol. 70, no. 4, pp. 554–586, Dec. 2015. DOI: 10.1016/j.surfrep.2015.10.001. [Online]. Available: http://dx.doi.org/10.1016/j.surfrep.2015.10.001.

[15] C. Lee, H. Yan, L. E. Brus, T. F. Heinz, J. Hone, and S. Ryu, "Anomalous lattice vibrations of single- and few-layer MoS_2," *ACS Nano*, vol. 4, no. 5, pp. 2695–2700, May 2010. DOI: 10.1021/nn1003937. [Online]. Available: http://dx.doi.org/10.1021/nn1003937.

[16] X. Zhang, W. P. Han, J. B. Wu, S. Milana, Y. Lu, Q. Q. Li, A. C. Ferrari, and P. H. Tan, "Raman spectroscopy of shear and layer breathing modes in multilayer MoS_2," *Physical Review B*, vol. 87, no. 11, Mar. 2013. DOI: 10.1103/physrevb.87.115413. [Online]. Available: http://dx.doi.org/10.1103/PhysRevB.87.115413.

[17] M. Amani, D.-H. Lien, D. Kiriya, J. Xiao, A. Azcatl, J. Noh, S. R. Madhvapathy, R. Addou, S. KC, M. Dubey, K. Cho, R. M. Wallace, S.-C. Lee, J.-H. He, J. W. Ager, X. Zhang, E. Yablonovitch, and A. Javey, "Near-unity photoluminescence quantum yield in MoS_2," *Science*, vol. 350, no. 6264, pp. 1065–1068, 2015, ISSN: 0036-8075. DOI: 10.1126/science.aad2114. eprint: http://science.sciencemag.org/content/350/6264/1065.full.pdf. [Online]. Available: http://science.sciencemag.org/content/350/6264/1065.

[18] D. Kozawa, R. Kumar, A. Carvalho, K. K. Amara, W. Zhao, S. Wang, M. Toh, R. M. Ribeiro, A. H. C. Neto, K. Matsuda, and G. Eda, "Photocarrier relaxation pathway in two-dimensional semiconducting transition metal dichalcogenides," *Nature Communications*, vol. 5, Jul. 2014. DOI: 10.1038/ncomms5543. [Online]. Available: http://dx.doi.org/10.1038/ncomms5543.

[19] Z. Nie, R. Long, J. S. Teguh, C.-C. Huang, D. W. Hewak, E. K. L. Yeow, Z. Shen, O. V. Prezhdo, and Z.-H. Loh, "Ultrafast electron and hole relaxation pathways in few-layer MoS_2," *J. Phys. Chem. C*, vol. 119, no. 35, pp. 20 698–20 708, Sep. 2015. DOI: 10.1021/acs.jpcc.5b05048. [Online]. Available: http://dx.doi.org/10.1021/acs.jpcc.5b05048.

[20] T. Olsen, S. Latini, F. Rasmussen, and K. S. Thygesen, "Simple screened hydrogen model of excitons in two-dimensional materials," *Phys. Rev. Lett.*, vol. 116, no. 5, Feb. 2016. DOI: 10.1103/physrevlett.116.056401. [Online]. Available: http://dx.doi.org/10.1103/PhysRevLett.116.056401.

[21] A. Chernikov, T. C. Berkelbach, H. M. Hill, A. Rigosi, Y. Li, O. B. Aslan, D. R. Reichman, M. S. Hybertsen, and T. F. Heinz, "Exciton binding energy and nonhydrogenic rydberg series in monolayer WS_2," *Phys. Rev. Lett.*, vol. 113, no. 7, Aug. 2014. DOI: 10.1103/physrevlett.113.076802. [Online]. Available: http://dx.doi.org/10.1103/PhysRevLett.113.076802.

[22] H. M. Hill, A. F. Rigosi, C. Roquelet, A. Chernikov, T. C. Berkelbach, D. R. Reichman, M. S. Hybertsen, L. E. Brus, and T. F. Heinz, "Observation of excitonic rydberg states in monolayer MoS_2 and WS_2 by photoluminescence excitation spectroscopy," *Nano Letters*, vol. 15, no. 5, pp. 2992–2997, May 2015. DOI: 10.1021/nl504868p. [Online]. Available: http://dx.doi.org/10.1021/nl504868p.

[23] N. Saigal, V. Sugunakar, and S. Ghosh, "Exciton binding energy in bulk MoS_2: A reassessment," *Appl. Phys. Lett.*, vol. 108, no. 13, p. 132 105, Mar. 2016. DOI: 10.1063/1.4945047. [Online]. Available: http://dx.doi.org/10.1063/1.4945047.

[24] C. Backes, R. J. Smith, N. McEvoy, N. C. Berner, D. McCloskey, H. C. Nerl, A. O'Neill, P. J. King, T. Higgins, D. Hanlon, N. Scheuschner, J. Maultzsch, L. Houben, G. S. Duesberg, J. F. Donegan, V. Nicolosi, and J. N. Coleman, "Edge and confinement effects allow in situ measurement of size and thickness of liquid-exfoliated nanosheets," *Nature Communications*, vol. 5, Aug. 2014. DOI: 10.1038/ncomms5576. [Online]. Available: http://dx.doi.org/10.1038/ncomms5576.

[25] B. Ganchev, N. Drummond, I. Aleiner, and V. Fal'ko, "Three-particle complexes in two-dimensional semiconductors," *Physical Review Letters*, vol. 114, no. 10, Mar. 2015. DOI: 10.1103/physrevlett.114.107401. [Online]. Available: http://dx.doi.org/10.1103/PhysRevLett.114.107401.

[26] E. J. Sie, A. J. Frenzel, Y.-H. Lee, J. Kong, and N. Gedik, "Intervalley biexcitons and many-body effects in monolayer MoS_2," *Phys. Rev. B*, vol. 92, no. 12, Sep. 2015. DOI: 10.1103/physrevb.92.125417. [Online]. Available: http://dx.doi.org/10.1103/PhysRevB.92.125417.

[27] Y. You, X.-X. Zhang, T. C. Berkelbach, M. S. Hybertsen, D. R. Reichman, and T. F. Heinz, "Observation of biexcitons in monolayer WSe_2," *Nat Phys*, vol. 11, no. 6, pp. 477–481, May 2015. DOI: 10.1038/nphys3324. [Online]. Available: http://dx.doi.org/10.1038/NPHYS3324.

[28] K. F. Mak, K. He, C. Lee, G. H. Lee, J. Hone, T. F. Heinz, and J. Shan, "Tightly bound trions in monolayer MoS_2," *Nature Materials*, vol. 12, no. 3, pp. 207–211, Dec. 2013. DOI: 10.1038/nmat3505. [Online]. Available: http://dx.doi.org/10.1038/NMAT3505.

[29] C. Grenier, C. Ciuti, and A. Imamoglu, "Trion-polaritons: How strong coupling to a cavity changes the orbital and spin properties of trions," 2016, [Online]. Available: https://arxiv.org/abs/1507.02480v1.

[30] H. Shi, R. Yan, S. Bertolazzi, J. Brivio, B. Gao, A. Kis, D. Jena, H. G. Xing, and L. Huang, "Exciton dynamics in suspended monolayer and few-layer MoS_2 2D crystals," *ACS Nano*, vol. 7, no. 2, pp. 1072–1080, Feb. 2013. DOI: 10.1021/nn303973r. [Online]. Available: http://dx.doi.org/10.1021/nn303973r.

[31] T. Korn, S. Heydrich, M. Hirmer, J. Schmutzler, and C. Schüller, "Low-temperature photocarrier dynamics in monolayer MoS_2," *Appl. Phys. Lett.*, vol. 99, no. 10, p. 102 109, 2011. DOI: 10.1063/1.3636402. [Online]. Available: http://dx.doi.org/10.1063/1.3636402.

[32] A. G. Čabo, J. A. Miwa, S. S. Grønborg, J. M. Riley, J. C. Johannsen, C. Cacho, O. Alexander, R. T. Chapman, E. Springate, M. Grioni, J. V. Lauritsen, P. D. C. King, P. Hofmann, and S. Ulstrup, "Observation of ultrafast free carrier dynamics in single layer MoS_2," *Nano Letters*, vol. 15, no. 9, pp. 5883–5887, Sep. 2015. DOI: 10.1021/acs.nanolett.5b01967. [Online]. Available: http://dx.doi.org/10.1021/acs.nanolett.5b01967.

[33] H. Wang, C. Zhang, and F. Rana, "Surface recombination limited lifetimes of photoexcited carriers in few-layer transition metal dichalcogenide MoS_2," *Nano Letters*, vol. 15, no. 12, pp. 8204–8210, Dec. 2015. DOI: 10.1021/acs.nanolett.5b03708. [Online]. Available: http://dx.doi.org/10.1021/acs.nanolett.5b03708.

[34] A. Tanaka, N. J. Watkins, and Y. Gao, "Hot-electron relaxation in the layered semiconductor 2h-MoS_2 studied by time-resolved two-photon photoemission spectroscopy," *Physical Review B*, vol. 67, no. 11, Mar. 2003. DOI: 10.1103/physrevb.67.113315. [Online]. Available: http://dx.doi.org/10.1103/PhysRevB.67.113315.

[35] Z. Nie, R. Long, L. Sun, C.-C. Huang, J. Zhang, Q. Xiong, D. W. Hewak, Z. Shen, O. V. Prezhdo, and Z.-H. Loh, "Ultrafast carrier thermalization and cooling dynamics in few-layer MoS_2," *ACS Nano*, vol. 8, no. 10, pp. 10 931–10 940, Oct. 2014. DOI: 10.1021/nn504760x. [Online]. Available: http://dx.doi.org/10.1021/nn504760x.

[36] E. A. A. Pogna, M. Marsili, D. D. Fazio, S. D. Conte, C. Manzoni, D. Sangalli, D. Yoon, A. Lombardo, A. C. Ferrari, A. Marini, G. Cerullo, and D. Prezzi, "Photo-induced bandgap renormalization governs the ultrafast response of single-layer MoS_2," *ACS Nano*, vol. 10, no. 1, pp. 1182–1188, Jan. 2016. DOI: 10.1021/acsnano.5b06488. [Online]. Available: http://dx.doi.org/10.1021/acsnano.5b06488.

[37] A. Chernikov, C. Ruppert, H. M. Hill, A. F. Rigosi, and T. F. Heinz, "Population inversion and giant bandgap renormalization in atomically thin WS_2 layers," *Nature Photonics*, vol. 9, no. 7, pp. 466–470, Jun. 2015. DOI: 10.1038/nphoton.2015.104. [Online]. Available: http://dx.doi.org/10.1038/NPHOTON.2015.104.

[38] A. Boulesbaa, B. Huang, K. Wang, M.-W. Lin, M. Mahjouri-Samani, C. Rouleau, K. Xiao, M. Yoon, B. Sumpter, A. Puretzky, and D. Geohegan, "Observation of two distinct negative trions in tungsten disulfide monolayers," *Phys. Rev. B*, vol. 92, no. 11, Sep. 2015. DOI: 10.1103/physrevb.92.115443. [Online]. Available: http://dx.doi.org/10.1103/PhysRevB.92.115443.

[39] M. Palummo, M. Bernardi, and J. C. Grossman, "Exciton radiative lifetimes in two-dimensional transition metal dichalcogenides," *Nano Letters*, vol. 15, no. 5, pp. 2794–2800, May 2015. DOI: 10.1021/nl503799t. [Online]. Available: http://dx.doi.org/10.1021/nl503799t.

[40] (2016). Locked phases, [Online]. Available: https://www.rp-photonics.com/mode_locking.html (visited on 12/15/2016).

[41] (2016). Modelocking, [Online]. Available: https://www.rp-photonics.com/mode_locking.html (visited on 12/15/2016).

[42] R. Alfano, Ed., *The supercontinuum laser source*. Springer, 2006.

[43] J. H. Marburger, "Self-focusing: Theory," *Prog. Quant. Electr.*, vol. 4, no. 1, pp. 35–110, 1975.

[44] M. Bradler, P. Baum, and E. Riedle, "Femtosecond continuum generation in bulk laser host materials with sub-μJ pump pulses," *Applied Physics B*, vol. 97, no. 3, pp. 561–574, Aug. 2009. DOI: 10.1007/s00340-009-3699-1. [Online]. Available: http://dx.doi.org/10.1007/s00340-009-3699-1.

[45] M. M. Benameur, B. Radisavljevic, J. S. Heron, S. Sahoo, H. Berger, and A. Kis, "Visibility of dichalcogenide nanolayers," *Nanotechnology*, 2011.

[46] S. Ghatak, A. N. Pal, and A. Ghosh, "Nature of electronic states in atomically thin MoS_2 field-effect transistors," *ACS Nano*, vol. 5, no. 10, pp. 7707–7712, Oct. 2011. DOI: 10.1021/nn202852j. [Online]. Available: https://doi.org/10.1021%2Fnn202852j.

[47] D. Vella, D. Ovchinnikov, N. Martino, V. Vega-Mayoral, D. Dumcenco, Y.-C. Kung, M.-R. Antognazza, A. Kis, G. Lanzani, D. Mihailovic, and C. Gadermaier, "Unconventional electroabsorption in monolayer MoS_2," *2D Materials*, no. 2, 2017. DOI: 10.1088/2053-1583/aa5784. [Online]. Available: https://doi.org/10.1088/2053-1583/aa5784.

[48] D. Ovchinnikov, F. Gargiulo, A. Allain, D. J. Pasquier, D. Dumcenco, C.-H. Ho, O. V. Yazyev, and A. Kis, "Disorder engineering and conductivity dome in ReS_2 with electrolyte gating," *Nature Communications*, vol. 7, p. 12 391, Aug. 2016. DOI: 10.1038/ncomms12391. [Online]. Available: https://doi.org/10.1038%2Fncomms12391.

[49] D. Sercombe, S. Schwarz, O. D. Pozo-Zamudio, F. Liu, B. J. Robinson, E. A. Chekhovich, I. I. Tartakovskii, O. Kolosov, and A. I. Tartakovskii, "Optical investigation of the natural electron doping in thin MoS_2 films deposited on dielectric substrates," *Scientific Reports*, vol. 3, Dec. 2013. DOI: 10.1038/srep03489. [Online]. Available: http://dx.doi.org/10.1038/srep03489.

[50] G. Plechinger, F.-X. Schrettenbrunner, J. Eroms, D. Weiss, C. Schüller, and T. Korn, "Low-temperature photoluminescence of oxide-covered single-layer MoS_2," *Physica status solidi (RRL) - Rapid Research Letters*, vol. 6, no. 3, pp. 126–128, Jan. 2012. DOI: 10.1002/pssr.201105589. [Online]. Available: http://dx.doi.org/10.1002/pssr.201105589.

[51] H. R. Gutierrez, N. Perea-Lopez, A. L. Elias, A. Berkdemir, B. Wang, R. Lv, F. Lopez-Urias, V. H. Crespi, H. Terrones, and M. Terrones, "Extraordinary room-temperature photoluminescence in triangular WS_2 monolayers," *Nano Letters*, vol. 13, no. 8, pp. 3447–3454, Aug. 2013. DOI: 10.1021/nl3026357. [Online]. Available: http://dx.doi.org/10.1021/nl3026357.

[52] L. Yadgarov, C. L. Choi, A. Sedova, A. Cohen, R. Rosentsveig, O. Bar-Elli, D. Oron, H. Dai, and R. Tenne, "Dependence of the absorption and optical surface plasmon scattering of MoS_2 nanoparticles on aspect ratio, size, and media," *ACS Nano*, vol. 8, no. 4, pp. 3575–3583, Apr. 2014. DOI: 10.1021/nn5000354. [Online]. Available: http://dx.doi.org/10.1021/nn5000354.

[53] S. Mouri, Y. Miyauchi, and K. Matsuda, "Tunable photoluminescence of monolayer MoS_2 via chemical doping," *Nano Letters*, vol. 13, no. 12, pp. 5944–5948, Dec. 2013. DOI: 10.1021/nl403036h. [Online]. Available: http://dx.doi.org/10.1021/nl403036h.

[54] V. I. Klimov, S. A. Ivanov, J. Nanda, M. Achermann, I. Bezel, J. A. McGuire, and A. Piryatinski, "Single-exciton optical gain in semiconductor nanocrystals," *Nature*, vol. 447, no. 7143, pp. 441–446, May 2007. DOI: 10.1038/nature05839. [Online]. Available: http://dx.doi.org/10.1038/nature05839.

[55] J. Cabanillas-Gonzalez, T. Virgili, A. Gambetta, G. Lanzani, T. D. Anthopoulos, and D. M. de Leeuw, "Photoinduced transient stark spectroscopy in organic semiconductors: A method for charge mobility determination in the picosecond regime," *Physical Review Letters*, vol. 96, no. 10, pp. 1–4, Mar. 2006. DOI: 10.1103/physrevlett.96.106601. [Online]. Available: http://dx.doi.org/10.1103/PhysRevLett.96.106601.

[56] C. Gadermaier, E. Menna, M. Meneghetti, W. J. Kennedy, Z. V. Vardeny, and G. Lanzani, "Long-lived charged states in single-walled carbon nanotubes," *Nano Letters*, vol. 6, no. 2, pp. 301–305, Feb. 2006. DOI: 10.1021/nl051970t. [Online]. Available: http://dx.doi.org/10.1021/nl051970t.

[57] G. Soavi, F. Scotognella, D. Brida, T. Hefner, F. Späth, M. R. Antognazza, T. Hertel, G. Lanzani, and G. Cerullo, "Ultrafast charge photogeneration in semiconducting carbon nanotubes," *The Journal of Physical Chemistry C*, vol. 117, no. 20, pp. 10 849–10 855, May 2013. DOI: 10.1021/jp404009z. [Online]. Available: http://dx.doi.org/10.1021/jp404009z.

[58] S. Sim, J. Park, J.-G. Song, C. In, Y.-S. Lee, H. Kim, and H. Choi, "Exciton dynamics in atomically thin MoS_2 : Interexcitonic interaction and broadening kinetics," *Physical Review B*, vol. 88, no. 7, Aug. 2013. DOI: 10.1103/physrevb.88.075434. [Online]. Available: http://dx.doi.org/10.1103/PhysRevB.88.075434.

[59] G. Trankle, E. Lach, A. Forchel, F. Scholz, C. Ell, H. Haug, G. Weimann, G. Griffiths, H. Kroemer, and S. Subbanna, "General relation between band-gap renormalization and carrier density in two-dimensional and electron-hole plasmas," *PHYSICAL REVIEW B*, vol. 36, no. 12, pp. 6712–6714, 1987.

[60] Q. Wang, S. Ge, X. Li, J. Qiu, Y. Ji, J. Feng, and D. Sun, "Valley carrier dynamics in monolayer molybdenum disulfide from helicity-resolved ultrafast pump-probe spectroscopy," *ACS Nano*, vol. 7, no. 12, pp. 11 087–11 093, Dec. 2013. DOI: 10.1021/nn405419h. [Online]. Available: http://dx.doi.org/10.1021/nn405419h.

[61] M. M. Ugeda, A. J. Bradley, S.-F. Shi, F. H. da Jornada, Y. Zhang, D. Y. Qiu, W. Ruan, S.-K. Mo, Z. Hussain, Z.-X. Shen, F. Wang, S. G. Louie, and M. F. Crommie, "Giant bandgap renormalization and excitonic effects in a monolayer transition metal dichalcogenide semiconductor," *Nature Materials*, vol. 13, no. 12, pp. 1091–1095, Aug. 2014. DOI: 10.1038/nmat4061. [Online]. Available: http://dx.doi.org/10.1038/NMAT4061.

[62] S. Schmitt-Rink, D. Chemla, and D. Miller, "Linear and nonlinear optical properties of semiconductor quantum wells," *Advances in Physics*, no. 2, pp. 89–188, 1989.

[63] M. Yan, L. J. Rothberg, E. Kwock, and T. M. Miller, "Interchain excitations in conjugated polymers," *PHYSICAL REVIEW LETTERS*, no. 10, 1995.

[64] C. Manzoni, A. Gambetta, E. Menna, M. Meneghetti, G. Lanzani, and G. Cerullo, "Intersubband exciton relaxation dynamics in single-walled carbon nanotubes," *Physical Review Letters*, vol. 94, no. 20, May 2005. DOI: 10.1103/physrevlett.94.207401. [Online]. Available: http://dx.doi.org/10.1103/PhysRevLett.94.207401.

[65] A. Ramasubramaniam, "Large excitonic effects in monolayers of molybdenum and tungsten dichalcogenides," *Physical Review B*, vol. 86, no. 11, Sep. 2012. DOI: 10.1103/physrevb.86.115409. [Online]. Available: http://dx.doi.org/10.1103/PhysRevB.86.115409.

[66] C. Gadermaier, G. Cerullo, G. Sansone, G. Leising, U. Scherf, and G. Lanzani, "Time-resolved charge carrier generation from higher lying excited states in conjugated polymers," *Physical Review Letters*, vol. 89, no. 11, Aug. 2002. DOI: 10.1103/physrevlett.89.117402. [Online]. Available: http://dx.doi.org/10.1103/PhysRevLett.89.117402.

[67] J. Noolandi and K. M. Hong, "Theory of photogeneration and fluorescence quenching," *The Journal of Chemical Physics*, no. 7, 1979.

[68] V. I. Arkhipov, E. Emelianova, and H. Bässler, "Hot exciton dissociation in a conjugated polymer," *PHYSICAL REVIEW LETTERS*, no. 6, 1999.

[69] A. Leitenstorfer, C. Fürst, A. Laubereau, and W. Kaiser, "Femtosecond carrier dynamics in gaas far from equilibrium," *PHYSICAL REVIEW LETTERS*, no. 9, 1996.

[70] D. Sun, Z.-K. Wu, C. Divin, X. Li, C. Berger, W. A. de Heer, P. N. First, and T. B. Norris, "Ultrafast relaxation of excited dirac fermions in epitaxial graphene using optical differential transmission spectroscopy," *Physical Review Letters*, vol. 101, no. 15, Oct. 2008. DOI: 10.1103/physrevlett.101.157402. [Online]. Available: http://dx.doi.org/10.1103/PhysRevLett.101.157402.

[71] C. Gadermaier, V. V. Kabanov, A. S. Alexandrov, L. Stojchevska, T. Mertelj, C. Manzoni, G. Cerullo, N. D. Zhigadlo, J. Karpinski, Y. Q. Cai, X. Yao, Y. Toda, M. Oda, S. Sugai, and D. Mihailovic, "Strain-induced enhancement of the electron energy relaxation in strongly correlated superconductors," *Physical Review X*, vol. 4, no. 1, Mar. 2014. DOI: 10.1103/physrevx.4.011056. [Online]. Available: http://dx.doi.org/10.1103/PhysRevX.4.011056.

[72] L. Dhar, J. A. Rogers, and K. A. Nelson, "Time-resolved vibrational spectroscopy in the impulsive limit," *Chem. Rev.*, no. 1, pp. 157–193, 1994.

[73] T. Ichibayashi, S. Tanaka, J. Kanasaki, K. Tanimura, and T. Fauster, "Ultrafast relaxation of highly excited hot electrons in si: Roles of the l - x intervalley scattering," *Physical Review B*, vol. 84, no. 23, Dec. 2011. DOI: 10.1103/physrevb.84.235210. [Online]. Available: http://dx.doi.org/10.1103/PhysRevB.84.235210.

[74] G. Wang, X. Marie, L. Bouet, M. Vidal, A. Balocchi, T. Amand, D. Lagarde, and B. Urbaszek, "Exciton dynamics in WSe_2 bilayers," *Applied Physics Letters*, no. 18, 2014.

[75] C. Mai, A. Barrette, Y. Yu, Y. G. Semenov, K. W. Kim, L. Cao, and K. Gundogdu, "Many-body effects in valleytronics: Direct measurement of valley lifetimes in single-layer MoS_2," *Nano Letters*, vol. 14, no. 1, pp. 202–206, Jan. 2014. DOI: 10.1021/nl403742j. [Online]. Available: http://dx.doi.org/10.1021/nl403742j.

[76] D. Lagarde, L. Bouet, X. Marie, C. R. Zhu, B. L. Liu, T. Amand, P. H. Tan, and B. Urbaszek, "Carrier and polarization dynamics in monolayer MoS_2," *Physical Review Letters*, vol. 112, no. 4, Jan. 2014. DOI: 10.1103/physrevlett.112.047401. [Online]. Available: http://dx.doi.org/10.1103/PhysRevLett.112.047401.

[77] M. J. Assael, S. Botsios, K. GialouI, and I. N. Metaxa, "Thermal conductivity of polymethyl methacrylate (pmma) and borosilicate crown glass bk7," *International Journal of Thermophysics*, no. 5, pp. 1595–1605, 2005.

[78] Q. .-.-C. Sun, L. Yadgarov, R. Rosentsveig, G. Seifert, R. Tenne, and J. L. Musfeldt, "Observation of a burstein-moss shift in rhenium-doped MoS_2 nanoparticles," *ACS Nano*, vol. 7, no. 4, pp. 3506–3511, Apr. 2013. DOI: 10.1021/nn400464g. [Online]. Available: http://dx.doi.org/10.1021/nn400464g.

[79] M. Fontana, T. Deppe, A. K. Boyd, M. Rinzan, A. Y. Liu, M. Paranjape, and P. Barbara, "Electron-hole transport and photovoltaic effect in gated MoS_2 schottky junctions," *Scientific Reports*, vol. 3, Apr. 2013. DOI: 10.1038/srep01634. [Online]. Available: http://dx.doi.org/10.1038/srep01634.

[80] O. Lopez-Sanchez, D. Lembke, M. Kayci, A. Radenovic, and A. Kis, "Ultrasensitive photodetectors based on monolayer MoS_2," *Nature Nanotechnology*, vol. 8, no. 7, pp. 497–501, Jun. 2013. DOI: 10.1038/nnano.2013.100. [Online]. Available: http://dx.doi.org/10.1038/NNANO.2013.100.

[81] A. Pospischil, M. M. Furchi, and T. Mueller, "Solar-energy conversion and light emission in an atomic monolayer p–n diode," *Nature Nanotechnology*, vol. 9, no. 4, pp. 257–261, Mar. 2014. DOI: 10.1038/nnano.2014.14. [Online]. Available: https://doi.org/10.1038%2Fnnano.2014.14.

[82] B. W. H. Baugher, H. O. H. Churchill, Y. Yang, and P. Jarillo-Herrero, "Optoelectronic devices based on electrically tunable p–n diodes in a monolayer dichalcogenide," *Nature Nanotechnology*, vol. 9, no. 4, pp. 262–267, Mar. 2014. DOI: 10.1038/nnano.2014.25. [Online]. Available: https://doi.org/10.1038%2Fnnano.2014.25.

[83] L. Britnell, R. M. Ribeiro, A. Eckmann, R. Jalil, B. D. Belle, A. Mishchenko, Y.-J. Kim, R. V. Gorbachev, T. Georgiou, S. V. Morozov, A. N. Grigorenko, A. K. Geim, C. Casiraghi, A. H. C. Neto, and K. S. Novoselov, "Strong light-matter interactions in heterostructures of atomically thin films," *Science*, pp. 1311–1314, 2013. DOI: 10.1126/science.1235547.

[84] C.-H. Lee, G.-H. Lee, A. M. van der Zande, W. Chen, Y. Li, M. Han, X. Cui, G. Arefe, C. Nuckolls, T. F. Heinz, J. Guo, J. Hone, and P. Kim, "Atomically thin p–n junctions with van der waals heterointerfaces," *Nature Nanotechnology*, vol. 9, no. 9, pp. 676–681, Aug. 2014. DOI: 10.1038/nnano.2014.150. [Online]. Available: https://doi.org/10.1038%2Fnnano.2014.150.

[85] X. Hong, J. Kim, S.-F. Shi, Y. Zhang, C. Jin, Y. Sun, S. Tongay, J. Wu, Y. Zhang, and F. Wang, "Ultrafast charge transfer in atomically thin MoS_2/WS_2 heterostructures," *Nature Nanotechnology*, vol. 9, no. 9, pp. 682–686, Aug. 2014. DOI: 10.1038/nnano.2014.167. [Online]. Available: https://doi.org/10.1038%2Fnnano.2014.167.

[86] Q. H. Wang, K. Kalantar-Zadeh, A. Kis, J. N. Coleman, and M. S. Strano, "Electronics and optoelectronics of two-dimensional transition metal dichalcogenides," *Nature Nanotechnology*, vol. 7, no. 11, pp. 699–712, Nov. 2012. DOI: 10.1038/nnano.2012.193. [Online]. Available: http://dx.doi.org/10.1038/NNANO.2012.193.

[87] S. Z. Butler, S. M. Hollen, L. Cao, Y. Cui, J. A. Gupta, H. R. Gutiérrez, T. F. Heinz, S. S. Hong, J. Huang, A. F. Ismach, E. Johnston-Halperin, M. Kuno, V. V. Plashnitsa, R. D. Robinson, R. S. Ruoff, S. Salahuddin, J. Shan, L. Shi, M. G. Spencer, M. Terrones, W. Windl, and J. E. Goldberger, "Progress, challenges, and opportunities in two-dimensional materials beyond graphene," *ACS Nano*, vol. 7, no. 4, pp. 2898–2926, Apr. 2013. DOI: 10.1021/nn400280c. [Online]. Available: http://dx.doi.org/10.1021/nn400280c.

[88] B. Radisavljevic, A. Radenovic, J. Brivio, V. Giacometti, and A. Kis, "Single-layer MoS_2 transistors," *Nature Nanotechnology*, vol. 6, no. 3, pp. 147–150, Jan. 2011. DOI: 10.1038/nnano.2010.279. [Online]. Available: http://dx.doi.org/10.1038/NNANO.2010.279.

[89] V. Nicolosi, M. Chhowalla, M. G. Kanatzidis, M. S. Strano, and J. N. Coleman, "Liquid exfoliation of layered materials," *Science*, vol. 340, no. 6139, pp. 1 226 419–1 226 419, Jun. 2013. DOI: 10.1126/science.1226419. [Online]. Available: http://dx.doi.org/10.1126/science.1226419.

[90] J. N. Coleman, M. Lotya, A. O'Neill, S. D. Bergin, P. J. King, U. Khan, K. Young, A. Gaucher, S. De, R. J. Smith, I. V. Shvets, S. K. Arora, G. Stanton, H.-Y. Kim, K. Lee, G. T. Kim, G. S. Duesberg, T. Hallam, J. J. Boland, J. J. Wang, J. F. Donegan, J. C. Grunlan, G. Moriarty, A. Shmeliov, R. J. Nicholls, J. M. Perkins, E. M. Grieveson, K. Theuwissen, D. W. McComb, P. D. Nellist, and V. Nicolosi, "Two-dimensional nanosheets produced by liquid exfoliation of layered materials," *Science*, vol. 331, no. 6017, pp. 568–571, Feb. 2011. DOI: 10.1126/science.1194975. [Online]. Available: http://dx.doi.org/10.1126/science.1194975.

[91] F. Bonaccorso, A. Bartolotta, J. N. Coleman, and C. Backes, "2d-crystal-based functional inks," *Advanced Materials*, vol. 28, no. 29, pp. 6136–6166, Jun. 2016. DOI: 10.1002/adma.201506410. [Online]. Available: https://doi.org/10.1002%2Fadma.201506410.

[92] K. F. Mak and J. Shan, "Photonics and optoelectronics of 2d semiconductor transition metal dichalcogenides," *Nature Photonics*, vol. 10, no. 4, pp. 216–226, Mar. 2016. DOI: 10.1038/nphoton.2015.282. [Online]. Available: https://doi.org/10.1038%2Fnphoton.2015.282.

[93] Z. Sun, A. Martinez, and F. Wang, "Optical modulators with 2d layered materials," *Nature Photonics*, vol. 10, no. 4, pp. 227–238, Mar. 2016. DOI: 10.1038/nphoton.2016.15. [Online]. Available: https://doi.org/10.1038%2Fnphoton.2016.15.

[94] T. Borzda, C. Gadermaier, N. Vujicic, P. Topolovsek, M. Borovsak, T. Mertelj, D. Viola, C. Manzoni, E. A. A. Pogna, D. Brida, M. R. Antognazza, F. Scotognella, G. Lanzani, G. Cerullo, and D. Mihailovic, "Charge photogeneration in few-layer MoS_2," *Advanced Functional Materials*, vol. 25, no. 22, pp. 3351–3358, Apr. 2015. DOI: 10.1002/adfm.201500709. [Online]. Available: https://doi.org/10.1002%2Fadfm.201500709.

[95] V. Vega-Mayoral, D. Vella, T. Borzda, M. Prijatelj, I. Tempra, E. A. A. Pogna, S. D. Conte, P. Topolovsek, N. Vujicic, G. Cerullo, D. Mihailovic, and C. Gadermaier, "Exciton and charge carrier dynamics in few-layer WS_2," *Nanoscale*, no. 8, pp. 5428–5434, 2016. DOI: 10.1039/C5NR08384B.

[96] P. D. Cunningham, K. M. McCreary, A. T. Hanbicki, M. Currie, B. T. Jonker, and L. M. Hayden, "Charge trapping and exciton dynamics in large-area CVD grown MoS_2," *The Journal of Physical Chemistry C*, vol. 120, no. 10, pp. 5819–5826, Mar. 2016. DOI: 10.1021/acs.jpcc.6b00647. [Online]. Available: https://doi.org/10.1021%2Facs.jpcc.6b00647.

[97] D. Tsokkou, X. Yu, K. Sivula, and N. Banerji, "The role of excitons and free charges in the excited-state dynamics of solution-processed few-layer MoS_2 nanoflakes," *The Journal of Physical Chemistry C*, vol. 120, no. 40, pp. 23 286–23 292, Oct. 2016. DOI: 10.1021/acs.jpcc.6b09267. [Online]. Available: https://doi.org/10.1021%2Facs.jpcc.6b09267.

[98] L. Wang, Z. Wang, H.-Y. Wang, G. Grinblat, Y.-L. Huang, D. Wang, X.-H. Ye, X.-B. Li, Q. Bao, A.-S. Wee, S. A. Maier, Q.-D. Chen, M.-L. Zhong, C.-W. Qiu, and H.-B. Sun, "Slow cooling and efficient extraction of c-exciton hot carriers in MoS_2 monolayer," *Nature Communications*, vol. 8, p. 13 906, Jan. 2017. DOI: 10.1038/ncomms13906. [Online]. Available: https://doi.org/10.1038%2Fncomms13906.

[99] A. Carvalho, R. M. Ribeiro, and A. H. C. Neto, "Band nesting and the optical response of two-dimensional semiconducting transition metal dichalcogenides," *Physical Review B*, vol. 88, no. 11, Sep. 2013. DOI: 10.1103/physrevb.88.115205. [Online]. Available: https://doi.org/10.1103%2Fphysrevb.88.115205.

[100] G. Plechinger, P. Nagler, J. Kraus, N. Paradiso, C. Strunk, C. Schüller, and T. Korn, "Identification of excitons, trions and biexcitons in single-layer WS_2," *Physica status solidi (RRL) - Rapid Research Letters*, vol. 9, no. 8, pp. 457–461, Jul. 2015. DOI: 10.1002/pssr.201510224. [Online]. Available: https://doi.org/10.1002%2Fpssr.201510224.

[101] E. Pogna, G. Cerullo, and C. Gadermaier, "In preparation."

[102] A. Splendiani, L. Sun, Y. Zhang, T. Li, J. Kim, C.-Y. Chim, G. Galli, and F. Wang, "Emerging photoluminescence in monolayer MoS_2," *Nano Letters*, vol. 10, no. 4, pp. 1271–1275, Apr. 2010. DOI: 10.1021/nl903868w. [Online]. Available: http://dx.doi.org/10.1021/nl903868w.

[103] B. Chakraborty, A. Bera, D. V. S. Muthu, S. Bhowmick, U. V. Waghmare, and A. K. Sood, "Symmetry-dependent phonon renormalization in monolayer MoS_2 transistor," *Physical Review B*, vol. 85, no. 16, Apr. 2012. DOI: 10.1103/physrevb.85.161403.

[104] H. Terrones, E. D. Corro, S. Feng, J. M. Poumirol, D. Rhodes, D. Smirnov, N. R. Pradhan, Z. Lin, M. A. T. Nguyen, A. L. Elias, T. E. Mallouk, L. Balicas, M. A. Pimenta, and M. Terrones, "New first order raman-active modes in few layered transition metal dichalcogenides," *Scientific Reports*, vol. 4, pp. 1–9, Feb. 2014. DOI: 10.1038/srep04215. [Online]. Available: https://doi.org/10.1038%2Fsrep04215.

[105] Y. Ma, B. Liu, A. Zhang, L. Chen, M. Fathi, C. Shen, A. N. Abbas, M. Ge, M. Mecklenburg, and C. Zhou, "Reversible semiconducting-to-metallic phase transition in chemical vapor deposition grown monolayer WSe_2 and applications for devices," *ACS Nano*, vol. 9, no. 7, pp. 7383–7391, Jul. 2015. DOI: 10.1021/acsnano.5b02399. [Online]. Available: https://doi.org/10.1021%2Facsnano.5b02399.

[106] Y. Zhang, J. Ye, Y. Matsuhashi, and Y. Iwasa, "Ambipolar MoS_2 thin flake transistors," *Nano Letters*, vol. 12, no. 3, pp. 1136–1140, Mar. 2012. DOI: 10.1021/nl2021575. [Online]. Available: https://doi.org/10.1021%2Fnl2021575.

[107] J. Pu, Y. Yomogida, K.-K. Liu, L.-J. Li, Y. Iwasa, and T. Takenobu, "Highly flexible MoS_2 thin-film transistors with ion gel dielectrics," *Nano Letters*, vol. 12, no. 8, pp. 4013–4017, Aug. 2012. DOI: 10.1021/nl301335q. [Online]. Available: https://doi.org/10.1021%2Fnl301335q.

[108] D. Braga, I. G. Lezama, H. Berger, and A. F. Morpurgo, "Quantitative determination of the band gap of WS_2 with ambipolar ionic liquid-gated transistors," *Nano Letters*, vol. 12, no. 10, pp. 5218–5223, Oct. 2012. DOI: 10.1021/nl302389d. [Online]. Available: https://doi.org/10.1021%2Fnl302389d.

[109] M. M. Perera, M.-W. Lin, H.-J. Chuang, B. P. Chamlagain, C. Wang, X. Tan, M. M.-C. Cheng, D. Tomanek, and Z. Zhou, "Improved carrier mobility in few-layer MoS_2 field-effect transistors with ionic-liquid gating," *ACS Nano*, vol. 7, no. 5, pp. 4449–4458, May 2013. DOI: 10.1021/nn401053g. [Online]. Available: https://doi.org/10.1021%2Fnn401053g.

[110] L. Chu, H. Schmidt, J. Pu, S. Wang, B. Özyilmaz, T. Takenobu, and G. Eda, "Charge transport in ion-gated mono-, bi-, and trilayer MoS_2 field effect transistors," *Scientific Reports*, vol. 4, p. 7293, Dec. 2014. DOI: 10.1038/srep07293. [Online]. Available: https://doi.org/10.1038%2Fsrep07293.

[111] Y. Li, A. Chernikov, X. Zhang, A. Rigosi, H. M. Hill, A. M. van der Zande, D. A. Chenet, E.-M. Shih, J. Hone, and T. F. Heinz, "Measurement of the optical dielectric function of monolayer transition-metal dichalcogenides:MoS_2, $MoSe_2$, WS_2, and WSe_2," *Physical Review B*, vol. 90, no. 20, Nov. 2014. DOI: 10.1103/physrevb.90.205422. [Online]. Available: https://doi.org/10.1103%2Fphysrevb.90.205422.

Bibliography

Publications Related to the Thesis

T.Borzda, Ch. Gadermaier, N. Vujičić, P. Topolovšek, M. Borovšak, T. Mertelj, D. Viola, C. Manzoni, E. A. A. Pogna, D. Brida, M. R. Antognazza, F. Scotognella, G. Lanzani, G. Cerullo, D. Mihailović "Charge photogeneration in few-layer MoS_2", Adv. funct. mater. (Print), **25**, 3351-3358 (2015).

Journal Articles

1. V. Vega Mayoral, D. Vella, *T.Borzda*, M. Prijatelj, I. Tempra, E. A. A. Pogna, S. Dal Conte, P. Topolovšek, N. Vujičić, G. Cerullo, D. Mihailović, Ch. Gadermaier "Exciton and charge carrier dynamics in few-layer WS_2", Nanoscale, **8**, 10, 5428-5434 (2016).

2. D. Vella, V. Vega Mayoral, Ch. Gadermaier, N. Vujičić, *T. Borzda*, P. Topolovšek, M. Prijatelj, I. Tempra, E. A. A. Pogna, G. Cerullo "Femtosecond spectroscopy on MoS_2 flakes from liquid exfoliation : surfactant independent exciton dynamics", Journal of nanophotonics, **10**, 1, 1-8 (2015).

3. T. Mertelj, N. Vujičić, *T.Borzda*, I. Vaskivskyi, A. Pogrebna, D. Mihailović "Multichannel photodiode detector for ultrafast optical spectroscopy", Rev. sci. instrum., **85**, 12, 1-4 (2014).

4. A. Pogrebna, N. Vujičić, T. Mertelj, *T.Borzda*, G. Cao, Z. A. Xu, J.-H. Chu, I. R. Fisher, D. Mihailović "Spectrally resolved femtosecond reflectivity relaxation dynamics in undoped spin-density wave 122-structure iron-based pnictides", Phys. Rev. B, **89**, 16, 1-9 (2014).

Conference Contribution

1. *T.Borzda*, Ch. Gadermaier, P. Topolovšek, M. Borovšak, T. Mertelj, D. Mihailović "Charge photogeneration in few-layer MoS_2", V: Nonequilibrium phenomena in complex matter : new observations and new theories : book of abstract : Ambrož, Krvavec, Slovenia, December 13-16, 2015.

2. *T.Borzda*, N. Vujičić, Ch. Gadermaier, P. Topolovšek, T. Mertelj, D. Vella, V. Vega Mayoral, D. Mihailović "Femtosecond charge transfer from MoS_2 to organic acceptor", V: Proceedings, Four International Workshop o Nanocarbon Photonics and Optoelectronics, 28 July - 1 August 2014, Polviärvi, Finland, Joensuu.

3. *T.Borzda*, N. Vujičić, Ch. Gadermaier, P. Topolovšek, T. Mertelj, D. Vella, V. Vega Mayoral, D. Mihailović "Femtosecond charge transfer from MoS_2 to organic acceptor", V: Flatlands : beyond graphene : 9-11 June 2014, Dublin, Ireland, , Dublin, CRANN Institute, Trinity College Dublin, 2014.

4. *T.Borzda*, Ch. Gadermaier, N. Vujičić, P. Topolovšek, T. Mertelj, D. Viola, G. Cerullo, D. Mihailović "Ultrafast measurement of charge carriers dynamics in few-layers of MoS_2", V: Molecular nanostructures : program, XXVIIIth International Winterschool Euroconference on Electronic Properties of Novel Materials, IWEPNM 2014, 08-15 March, 2014, Kirchberg in Tirol, Austria.

Biography

The author of this thesis was born in 1989 in Chernigiv, Ukraine. She studied Physics in the Faculty of Physics at Kyiv National Taras Shevchenko University and graduated in 2012 with master thesis titled "Computational and spectroscopic investigation of hydrogen bond dynamics in methanol and hexanol trapped in argon matrix". In 2013 she entered the Ph.D. program in Nanoscience and Nanotechnologies at the Jožef Stefan International Postgraduate School.